MULTISCALE CHARACTERIZATION OF PROCESS-STRUCTURE-PROPERTY RELATIONSHIPS IN ADDITIVELY MANUFACTURED IN718

by

Dillon Scott Watring

A dissertation submitted to the faculty of
The University of Utah
in partial fulfillment of the requirements for the degree of

Doctor of Philosophy

Department of Mechanical Engineering

The University of Utah

August 2021

The University of Utah Graduate School

STATEMENT OF DISSERTATION APPROVAL

The dissertation of **Dillon Scott Watring**
has been approved by the following supervisory committee members:

Ashley Spear ,	Chair(s)	**4/16/2021** Date Approved
Michael Czabaj ,	Member	**4/16/2021** Date Approved
Owen Kingstedt ,	Member	**4/16/2021** Date Approved
Bart Raeymaekers ,	Member	**4/16/2021** Date Approved
Ravi Chandran ,	Member	**4/16/2021** Date Approved

by **Bruce K. Gale** , Chair/Dean of
the Department/College/School of **Mechanical Engineering**
and by **David B. Kieda** , Dean of The Graduate School.

ABSTRACT

Additive manufacturing has become a popular tool in a variety of different industries. However, there remain many unknowns regarding the processing-structure-property relationships and the corresponding quality, reliability, and performance of the parts. Laser powder bed fusion, which is one of the most common metal additive manufacturing techniques, has many benefits over traditional manufacturing and other metal additive manufacturing techniques. Inconel, which is a nickel-based superalloy, is a commonly used alloy for nuclear, aerospace, and marine industries due to its excellent mechanical properties at high temperatures. Although there is a significant amount of previous literature investigating processing-structure-property relationships of laser powder bed fused Inconel 718, few studies exist in the open literature that have investigated the variability of the pore structure, microstructure, tensile properties, and fatigue life in the as-built condition (i.e., no heat treatments or stress relieving). However, there are potential applications, such as deployment of additive manufacturing machines in the field, where it may not be possible to perform heat treatments. There is a need to better understand the relationships among laser-energy density, build orientation, pore structures, microstructures, and mechanical properties for the as-built condition.

In this dissertation, a multiscale experimental approach is implemented, wherein each chapter leverages progressively smaller specimens (all derived from the same initial build) intended to investigate different aspects of property-process-structure relationships in as-built laser powder bed fused Inconel 718. The research addresses three main objectives: **(1)** to investigate the mechanisms driving high-cycle fatigue life with respect to different processing conditions; **(2)** to investigate the effects of laser-energy density and build orientation on the pore structure, microstructure, and tensile properties; and **(3)** to modify and validate a void descriptor function to uniquely characterize pore networks and predict fracture location in mesoscale tensile specimens. The primary findings from each study are described in subsequent chapters.

CONTENTS

LIST OF TABLES

NOTATION AND SYMBOLS

V_{frac}	Percent of pore volume to nominal volume
N_{tot}	Number of pores in the gauge region
CSA_{ave}	Average percentage of cross-sectional area reduction
CSA_{max}	Maximum percentage of cross-sectional area reduction
$z_{CSA,max}$	The location in the gauge length of the max cross-section area reduction
ESD_{ave}	The average equivalent spherical diameter
EDS_{max}	The maximum equivalent spherical diameter
$z_{ESD,max}$	The location of the maximum pore by diameter
VDF_{max}	The global maximum value of the VDF
$z_{VDF,max}$	The location of the global VDF maximum
E	Elastic modulus
σ_Y	Yield strength
σ_U	Ultimate strength
e_f	Percent elongation
z_{ref}	Reference point along the axial direction of the specimen
v_i	Pore volume
D_i	Pore diameter
S_i	Distance from the reference position to the centroid of the i^{th} pore
r_i	Distance from the edge of the pore to the centroid of the cross section
x_i, y_i, z_i	Pore centroid
α, ρ, γ	Weighting parameters
V_{gauge}	Total volume of the gauge region
L	Length of the gauge section
c	Maximum distance from the centroid of the specimen to the free surface
a_i	Weighted nearest-neighbor distance term
w	The linear weights array
d	The array of nearest-neighbor distances
r_Y	Major semi-axis
r_b, r_c	Minor semi-axes
θ_{xy}	The angle between the major semi-axis and the XY plane
ϕ_x	The angle between the projected axis and the x-axis
ϕ_y	The angle between the projected axis and the y-axis
Ψ_i	The pore sphericity

ACKNOWLEDGEMENTS

I would like to take this opportunity to acknowledge and thank the important people in my life that have helped me make it to where I am today. First, I would like to thank my family. Specifically, my mother, Donna Wega, who has always supported me in every way she could and sacrificing a lot for the possibility for me to have a better life. I also want to thank my grandparents, Mimi and Papa, who helped raise me to become the person I am today. I also want to thank all of my aunts and uncles, who have provided me with priceless guidance and support throughout my life.

There were also many mentors and advisors throughout my life that have helped me succeed. My PhD advisor, Dr. Ashley Spear, has been crucial in my development as a researcher and has provided me with the knowledge and experience necessary to succeed. Throughout my PhD program, she has taught me the importance of hypothesis driven research and has taught me skills that often get overlooked in PhD programs (e.g., how to write grants, how to perform peer reviews, etc.). Her outstanding reputation in the field of materials science has also opened the door for me to make meaningful and lasting collaborations. I will forever be grateful for her mentorship in my life. I would like to also acknowledge my master's advisors Dr. Benjamin Boesl and Dr. Dwayne McDaniel both who provided me with countless amounts of support and guidance. They both, similar to Dr. Spear, provided me with an in depth understanding and passion for research in academia. I hope everyone gets the opportunity to have amazing mentors like Dr. Spear, Dr. Boesl, and Dr. McDaniel. I would also specifically like to thank all the other members of my advisory committee, Dr. Owen Kingstedt, Dr. Bart Raeymaekers, Dr. Michael Czabaj, and Dr. K.S. Ravi Chandran.

My work has also been made possible due to all of my collaborators and co-authors. Specifically, I would like to thank Jake Benzing and Nik Hrabe from the National Institute of Standards and Technology for all of the work they have done on my research projects and for providing me with technical guidance and their expertise. Their collaborations

have helped me grow as a researcher and provided me with unique research opportunities that I will continue throughout my career. I also would like to thank the rest of my co-authors and collaborators Orion Kafka, Newell Moser, Kristen Carter, Dustin Crouse, and Nadia Kouraytem.

PhD programs are not known for being easy and I wanted to thank all of my friends and fellow lab members that have made my time at Utah memorable. Thanks to Brian Phung, Cole Schreiber, Karl Niendorf, Sarah Hood, and Marshall Ishmael for being some of my first friends in Utah. Thanks to my fellow lab members Karen Demille, Carl Herriott, John Erickson, Jimmy He, Nadia Kouraytem, Dongfang Zhao, and Quinn Johnson.

Finally, this research is supported by the Department of Defense Office of Economic Adjustment (ST1605-19-03) and by the National Science Foundation under Grant No. CMMI-1752400. I would like to express gratitude to 3D Systems for supplying the materials and the National Institute of Standards and Technology for providing access to testing equipment (EBSD, SEM, CT, and tension testing). The views expressed in the article do not necessarily represent the views of the U.S. DOC, NSF, or the United States Government.

CHAPTER 1

INTRODUCTION

Additive manufacturing (AM), commonly referred to as 3D printing, has become a popular and vital tool in a variety of different industries, especially in the aerospace, nuclear, marine, defense, and energy industries [2]. The annual Wohlers report forecasts the sales of AM products and services to exceed US$23.9 billion by the end of 2022 [3]. Metal AM techniques are currently revolutionizing, and will continue to revolutionize, the manufacturing of metals in large part due to the ability to reduce the manufacturing time, reduce the overall weight, enable geometric flexibility, and support the use of a wide variety of metals and their alloys [4]. Although AM techniques are becoming widely adopted for use in non-critical applications, there are many unknowns concerning the processing-structure-property relationships for AM metals, thereby hampering their widespread adoption in critical applications. Complicating the processing-structure-property relationships for AM metals even further, there are many different AM techniques used to manufacture metal parts, making it difficult to establish universal relationships. In general, industry and academia have typically classified these techniques into two main categories: powder bed fusion (PBF) and direct energy deposition (DED) [5]. One of the most commonly used PBF methods, and AM methods in general, is laser powder bed fusion (L-PBF), which will be the main focus of this dissertation [6]. In L-PBF (seen in Figure 1.1), a metal powder is spread or rolled (depending on the manufacturer) onto a build plate. A scanning laser is then used to locally melt/fuse a thin layer of metal powder to create the first layer. The build plate is then lowered and another layer of powder is spread on top of the lowered build plate. The scanning laser then melts the next layer of metal powder. This is repeated layer-by-layer until the full three-dimensional part is completed. L-PBF methods have many benefits over traditional manufacturing. Additionally, L-PBF methods allow for near net-shape production of complex geometries

that allow for the reduction in manufacturing time, reduction in post-processing time, reduction in weight, and geometric flexibility, which are some of the most touted benefits of AM [4].

To expand adoption of metal AM, especially in critical applications, a better understanding of the processing-structure-property relationships is needed. Modern L-PBF systems can have an overwhelming number of processing parameters to control. L-PBF manufacturers tend to limit the number of processing parameters a user can control and attempt to provide optimized processing parameters. However, due to the geometric flexibility, it is difficult to achieve a standard parameter set that will be universally optimized for every geometry and application. This has motivated significant research efforts into optimizing the AM processing parameters for specific structures or mechanical performance [7–9]. The most commonly investigated processing parameters include the laser power, laser scan speed, layer thickness, hatch distance, and scan pattern due to their direct impact on the microstructure and defects in AM metals [8]. Although these are some of the more commonly investigated parameters, as the AM field has grown, investigations into other processing parameters have rapidly expanded. Much of this research has focused on understanding the evolution of the material structure due to changing processing parameters, which is a vital link in understanding the processing-structure-property relationships.

The primary goal of this research is to improve understanding of the processing-structure-property relationships in as-built L-PBF Inconel 718 (IN718) using materials characterization and mechanical testing across multiple length scales. This dissertation consists of three main studies. The first study focuses on the high-cycle fatigue life of as-built IN718 manufactured by laser powder bed fusion and tests the hypothesis that high-cycle fatigue life is driven by two competing mechanisms: surface roughness and porosity. A comprehensive set of processing parameters was investigated, and the mechanisms driving high-cycle fatigue life in as-built L-PBF IN718 were determined [10]. The second study focuses on down selecting parameter sets from the first study to quantify the differences of pore structure, microstructure, and quasi-static tensile properties due to changes in the processing parameters using miniature tensile specimens [1]. The final study focuses on testing the hypothesis that incorporating pore-pore interactions and pore ellipticity into a void descriptor function (VDF) reported previously in the literature can serve to improve

characterization of pore structures and provide an indication of fracture location. The modified VDF is assessed using mesoscale tensile specimens machined from a subset of the L-PBF IN718 fatigue specimens tested in the first study.

1.1 Overview of processing-structure-property relationships in AM metals

One of the most vital aspects of the processing-structure-property relationships for AM metals is the porosity. In ductile metals especially, one of the most important failure mechanisms is pore coalescence and growth [11]. Recent works have begun to acknowledge the significance that porosity plays in the mechanical response in metal AM [10, 12–14]. With this recent acknowledgement, there has been a significant amount of work investigating the evolution of porosity due to AM processing parameters. Researchers have suggested there are three main types of pores that can evolve in AM metals: gas pores, keyhole pores, and lack-of-fusion pores [15]. Gas pores are commonly found in AM metals and are typically spherical. Two different mechanisms can cause the formation of gas pores: hollow powder particles and gas entrapment. With typical processes to manufacture metal powders, gases can become entrapped inside of the powder particles [16]. When the melting of the powder occurs, these entrapped gases remain in the molten pool unless they can escape. Similarly, entrapment of the shielding gases or vapors from the material can cause gas pores [17]. Keyhole pores are another type of pores commonly found in AM metals. Keyhole pores typically evolve at high levels of laser energy density, where keyholes become unstable and collapse [18–20]. Keyhole pores are typically spherical, similar to gas pores, but can have variable sizes depending on the size and shape of the keyhole prior to collapse. The third type of pore (or void) that can evolve in AM metals is caused by lack-of-fusion. Lack-of-fusion pores are irregularly shaped voids that are caused by an insufficient melting of the powder and occur in the low levels of laser energy density [21, 22]. Primarily, the lack-of-fusion pores and keyhole pores are the most sensitive to changes in the processing parameters, which leads to large variations in porosity. Additionally, the different types of pores have been shown to have different impacts on the mechanical response [20, 23–29]. For example, Hilaire et al. [30] showed that lack-of-fusion pores (irregularly shaped) created localized stress concentrations and promoted the

initiation of sharp cracks more so than spherical pores (gas pores). Additionally, Gribbin et al. [31] showed that the fatigue life of L-PBF Inconel was directly attributed to the presence of pores. Both of these works, along with many others, highlights the importance of understanding the unique evolution of porosity and its corresponding impact on the mechanical behavior in AM metals.

The microstructure of AM metals also presents a challenge in deciphering processing-structure-property relationships due to the intrinsic anisotropy and heterogeneity in the material [13]. The complex thermal history in the AM process produces unique microstructures that are generally not found in traditional metals. The microstructure in AM metals, specifically in the as-built condition, consist of columnar grains elongated in the build direction [32–35]. Additionally, common metrics characterizing the microstructure in metals may be insufficient for describing the microstructure in AM metals. A strong crystallographic texture is also typically observed in most AM metals [36–38]. Although both the grain morphology and crystallographic structure can contribute to the anisotropy in mechanical properties, the morphology likely has a larger influence on the anisotropy [39, 40]. Despite general observations regarding the microstructure in AM metals, the specific variations in microstructure are strongly dependent on the alloy and the type of AM technique used. The remaining literature review focuses specifically on IN718, and additional background is provided in Chapters 2 through 4.

Inconel is a nickel-based superalloy that has become increasingly popular specifically in the aerospace, nuclear, and marine industries due in part to its ability to retain its strength over a wide range of temperatures [41–43]. IN718, one of the most commonly used Inconel alloys, is a Ni-Cr-Fe austenitic superalloy, which has excellent mechanical properties especially at high temperatures and in corrosive environments [44]. A passivating oxide layer is created during the heating of Inconel, which provides thermal insulation and corrosion resistance, leading to maintained strength at high temperatures [45]. IN718 consists of a γ-fcc (face-centered cubic) phase, which is known as the γ-matrix, that is rich in nickel (Ni), chromium (Cr), and iron (Fe) [46]. It is a precipitation-strengthened superalloy with the main strengthening phases being the γ'-fcc and γ''-bct (body-centered tetragonal) phases, which consist of Ni_3(Al,Ti,Nb) and Ni_3Nb, respectively. The γ''-bct phase exhibits a higher degree of strengthening than the γ'-fcc phase; however, the γ''-bct

phase metastability, which is a material's ability to transform into another state, can lead to additional phases such as carbides, δ precipitates, and Laves phases. These additional phases and precipitates typically have a negative impact on the mechanical properties [47].

Traditionally, IN718 has been used in wrought, cast, and powder metallurgy applications with great success. However, the high hardness and low thermal conductivity of IN718 make it difficult and costly to machine [48–50], which can lead to tool overwear and poor surface integrity of the finished part [51]. AM techniques have shown the ability to create near-net-shaped parts, which could solve many of the machining concerns with IN718 [12]. IN718 manufactured by L-PBF methods has been shown to have similar mechanical properties to wrought IN718 [52]. Wang et al. [52] showed that the tensile strength and ductility of L-PBF IN718, which was solution treated and double aged, were comparable to those of wrought IN718. Specifically, they observed an ultimate tensile strength range of 1137-1358 MPa for L-PBF IN718 compared to 1200-1400 MPa for wrought IN718 and observed an almost identical elastic modulus of 201 GPa versus 208 GPa. However, Hilaire et al. [53] reported the influence of varying processing parameters on the microstructure, yield strength, and ultimate strength of L-PBF IN718 and concluded that the optimization of processing parameters should be performed to maximize the mechanical properties. Although L-PBF IN718 has shown similar tensile properties to those of wrought IN718, the fatigue life of L-PBF IN718 has remained a concern and has been shown to be significantly lower than that of wrought IN718 [54]. Specifically, Gribbin et al. [31] showed that the decrease in low-cycle fatigue life of heat-treated (solution treated and doubled aged) L-PBF IN718 was due to the presence of internal defects such as porosity.

Based on the above review, there is a need to better understand the relationships among laser-energy density, build orientation, pore structures, microstructures, and mechanical properties for IN718, namely in the as-built condition. The studies described in the following chapters detail the impact of processing conditions on intrinsic material structures and, in turn, their impact on bulk-scale fatigue properties (Chapter 2), microscale tensile properties (Chapter 3), and mesoscale fracture behavior (Chapter 4) for as-built L-PBF IN718.

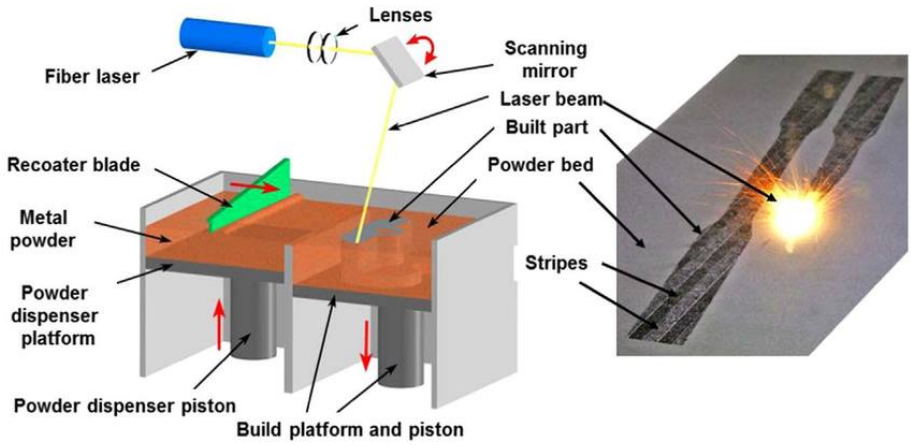

Figure 1.1. Schematic showing the laser powder bed fusion process. Taken from [55]

CHAPTER 2

MECHANISMS DRIVING HIGH-CYCLE FATIGUE LIFE OF AS-BUILT IN718 PROCESSED BY L-PBF

The contents of this chapter are adapted from the following journal article: D.S. Watring, K.C. Carter, D. Crouse, B. Raeymaekers, and A.D. Spear, "Mechanisms driving high-cycle fatigue life of as-built Inconel 718 processed by laser powder bed fusion," *Materials Science and Engineering: A*, vol. 761, p. 137993, 2019.

This study investigates the relationships among the high-cycle fatigue life, surface roughness, and additive manufacturing processing parameters in laser powder bed fusion Inconel 718 in the as-built condition. Standardized fatigue specimens were manufactured using 25 different sets of processing parameters by varying laser power, scan speed, layer thickness, and build orientation, with three repeat specimens per parameter set. Surface roughness measurements were conducted using white light interferometry, high-cycle fatigue life was measured, and fractography analysis was performed using scanning electron microscopy. Two processing-parameter metrics were observed to dominate high-cycle fatigue life: build orientation and laser-energy density. Build orientation affected fatigue life due to the relationship between build orientation and surface roughness. Increasing surface roughness decreased the fatigue life due to increasing surface-crack initiation sites. For a fixed build orientation, the laser-energy density, outside of the optimal range, decreased the fatigue life due to sub-surface defects. Specifically, fractography analysis showed that sub-surface defects consisted of lack-of-fusion pores at low laser-energy densities and secondary cracking and pores (possibly related to keyholing) at high laser-energy densities. While variability in residual stresses among the specimens could also play a role, this work focuses on geometrical surface and sub-surface defects caused by different processing parameters and their corresponding impact on total fatigue life. Based

on these findings, guidelines are offered to improve fatigue life of additively manufactured Inconel 718 in the as-built, non-heat-treated condition.

2.1 Introduction

While additive manufacturing (AM) has become a popular tool in a variety of different industries [2, 56], there remain many unknowns regarding the relationships between the build or process parameters and the corresponding quality, reliability, and the performance of the parts [57]. There are many different AM techniques used to manufacture metal parts. These techniques are typically categorized as powder bed fusion (PBF) and direct energy deposition (DED) [5]. Powder bed fusion can be separated further into laser powder bed fusion (L-PBF) [6] and electron beam melting (EBM) [58]. In L-PBF, metal powder is spread or rolled onto a build plate. A scanning laser is then used to locally melt/fuse a thin layer of metal powder to create the first layer. This is repeated layer-by-layer, until the full three-dimensional part is completed. L-PBF has many benefits over traditional manufacturing and other metal AM techniques including high accuracy in fine details, near net-shape production of complex geometries, and the ability to use a variety of metals and their alloys [4], including Inconel.

Inconel is a nickel-based superalloy that has become increasingly popular in the aerospace, nuclear, and marine industries in part to its ability to retain its strength over a wide temperature range. Particularly, Inconel shows excellent mechanical properties especially at high temperatures and in corrosive environments [44], whereas mechanical properties of aluminum and steels may degrade in such conditions [59–62]. Inconel creates a passivating oxide layer during heating, which prevents the surface from further heating and corrosion [45]. Additionally, Inconel shows an increase in strength due to solid solution and precipitation hardening [63]. One of the most commonly used Inconel alloys is 718 [43]. Inconel 718 (IN 718) shows many improved mechanical properties over other Inconel alloys. However, due to its high hardness and low thermal conductivity, it is significantly more difficult and costly to machine [48–50, 64]. AM techniques have shown the ability to create near-net shaped parts, which could solve many of the concerns with IN 718 [12]. IN 718 manufactured by L-PBF methods has been shown to have similar mechanical properties to wrought 718 [52]. Wang et al. [52] showed that the tensile strength and

ductility of selective laser melted (SLM[1]) IN 718, which was solution treated and double aged, were comparable to those of wrought 718. Specifically, they observed an ultimate tensile strength range of 1137-1358 MPa for SLM IN 718 compared to 1200-1400 MPa for wrought 718 and observed an almost identical elastic modulus of 201 GPa versus 208 GPa. However, Hilaire et al. [53] showed the influence of varying processing parameters on the microstructure, yield strength, and ultimate strength of L-PBF IN 718 and concluded that the optimization of processing parameters should be performed to maximize the mechanical properties. Although L-PBF IN 718 has similar mechanical properties to those of wrought 718, the fatigue life of L-PBF IN 718 has been shown to be significantly lower than that of wrought 718 [54]. Specifically, Gribbin et al. [31] showed that the decrease in low-cycle fatigue life of heat-treated (solution treated and doubled aged), direct metal laser sintered (DMLS[2]) IN 718 was due to the presence of porosity. Additionally, others have shown that porosity in heat-treated L-PBF IN 718 parts can be induced by varying processing parameters [26]. Thus, a thorough understanding and control of the processing parameters are required for optimizing the fatigue life in L-PBF IN 718.

The objective of this study was to examine the relationships among the AM process parameters (laser scan power, laser scan speed, layer thickness, and build orientation) for a laser powder bed fusion technique, surface roughness parameters, and high-cycle fatigue life of as-built L-PBF IN 718. Few studies exist in the open literature that have investigated the material in the as-built condition, without applying heat treatments or stress relieving. However, there are potential applications, such as deployment of AM machines in the field, where it may not be possible to perform heat treatments. To better optimize AM parts for use in such applications, there is a need to better understand the process-property relationships for the as-built condition. Therefore, the L-PBF specimens in this work had no heat treatments applied (e.g., stress relief, solution treatment, double aging, etc.). A total of 11 different laser powers, 13 different laser scan speeds, two different layer thicknesses, and three different build orientations were investigated. The high-cycle fatigue life for different combinations of AM processing parameters was determined, and the competing

---

[1]Selective laser melting (SLM) is a commonly used L-PBF technique.

[2]Direct metal laser sintering (DMLS) is another commonly used L-PBF technique.

physical mechanisms driving the fatigue life of L-PBF IN 718 were investigated.

2.2 Methods and materials

2.2.1 Materials and processing parameters

The test specimens used in this study were fabricated from 3D Systems Inconel 718 powder, which was recycled powder within 3D Systems usable standards. Analysis of the particle-size and aspect-ratio distributions of the Inconel 718 powder was performed in accordance with the ASTM F1877 standard [65]. Standardized fatigue test specimens were manufactured with a target gauge width of 6.36 mm and target gauge thickness of 3.10 mm, in accordance with the ASTM E466-15 standard [66]. Figure 2.1a shows the target dimensions of the specimens. The specimens were built using 3D Systems ProX DMP 320 machine. In total, 25 different parameter sets were defined, each having a unique combination of laser power, laser scan speed, layer thickness and build orientation. The upper and lower values for the laser power and laser scan speed were selected based on the manufacturer's specified limits. The laser power ranged from 115 W to 465 W, with 11 different values selected within that range, and the laser scan speed ranged from 620 mm/s to 1770 mm/s, with 13 incremental values selected. The values for the layer thickness were set to the ProX DMP 320 standard thicknesses: 30 μm and 60 μm. Each specimen was manufactured such that the loading axis was aligned 0°, 60°, or 90° relative to the recoater direction in the build plate, as shown in Figure 2.1b. For the purpose of this study, the hatch spacing and spot size were held constant at standard values: 100 μm and 50 μm, respectively. The entire parameter matrix can be seen in Table 2.1. Additionally, all of the 30 μm thickness specimens were built using contouring parameters of 115 W and 625 mm/s for the laser power and scan speed, whereas the 60 μm thickness specimens were built using 165 W and 625 mm/s contouring parameters. The parameter ranges were chosen such that volumetric laser-energy density (E_ρ) ranged from approximately 30 to 90 J/mm^3, based on optimal values specified by 3D Systems. The volumetric laser-energy density is $E_\rho = \frac{P}{vht}$, where P is the laser power, v is the scan speed, h is the hatch spacing, and t is the layer thickness [67]. For each parameter set, there were three fatigue specimens manufactured for a total of 75 specimens. All of the specimens were tested in the as-built condition (i.e., no post-processing or secondary heat-treatments were performed).

2.2.2 Surface roughness measurements

Surface roughness was measured in the gauge region for all 75 specimens. The surface roughness measurements were obtained using a Zeta 3D optical profilometer with a 10× objective lens. Three scans per side on all four sides of the gauge region were measured covering an area of 948 μm by 711 μm. Ten different surface roughness metrics were quantified for each specimen, namely Ra, Rms, Rt, Rsk, Rku, RzDIN, RzJIS, η, ρ, and σ_s. A description of all of the surface roughness parameters is provided in Appendix A.

2.2.3 Fatigue testing

Following surface roughness measurements, all 75 specimens were cyclically loaded (tension-tension) to failure with the maximum stress of 600 MPa, stress ratio of 0.1, and a frequency of 20 Hz. The fatigue testing parameters were chosen such that the total fatigue-life testing was in the high-cycle range (i.e. within the elastic regime) at a fixed stress amplitude, which would result in fatigue failure within a tractable number of cycles (nominally 100,000). To that end, the stress amplitude was identified using S-N curves (at R=0.1) from the literature for AM IN 718 [54]. Note that the reported yield strength of L-PBF IN 718 is between 800 MPa and 1100 MPa [68, 69], which is well above the applied peak stress. The fatigue testing was performed in force control at a frequency of 20 Hz on an MTS 810 servo-hydraulic testing machine using a 25 kN load cell. Hydraulic grips were used to hold the specimens at 20 MPa, which is approximately 3.3% of the maximum applied stress. The cross-sectional area of each specimen was measured using a Keyence VHX-5000 optical microscope, which was then used to accurately determine the load required to reach a maximum applied stress of 600 MPa.

2.2.4 Fractography

Fractography analysis was performed on each specimen after fatigue failure using a Hitachi S-2600N scanning electron microscope (SEM). Representative images for specimens with the same laser-energy density but different build orientations were analyzed to quantify the amount of fracture initiation beginning on the surfaces of the specimens. Additionally, representative images for specimens with different laser-energy densities but the same build orientation were analyzed to investigate the sub-surface defects.

2.3 Results

2.3.1 Powder characterization

Figure 2.2 shows SEM images of the IN 718 powder at low and high magnification. The majority of the powder particles are spherical or near spherical (similar to Figure 2.2b). However, some particles appeared to be partially fused (Figure 2.2c) and display an oblong morphology (Figure 2.2d). SEM images similar to that shown in Figure 2.2a were used to determine the powder particle-size distribution for a population of 534 particles, shown in Figure 2.3, which is similar to those seen in the literature [52]. The mean particle size was found to be 39.98 μm, compared to 43.8 μm reported by 3D Systems.

2.3.2 Surface roughness

A correlation study was performed to determine the roughness parameters exhibiting the strongest correlation to the high-cycle fatigue life. The methodology and results from the correlation study are presented in Appendix B. The average of three scans was taken for each side, and the maximum of the averaged values among the four sides was used to represent the overall roughness for a given specimen. Based on results from the correlation analysis, it was found that no one parameter significantly correlated with high-cycle fatigue life. Therefore, to simplify the presentation of results, only the average roughness value (Ra) will be considered and discussed. Figure 2.4 shows representative surface topography maps of each side of the specimens for each of the build orientations. For the 0° build orientation, the surface topography maps for sides three and four have been plotted using a different scale than that for sides one and two due to the significant difference in surface-roughness magnitude. The significantly higher surface roughness for side four in the 0° build orientation specimen is likely due to the supports that were needed during the printing process (see Figure 2.1b). The 90° build orientation specimens showed the next roughest surfaces with side three being the roughest (Figure 2.4c). It can be postulated that this difference in surface roughness (between sides three and four) could be caused by some mechanism attributed to the gas flow direction. The surface roughness of the 60° build orientation specimens was slightly less than the 90° specimens with the roughest side being side two, which can be attributed to the downskin of the specimen.

2.3.3 Fatigue life

Figure 2.5 shows the fatigue life as a function of the different sets of process parameters, by comparing the total fatigue life to the volumetric laser-energy density for different layer thickness and build orientation. For a fixed build orientation, the total fatigue life presented in Figure 2.5a exhibits a bell-shaped relationship with the laser-energy densities, which tend to result in lower total fatigue life for lower and higher laser-energy densities. Figure 2.5b shows a similar trend, although it is less pronounced. It is noted that one specimen for the 60 μm, 90° build orientation, and lowest energy density showed visual signs of damage prior to loading. Namely, it showed significant warping, which could be due to residual stresses from the manufacturing process, and notches on the edges, which could be due to removing the support structures. Therefore, it was considered an outlier and was not included in the trend line shown for that data set. Overall, the specimens built at a 60° build orientation with a laser-energy density of 62.15 J/mm^3 and 30 μm thickness resulted in the maximum total fatigue life among all parameter sets considered in this study.

2.3.4 Fractography

Figure 2.6 shows the fracture surfaces of nine test specimens selected from 30 μm layer thickness at three different laser-energy densities from each build orientation: 45 J/mm^3, 62 J/mm^3, and 77 J/mm^3. The middle column corresponds to specimens displaying the highest total fatigue life (62 J/mm^3 laser-energy density). In the first column (45 J/mm^3), there is consistently a very tortuous fracture surface compared to the other laser-energy densities, which is indicative of a high amount of porosity or defects. Figure 2.7 shows higher magnification images that revealed the majority of these defects consisted of lack-of-fusion pores with powder particles present. Additionally, Figure 2.7 shows a significant amount of secondary cracking and pores at high laser-energy densities. Figure 2.8 shows lower magnification images displaying the transition from stable crack growth to final fracture. The relative portion of stable crack-growth area per cross section is approximately 49.25% for the 0° specimen, 76.71% for the 60° specimens, and 52.58% of the 90° specimens. Similar trends were observed in the 60 μm layer thickness specimens.

The main difference among the three build orientations was the number of crack initi-

ation sites observed on the specimen surfaces. Surface-crack initiation sites were observed in all three specimens; however, there were significantly more surface-crack initiation sites observed in the 0° build orientation specimens, fewer in the 90° specimens, and the fewest in the 60° specimens. Figure 2.9 shows representative images of surface-crack initiation sites. Surface-crack initiation predominantly occurred on sides three and four, which corresponded to the roughest surfaces. There were approximately 63% more occurrences of surface-crack initiation sites for the 0° specimens compared to the 60° specimens and approximately 29% more in the 90° specimens compared to the 60° specimens (all for the 30 μm layer thickness). Table 2.2 shows the number of surface-crack initiation sites observed on the surface of each specimen.

2.4 Discussion

To facilitate the use of L-PBF IN 718 in fatigue critical applications, it is paramount to understand the mechanisms that determine the fatigue life of L-PBF IN 718. In this work, two different relationships were observed: the relationship between surface roughness and high-cycle fatigue life, and the relationship between laser-energy density and high-cycle fatigue life.

2.4.1 Relationship between build orientation, surface roughness, and high-cycle fatigue life

The results from sections 3.2 and 3.3 are synthesized in Figure 2.10, which shows the maximum surface roughness, the high-cycle fatigue life, and build orientation for each specimen. It is evident that fatigue life is dependent upon surface roughness, which is dependent upon the build orientation. The 0° build orientation exhibits rougher surfaces and generally results in lower fatigue life. On the other hand, the 60° build orientation, which Figure 2.5 shows to provide the highest values of fatigue life, exhibits low surface roughness. While increasing surface roughness is generally regarded to decrease fatigue life, a question of interest is whether stress concentrations associated with AM-induced surface roughness increases the number of crack initiation sites, or whether the number of crack initiation sites is approximately the same but have earlier onsets. To investigate this, the fracture surfaces were carefully analyzed. The 0° build orientation specimens showed significantly more surface-crack initiation sites; whereas, for the surfaces with

lower roughness values, fewer surface-crack initiation sites existed. Figure 2.8 shows overviews of representative surfaces of the three different build orientations at identical laser-energy densities. There were approximately 60% more crack initiation sites on the surfaces for the 0° build orientation compared to the 60° build orientation for the 30 μm layer thickness. Others have demonstrated that multiple initiation sites lead to higher crack driving forces [70–73], which can lead to increased crack growth rates. The 0° build orientation had the lowest high-cycle fatigue life and the highest number of surface cracks. Therefore, it can be inferred that the number of crack initiation sites impacts the crack growth rates, reducing the number of cycles to reach fracture (propagation cycles). Additionally, it can be postulated that some of the reduction in fatigue life could be due to early onset of crack initiation. Spear et al. [74] have shown that early initiation of fatigue cracks can be caused by local, pit-induced, stress concentrations. The reduction of fatigue life in the specimens with higher surface roughness can hence be attributed to a reduction in the propagation cycles due to a higher amount of crack initiation sites and a reduction in the cycles to initiation due to local stress concentrations on the surface.

Other work has been performed investigating the surface roughness and fatigue life of L-PBF IN 718. In that work, Gockel et al. [9] held the build orientation constant while varying contour power and scan speed of the fatigue specimens. They showed limited correlation between surface roughness (Ra) and fatigue life, which they attributed to powder particles on the surface that essentially obfuscate the underlying, more important, surface features. While Gockel et al. show that parameters like Ra might not adequately characterize fatigue-critical surface features, the results from this work suggest that Ra, nonetheless, exhibits meaningful correlation with fatigue life for the ranges of specimens studied here. One reason for this could be the variability of surface roughness that is introduced by varying build orientation, which has a clear impact on fatigue life. That is, due to significant variation of Ra values across all 75 specimens, the correlation coefficients with fatigue life are relatively high. Based on work by Gockel et al., it appears that using a more accurate description of relevant surface structure would lead to even stronger correlation coefficients. Testing this would require the use of X-ray computed tomography, which is beyond the scope of the current study; additionally, the overall trends presented in this work are not expected to vary by doing so.

Despite the clear trends among build orientation, surface roughness, and fatigue life, there does not appear to be a clear trend between surface roughness and fatigue life for a fixed build orientation (Figure 2.10). This suggests that another mechanism must also play a role in the high-cycle fatigue life of L-PBF IN 718. To investigate the mechanism behind this variation, an analysis of the sub-surface defects was performed.

2.4.2 Relationship between the laser-energy density and the high-cycle fatigue life

From sections 3.3 and 3.4, it is evident that for a fixed build orientation, fatigue life is strongly dependent on sub-surface defect structure, which is, in turn, dependent upon volumetric laser-energy density. Sheridan et al. [26] have shown that for machined L-PBF IN 718 parts, the porosity can be induced by varying the processing parameters, which ultimately determines the fatigue life. The parameters that Sheridan et al. investigated were the power, velocity, hatch spacing, and layer thickness, which directly relate to the laser-energy density, for two different machines (Concept laser M2 cusing and EOS M290); however, a large range of laser-energy density was not investigated (only one value for the M2 and three values for the EOS M290). Furthermore, the relationship between the volumetric laser-energy density and the high-cycle fatigue life is more complicated than the relationship between the surface roughness and fatigue life. A bell-shaped curve relates the fatigue life to laser-energy density. A similar curve was observed in previous work when comparing porosity and laser-energy density [75, 76]. Kantzos et al. [77] have shown that the introduction of porosity due to varying processing parameters reduce the fatigue life. For this specific AM process, an optimal range of volumetric laser-energy density exists where the sub-surface defects (secondary cracking, porosity) are minimum, and the high-cycle fatigue life is maximum. The optimal range was around 60 to 70 J/mm^3 and 40 to 45 J/mm^3 for the 30 μm and 60 μm layer thickness specimens, respectively. At lower values of laser-energy density, the high-cycle fatigue life is significantly reduced. Similarly, the high-cycle fatigue life is significantly reduced at higher laser-energy densities.

The fractography analysis shows that in the low laser-energy density ranges, there was a very tortuous fracture surface indicative of a high amount of porosity. The porosity and sub-surface defects in the low energy density ranges are predominantly due to lack-of-fusion pores (Figure 2.7). Typically, three to five Inconel particles were present in these

lack-of-fusion pores, but fracture initiation was observed to begin at larger clusters of particles. However, the fractography analysis for the high laser-energy density specimens showed different sub-surface defects than the low laser-energy densities. There was a significant amount of secondary cracking observed (seen in Figure 2.7) along with fracture initiating at sub-surface porosity. This could be due to keyhole (or other metallurgical) pores [21]. The secondary cracking observed could be due to a similar mechanism to hot cracking [78], hot tearing [79], or liquation cracking [80]. Hot cracking is caused by a high grain misorientation and hot tearing is caused by high residual stresses due to high temperature gradients. Chen et al. [80] concluded that liquation cracking in additive IN 718 is due to the liquation of Laves/γ particles during manufacturing. They also observed that an increase in the heat input, due to processing parameters, showed an increase in susceptibility to liquation cracking, which can be compared to the increase in cracking observed in this work with an increase in the laser-energy density.

The fatigue behavior of L-PBF IN 718 presented in this study is consistent with literature showing that fatigue life in metals is typically driven by surface and sub-surface defects [81–84]. The main contribution of this work is the establishment of links among L-PBF build parameters and high-cycle fatigue-driving mechanisms, considering a broad space of build parameters. The mechanism of fracture initiation at surface defects is dominated by the surface roughness, which is predominantly governed by build orientation. For a given build orientation, the fatigue life is driven by the sub-surface defects in AM metals due to a high amount of lack-of-fusion pores at low laser-energy densities and metallurgical porosity at high laser-energy densities. The sub-surface defects are predominantly associated with the laser process parameters: laser power, scan speed, hatch spacing, and layer thickness. Although the results from the correlation analysis showed that no one parameter significantly correlated with high-cycle fatigue life, there could be factors leading to this perceived weak correlation. Outside of the optimal range of laser-energy density, there is significant near-surface porosity that may be contributing to the weak correlation. A separate Pearson correlation analysis was performed among the fatigue life, Ra values, and Rms values using only the specimens in the optimal laser-energy density range. The results showed approximately a 33% increase in the magnitude of correlation coefficient for Ra (-0.571 to -0.763) and a 29% increase in the magnitude of

correlation coefficient for Rms (-0.565 to -0.730). Additionally, the residual stresses due to the different laser-energy densities and build orientations may have influenced the fatigue results, thereby further impacting the correlation coefficients. While it is noted that variability in residual stresses induced by the L-PBF process also likely contributes to variability in fatigue life, the work presented here focuses on geometrical surface and sub-surface defects induced by the L-PBF process and their corresponding impact on total fatigue life.

2.5 Conclusion

In this study, a systematic design of experiments was performed to investigate the relationships among process parameters, surface roughness, and the high-cycle fatigue life in L-PBF IN 718. Based on the experimental fatigue results and fractography, the following conclusions are made:

1. In the high-cycle fatigue life of L-PBF IN 718, there are two competing mechanisms that influence the fatigue life. The first mechanism is due to the relationship between the surface roughness and the high-cycle fatigue life. The surface roughness causes an increase in the number of surface-crack initiation sites, which reduces the fatigue life. The second mechanism is due to the relationship between the volumetric laser-energy density and the high-cycle fatigue life, which causes an increase in sub-surface defects.

2. The worst total fatigue life was observed for the 0° build orientation specimens, while the 60° build orientation specimens showed the highest total fatigue life. The fractography analysis shows that fracture initiation sites occur predominantly on the surfaces of specimens for the 0° build orientation specimens with significantly fewer surface-crack initiation sites on the 90° and 60° build orientation specimens. Hence, the fatigue life is driven by the surface roughness. The surface roughness contributes to the possible number of fracture initiation locations on the surface of the specimen, which is predominantly due to the build orientation. The reduction in fatigue life is due to higher crack propagation rates caused by an increased number of surface-crack initiation sites.

3. The total fatigue life within a specific build orientation follows a bell-shaped curve. There is an optimal laser-energy density, depending on the layer thickness, for the total fatigue life. For the 30 μm layer thickness, this value is around 60 to 70 J/mm^3. For the 60 μm layer thickness, it is around 40 to 45 J/mm^3. This is consistent with previous work showing that at low and high values of energy densities, there is an increased amount of sub-surface porosity and defects. The laser-energy density drives the amount of sub-surface pores and defects, which ultimately drives the total fatigue life within a given build orientation. At low volumetric laser-energy density ranges, the sub-surface defects consist of lack-of-fusion pores. At high volumetric laser-energy density ranges, the sub-surface defects consist of keyhole (or other metallurgical) pores and secondary cracking possibly caused by a hot tearing like mechanism.

4. Similar to traditional materials, the total fatigue life in AM Inconel is dominated by surface and sub-surface defects. Residual stresses may also affect the high-cycle fatigue life, but were not investigated in this work. From this work, however, the conclusion can be made that to maximize the total fatigue life in as-built L-PBF IN 718, the manufacturing process should minimize the sub-surface defects through process parameter optimization (specifically the laser power, scan speed, hatch spacing, and layer thickness) and also minimize the surface roughness through build orientation or machining when possible.

Table 2.1. Test matrix for L-PBF IN 718 processing parameter sets. For each parameter set, three specimens were manufactured and tested.

Parameter set	**Power** (W)	**Scan speed** (mm/s)	**Layer thickness** (μm)	**Build orientation** ($^\circ$)	**Laser-energy density** (J/mm^3)
1	220	1180	30	60	62.15
2	330	1770	30	0	62.15
3	115	620	30	90	61.83
4	168	1475	30	0	37.97
5	275	1200	30	0	76.39
6	115	915	30	60	41.89
7	330	1475	30	60	74.58
8	168	1180	30	90	47.46
9	200	800	30	90	83.33
10	275	1770	30	60	51.79
11	315	1050	60	60	50.00
12	465	1450	60	0	53.45
13	240	850	60	90	47.06
14	165	850	60	0	32.35
15	390	1050	60	60	61.90
16	465	1400	60	90	55.36
17	165	650	60	0	42.31
18	240	1250	60	60	32.00
19	315	1250	60	60	42.00
20	390	1450	60	90	44.83
21	220	1180	30	0	62.15
22	220	1180	30	90	62.15
23	315	1050	60	0	50.00
24	315	1050	60	90	50.00
25	200	1000	60	90	33.33

Table 2.2. Number of observed surface-crack initiation sites from one representative sample at each build orientation.

Build orientation	**Medium laser-energy density**
0°	57
60°	35
90°	45

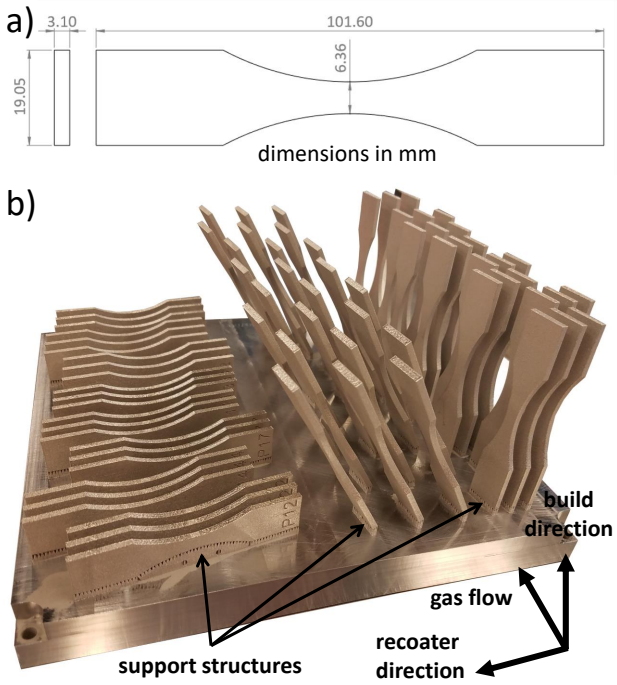

Figure 2.1. Manufactured specimens. a) Specimen dimensions in accordance with ASTM E466-15. b) All as-built IN 718 specimens on the build plate prior to removal with support structures shown.

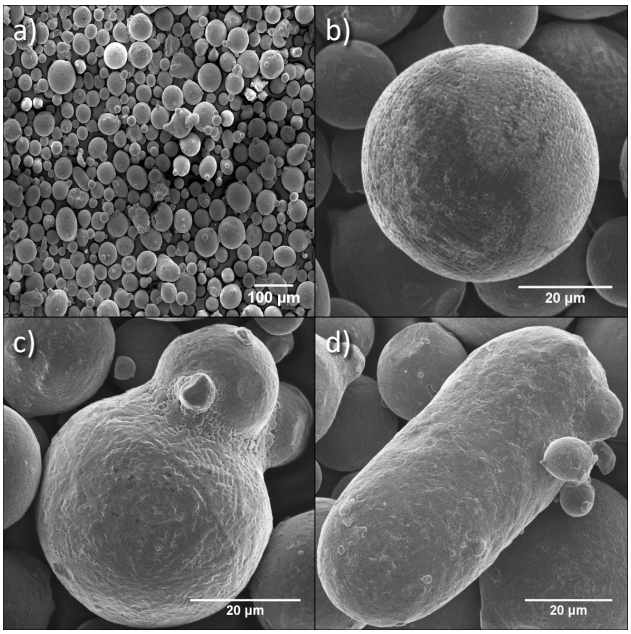

Figure 2.2. Representative SEM images of IN 718 powder particles showing a) an overview, b) perfectly spherical particles, c) partially fused particles, and d) oblong shaped particles.

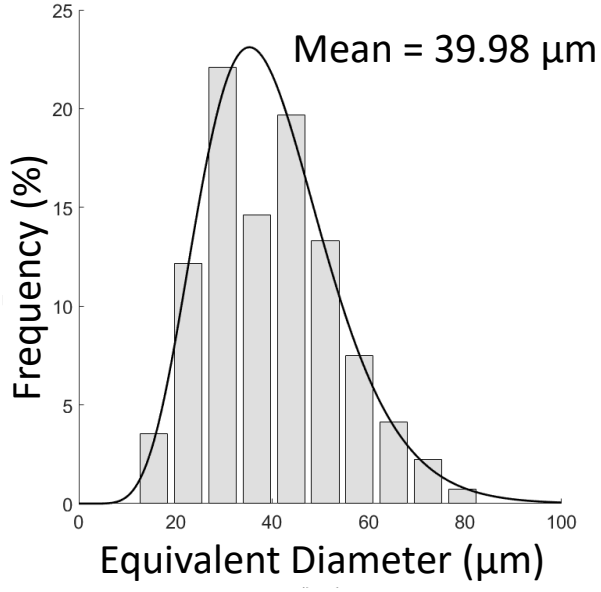

Figure 2.3. Inconel 718 powder particle size distribution determined using SEM particle mapping.

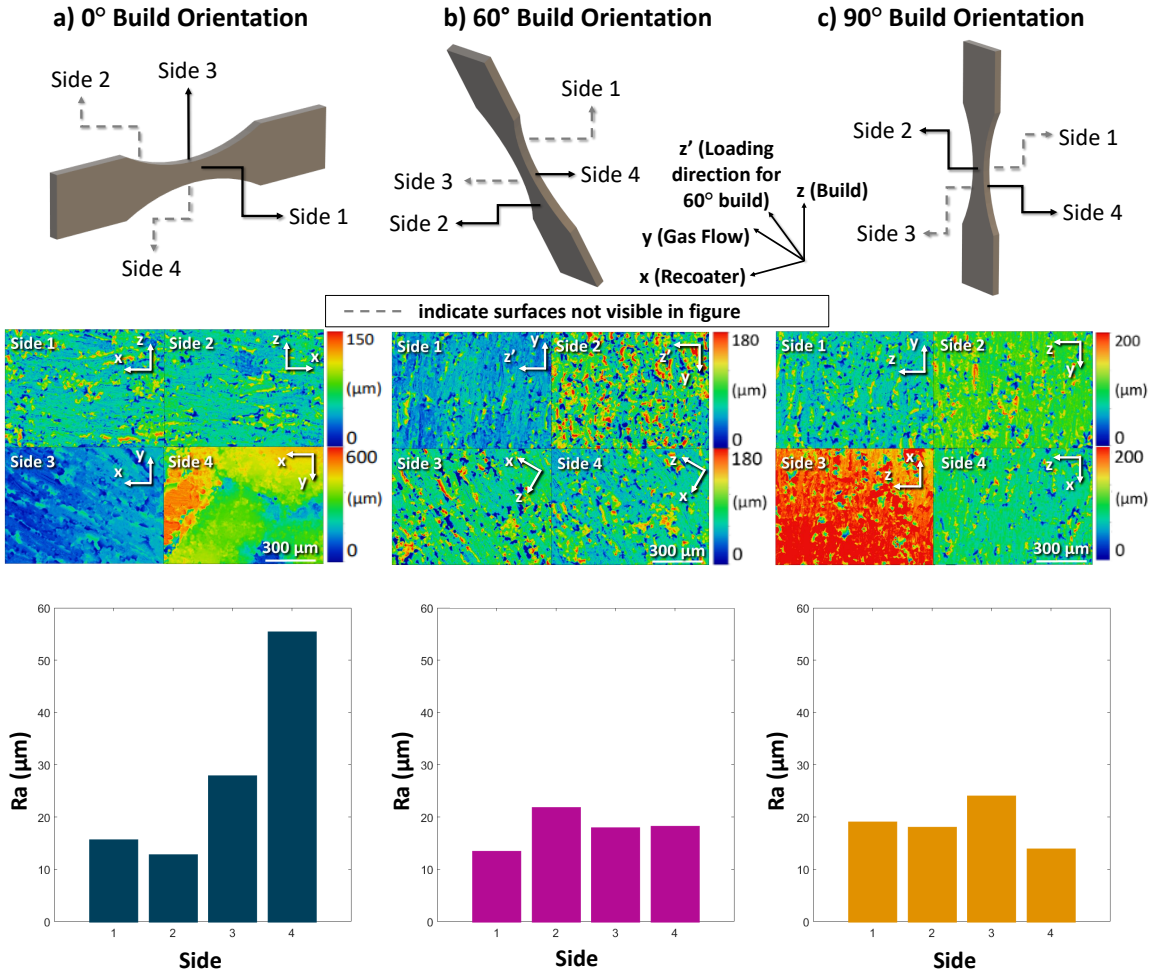

Figure 2.4. Representative surface topography maps and Ra values for a) 0° build orientation, b) 60° build orientation, and c) 90° build orientation. Note, contour limits for the maps are scaled differently to enable visual contrast for each surface.

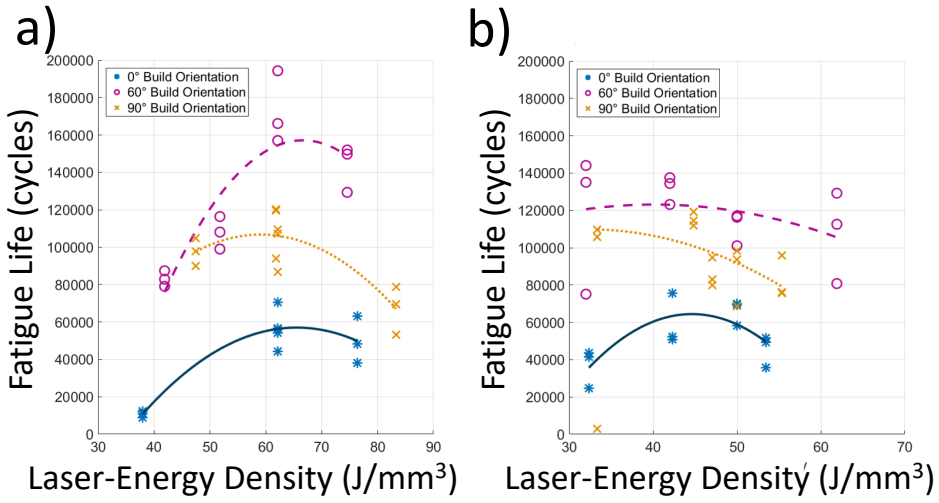

Figure 2.5. High-cycle fatigue life versus volumetric laser-energy density for a) 30 μm layer thickness specimens and b) 60 μm layer thickness specimens.

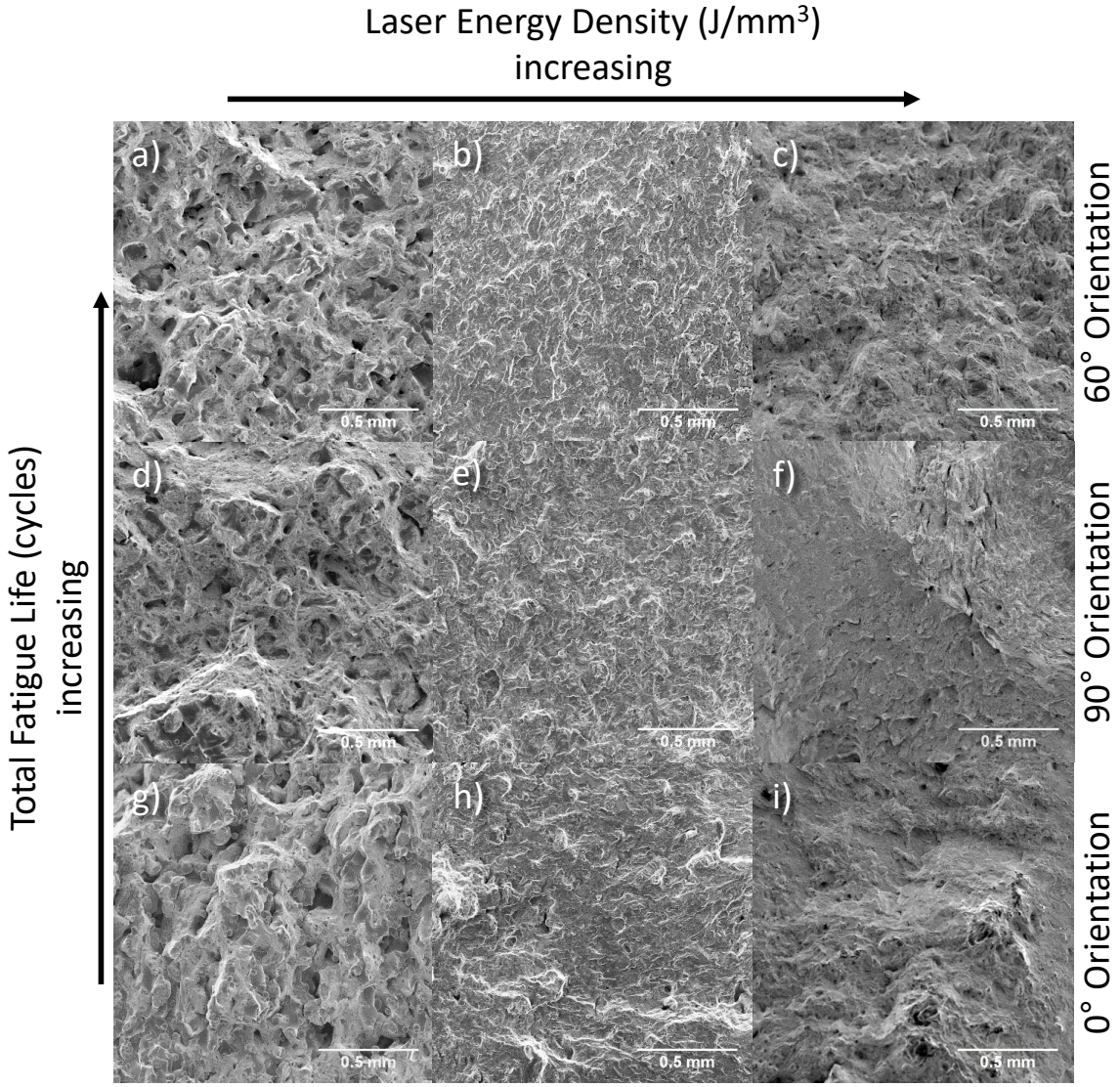

Figure 2.6. SEM images of fracture surfaces of high-cycle fatigue tested L-PBF IN 718 for 30 μm at a) 45 J/mm^3 and 60° build orientation, b) 62 J/mm^3 and 60° build orientation, c) 77 J/mm^3 and 60° build orientation, d) 45 J/mm^3 and 90° build orientation, e) 62 J/mm^3 and 90° build orientation, f) 77 J/mm^3 and 90° build orientation, g) 45 J/mm^3 and 0° build orientation, h) 62 J/mm^3 and 0° build orientation, i) 72 J/mm^3 and 0° build orientation.

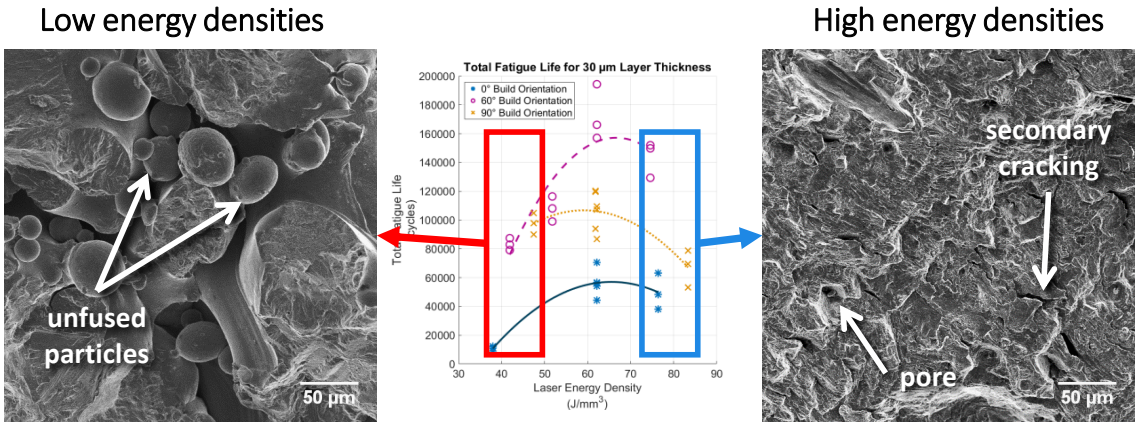

Figure 2.7. High-cycle fatigue life dependence on sub-surface defects.

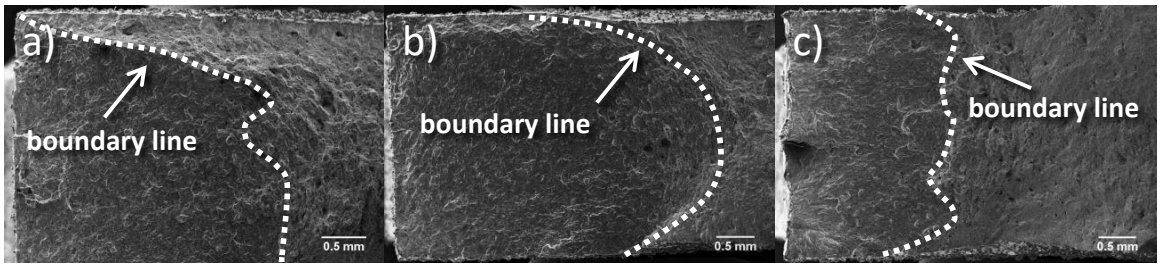

Figure 2.8. Representative SEM images of fracture surfaces showing stable crack growth (left of the boundary line) and final fracture region (right of the boundary line) for 30 μm layer thickness: a) 0° specimen with N_f = 70523 cycles, b) 60° specimen with N_f = 194329 cycles, and c) 90° specimen with N_f = 120255 cycles.

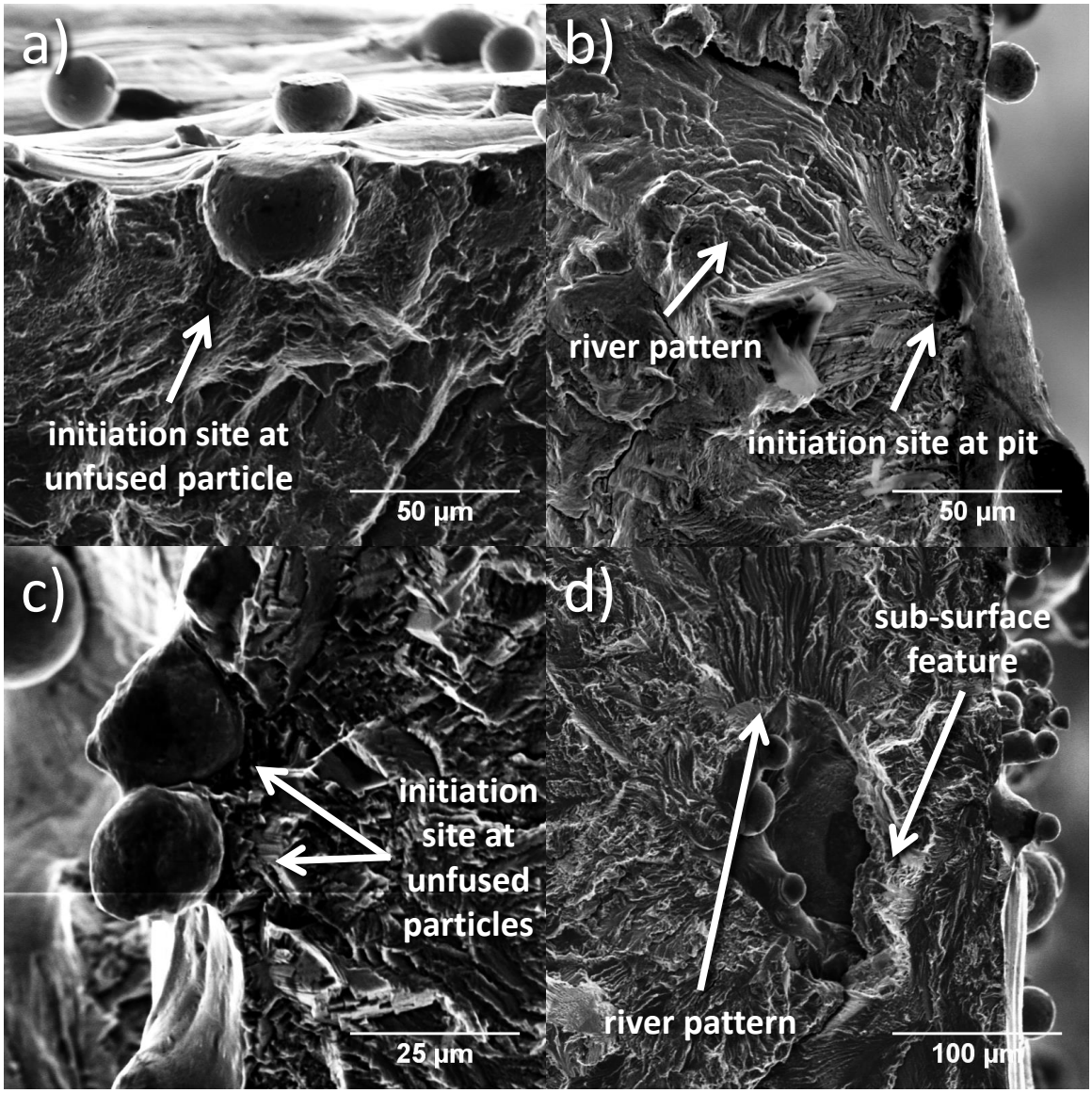

Figure 2.9. Representative SEM images of surface cracks for a) 60° specimens, b) 90° specimens, c) 0° specimens, and d) a representative sub-surface initiation site.

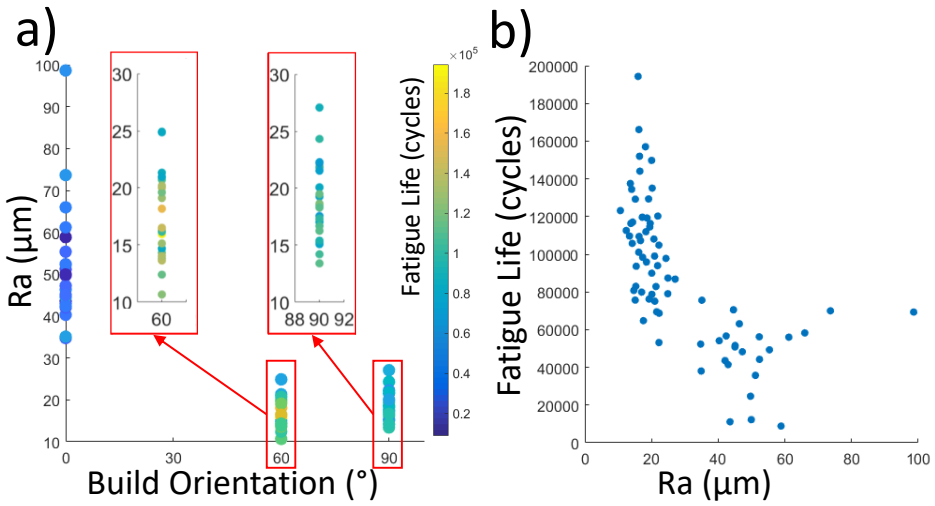

Figure 2.10. Build orientation versus Ra values. a) Relationship among high-cycle fatigue life, roughness average parameter (Ra), and the build orientation for all three build orientations (n=75 samples). Magnified views are shown for 60° and 90° build orientations. b) Relationship between the high-cycle fatigue life and Ra for all 75 samples.

CHAPTER 3

EFFECTS OF LASER-ENERGY DENSITY AND BUILD ORIENTATION ON STRUCTURE-PROPERTY RELATIONSHIPS IN AS-BUILT L-PBF IN718

The contents of this chapter are adapted from the following journal article: D.S. Watring, J.T. Benzing, N. Hrabe, and A.D. Spear, "Effects of laser-energy density and build orientation on the structure–property relationships in as-built Inconel 718 manufactured by laser powder bed fusion," *Additive Manufacturing*, vol. 36, p.101425, 2020.

This study investigates the effects of build orientation and laser-energy density on the pore structure, microstructure, and tensile properties of Inconel 718 manufactured by laser powder bed fusion. Three different build conditions were selected for comparison based on previous research (namely, the conditions that resulted in the worst and best fatigue lifetimes): 0° build orientation and 38 J/mm^3 laser-energy density, 0° build orientation and 62 J/mm^3 laser-energy density, and 60° build orientation and 62 J/mm^3 laser-energy density. Differences in porosity were measured between each build condition. In terms of microstructure, all three conditions exhibited a predominantly $\langle 001 \rangle$ texture in the build direction, grains elongated in the build direction, and a sub-grain structure oriented with the build direction that consisted of dislocation networks decorated with nano-scale precipitates. Build orientation (0° versus 60° with respect to the build plate) produced a difference in yield strength due to anisotropic grain morphology and effective grain size. The low laser-energy density specimens showed a significant decrease in all mechanical properties compared to the high laser-energy density specimens because the amount (6.91 % by volume) and size of the lack-of-fusion porosity (from insufficient melting) surpassed a level at which microstructure (the grain and sub-grain structure) no longer governs quasi-static mechanical properties. This work provides insight that

could enable the tunability of structure-property relationships in as-built Inconel 718 by optimizing laser-energy density and build orientation.

3.1 Introduction

Nickel-based superalloys have become increasingly popular in the aerospace, nuclear, and marine industries [41, 42]. Specifically, one nickel-based superalloy, Inconel, has become an alloy of choice in many applications due in part to its ability to retain high strength over a wide range of temperatures [43]. Inconel 718 (IN718), one of the most commonly used Inconel alloys, is a Ni-Cr-Fe austenitic superalloy, which has excellent mechanical properties especially at high temperatures and in corrosive environments [44]. A passivating oxide layer is created during the heating of Inconel, which provides some thermal insulation and corrosion resistance, leading to a maintained strength at high temperatures [45]. IN718 consists of a γ-fcc phase, known as the γ-matrix, that is rich in Ni, Cr, and Fe [46]. IN718 is also a precipitation-strengthened superalloy with the main strengthening phases being the γ'-fcc and γ''-bct phases, which consist of Ni_3(Al,Ti,Nb) and Ni_3Nb, respectively. The γ''-bct phase exhibits a higher degree of strengthening than the γ'-fcc phase, but the γ''-bct phase metastability can lead to additional phases such as carbides, δ precipitates, and Laves phases. Traditionally, IN718 has been used in wrought, cast, and powder metallurgy applications with great success. However, the high hardness and low thermal conductivity of IN718 make it difficult and costly to machine [48–50], which leads to tool over-wear and poor surface integrity of the finished part [51]. Additive manufacturing techniques, which can create near-net shaped parts, could be a solution to some of the machining concerns associated with IN718.

Additive manufacturing (AM) has quickly become a popular tool in a variety of different industries [2, 85, 86]. Some of the benefits of AM techniques over traditional manufacturing include the ability to achieve high accuracy in fine details, reduced manufacturing time, and the ability to use a variety of metals and their alloys [4]. One of the most commonly used AM processes is laser powder bed fusion (L-PBF[1]) [87, 88]. In this method, metal powder is first spread or rolled onto a build plate. A scanning laser is used to locally

[1]Many of the works referenced throughout this manuscript use the terms selective laser melting (SLM) or direct metal laser sintering (DMLS); however, to be consistent with ASTM standards, these terms have been replaced by L-PBF in this manuscript.

melt/fuse a thin layer of the metal powder. This is repeated layer-by-layer to create a three-dimensional solid structure [4]. Although AM techniques address many concerns and issues associated with machining IN718 [12], challenges still arise during the L-PBF process, including variations in NbC fractions and porosity with respect to build height [89].

There has been a large amount of research done investigating the porosity in L-PBF metals (e.g., [23–25, 90]). For example, it has been found that varying laser-energy density leads to differences in the porosity and fatigue life of L-PBF IN718 [26]. Pores in AM components are typically classified into three main categories: gas pores, keyhole pores, and lack-of-fusion (LOF) pores [15]. While hot isostatic pressing (HIP) can significantly decrease porosity in AM builds [68, 91, 92], HIP requires an application of high heat and pressure, which may not be possible in certain situations, depending on the size of the component or availability of such equipment in field applications.

The microstructure of IN718 manufactured by L-PBF also presents a challenge in deciphering processing-structure-property relationships. The typical microstructure of as-built L-PBF IN718 consists of grains with an anisotropic morphology. However, there has been little work investigating the variation of the as-built microstructure due to varying processing parameters. Additionally, dendritic sub-grain structures that are slender and uniformly distributed have been observed in the microstructure. These sub-grain structures have been shown to exist in metal alloys produced by laser-based manufacturing, and their characteristics can vary depending on the applied laser-energy density [93, 94]. Moreover, previous work has shown that for L-PBF stainless steels, the sub-grain structures showed a strengthening effect [95, 96]. While carbides and oxides reside along the sub-grain boundaries (mainly from Nb segregation during the L-PBF process) [97], the main strengthening phases of IN718 (γ'-fcc and γ''-bct) are usually produced after appropriate heat treatment and slow cooling [98, 99]. However, when standard heat treatments are applied to L-PBF IN718, unwanted phases can precipitate (the δ phase in particular) and negatively impact mechanical properties [47, 100, 101]. Also, traditional heat treatments tend to completely erase the elongated grain morphology and the sub-grain structures. Recent research efforts have focused on tailoring heat treatments to retain the sub-grain structures in AM IN718 [97] since the sub-grain structures in L-PBF IN718 exhibit a positive impact on creep re-

sistance [102]. Another example of maintaining elongated grain morphology includes the work from Amato et al. [68], which showed that a specific HIP treatment of L-PBF IN718 still produced grains elongated in the build direction, plus a large amount of γ' and γ''.

Previous work by the authors showed that laser-energy density and build orientation had a significant influence on the high-cycle fatigue life of as-built L-PBF IN718 [10]. However, there was no investigation into the influence of the laser-energy density and build orientation on the variability of the three-dimensional pore structure and microstructure. Therefore, build conditions were selected from the previous work [10] to investigate the extreme cases of fatigue (i.e., the highest and lowest fatigue lifetimes) while considering differences in laser-energy density and build orientation. The objective of this study is to quantify the three-dimensional pore structure, microstructure, and quasi-static tensile properties for three different build conditions selected among the previously tested conditions [10]: 0° build orientation and 38 J/mm^3 laser-energy density (the absolute lowest fatigue life), 0° build orientation and 62 J/mm^3 laser-energy density (the lowest fatigue life for that specific laser-energy density and the highest fatigue life for that specific build orientation), and 60° build orientation and 62 J/mm^3 laser-energy density (the absolute greatest fatigue life). Although there have been previous investigations of microstructure and pore structure in L-PBF IN718, few studies exist in the open literature that have investigated the material in the as-built condition (without heat treatments or stress relieving) and the corresponding variability of the pore structure, microstructure, and tensile properties. However, the as-built condition of L-PBF IN718 is an important condition to study due to potential applications, such as deployment of AM machines in the field, where it may not be possible to perform heat treatments. Furthermore, the as-built condition contains two potentially advantageous and unique microstructural features. First, there is a lack of the deleterious δ phase that is commonly found in the stress-relieved condition. Second, the as-built condition contains a sub-grain structure that has been shown to benefit mechanical behavior in other AM material systems, and this sub-grain structure is eliminated during homogenization heat treatments. Thus, to better optimize AM parts for use in such applications, there is a need to better understand the relationships among laser-energy density, build orientation, pore structure, microstructure, and tensile properties for the as-built condition.

3.2 Material and methods

3.2.1 Build parameters and tension testing

In this study, three build conditions were selected among 25 candidate build conditions that were examined previously by the authors [10], in which ASTM E466-15 standard fatigue specimens [66] were fabricated using a 3D Systems ProX DMP 320 machine and IN718 powder. The entire build plate from the previous work is shown in Figure 3.1a. The three build conditions were selected that resulted in the extreme cases of fatigue life and also exhibited variability in the build orientation and laser-energy density. The laser-energy density can be calculated by $E_\rho = \frac{P}{vht}$, where P is the laser power, v is the scan speed, h is the hatch spacing, and t is the layer thickness [67]. The values of the laser power and scan speed of the three build conditions are provided in Table 3.1. Build orientation is reported with respect to the build plate. The first build condition had a 0° build orientation and a 38 J/mm^3 laser-energy density. The second build condition had a 0° build orientation and a 62 J/mm^3. The final build condition had a 60° build orientation and a 62 J/mm^3 laser-energy density. For all three conditions, the layer thickness (30 μm) and hatch spacing (100 μm) were held constant using standard values.

Grip sections of nine specimens, which were tested in the previous work [10], were used in this study. Each grip section was thinned from 3.18 mm to 1 mm (Figure 3.1c) using wire electrical discharge machining (wire-EDM). Four tensile specimens were excised from each of the 1 mm-thick wafers using wire-EDM (target dimensions provided in Figure 3.1d). Twelve tensile specimens were extracted for each build condition (36 total). However, four specimens were lost from the third build condition due to non-optimized settings on the first attempt with the wire-EDM process, so a total of 32 tensile specimens were available for this study. The tensile specimens were loaded to failure in uniaxial tension at a strain rate of 1 x 10^{-3} s^{-1}. The linear portion of the stress-strain curve was fit in accordance with ASTM E3076-18 [103] to calculate Young's modulus. The other tensile properties (yield strength, ultimate tensile strength, uniform elongation, and elongation at fracture) were found according to practices recommended in ASTM E8-16a [104]. An analysis of variance (ANOVA) was completed with InStat software and used to test the null hypotheses that the tensile properties were equal across the three build conditions; significance is defined as $p < 0.01$.

3.2.2 X-ray computed tomography and electron microscopy

Prior to tensile testing, one specimen from each build condition was analyzed in the gauge region to characterize potential differences in the three-dimensional pore structures. A Zeiss Xradia Versa 520 X-ray computed tomography (CT) machine (160 kV, 10 W, 1 μm voxel size) was used to measure the pore structure. The X-ray CT allowed for a visual reconstruction and quantification of the pore structures. The ImageJ (FIJI) 3D Objects Counter was used to quantify the pore sizes and morphologies from the image stacks obtained by X-ray CT [105]. Currently, in AM processes, there are three main classifications of pores: gas pores, lack-of-fusion (LOF) pores, and keyhole pores [15]. The pores in this study were classified by aspect ratios, which is the ratio of the minor axis to the major axis of the best fitting ellipse of the pore. The pores were classified as either a gas pore (aspect ratio greater than 0.5) or a LOF pore (aspect ratio less than or equal to 0.5). There is a threshold of laser-energy density, which is typically higher than the optimal laser-energy density, above which an increase in keyhole porosity results [18, 20]. In the current work, the laser-energy density for the three build conditions likely does not surpass this threshold, so no classification of keyhole porosity was performed. Additionally, an equivalent spherical diameter was determined by calculating the diameter of a sphere of equivalent volume of the pore. Finally, a relative, volumetric density of the specimen was calculated using the total volume of the CT scan and the total volume of the pores.

A specimen from each build condition was sectioned in three orthogonal directions (with respect to the loading direction), ground with SiC paper (400 grit through 1200 grit), polished with suspensions of 3 μm and 1 μm diamond particles, and finished with a vibratory polish using 50 nm colloidal silica. Backscattered electron (BSE) images were acquired using a field-emission scanning electron microscope (FE-SEM) at 20 kV, 60 μm aperture, and a 7.8 mm working distance. Electron backscatter diffraction (EBSD) measurements were conducted in an FE-SEM (20 kV, 120 μm aperture, 7.8 nA probe current, and 19.0 mm working distance) using a 0.50 μm step size. EBSD measurements were cleaned with standard practices in the TSL OIM Analysis software (v7) to remove points with a low confidence index (primarily occurring in the lack-of-fusion regions). Energy dispersive spectroscopy (EDS) line scans were carried out in an FE-SEM with a 1 nm step size and a 6 kV accelerating voltage to minimize interaction volume but maintain

sufficient excitation energy. Following mechanical testing, fractography was performed using a thermionic emission SEM (20 kV and a 19 mm working distance) and a secondary electron (SE) detector.

3.3 Results

3.3.1 Characterization of as-received material

X-ray CT was used to quantify differences in porosity among the three build conditions. Visual reconstructions of the pore structure are shown in Figure 3.2a-c. The reconstructions capture only the gas porosity (i.e., the small, spherical pores) and the LOF porosity (i.e., the large, non-spherical pores). The LOF pores were defined as those having an aspect ratio of less than 0.5, which indicates non-sphericity. The remaining pores, which were more spherical, were classified as gas pores. Quantifying both the gas porosity and the LOF porosity using equivalent spherical diameter allows for the relative frequency with respect to pore size to be compared in Figure 3.2d. The specimen built at 0° orientation with a 38 J/mm^3 laser-energy density contained significantly more porosity than the other two build conditions. This porosity was dominated by LOF pores. Additionally, the specimen built at 0° orientation with a 62 J/mm^3 laser-energy density had more LOF porosity than the specimen built at 60° orientation with the same laser-energy density (62 J/mm^3). As shown in the pore-frequency plot in Figure 3.2d, all three build conditions exhibited similar frequency of pore sizes for pores classified as gas porosity. In all three build conditions, the spherical gas porosity constitutes less than 0.3% of the entire sample volume (Table 3.2). Additionally, the LOF porosity for the first build condition (0° and 38 J/mm^3) comprises a small number of very large sized pores (greater than 75 μm in diameter). Although the X-ray CT visual reconstructions of porosity show a large amount of porosity, the two build conditions manufactured with the high laser-energy density (62 J/mm^3), but with different build orientations (0° and 60°), have a high relative part density: 99.77% and 99.93%, respectively. In contrast, the relative part density of the build condition manufactured with the low laser-energy density (38 J/mm^3) was 93.09%, where LOF porosity comprises a majority of the porosity (6.62%).

EBSD was used to quantify differences in effective grain sizes, grain morphologies, and crystal orientations among the three build conditions. To achieve this, a large area

EBSD map was acquired in three orthogonal planes (with respect to tensile direction) for each build condition. The inverse pole figure (IPF) maps (Figure 3.3) were carefully analyzed so that each orthogonal view shows poles (plane normals in a given grain) rotated in reference to a common direction (the build direction). Figures 3.3a, b, and i show both the direction of hatch filling and the width of the laser passes from the manufacturing process (see dashed arrows in 3.3b). In the 0° and 38 J/mm^3 build condition, EBSD measurements revealed smaller grain structures compared to the 0° and 62 J/mm^3 build condition. Additionally, the hatching is more pronounced in the high laser-energy density (62 J/mm^3) build condition (Figure 3.3b) compared to the low laser-energy density (38 J/mm^3) build condition (Figure 3.3a). Figures 3.3c, g, and h show the melt-pool geometry and microstructure perpendicular to the build direction for all build conditions. In general, a characteristic feature observed in the microstructure for all three build conditions was the grain morphology. Specifically, most grains appeared elongated in a trajectory parallel to the build direction. In the analysis software, texture maps (intensities displayed on inverse pole figures) were computed using a harmonic series expansion and a triclinic sample symmetry (no sample symmetry), as opposed to an orthotropic sample symmetry (like a rolled sheet), so as to not compute erroneous symmetry assumptions. All three build conditions exhibited a similar texture (i.e., the $\langle 001 \rangle$ pole orientations were aligned with the build direction), which is shown in Figure 3.4. However, the maximum intensity of the 0° and 38 J/mm^3 build condition (1.61) was less than the maximum intensities of the other two build conditions (2.01 for the 0° and 62 J/mm^3 build condition and 2.35 for the 60° and 62 J/mm^3 build condition).

Large black regions shown in Figures 3.3a, d and g are areas with a near-zero confidence index and correspond directly with the location of both gas pores and LOF pores (large LOF pores are most prevalent in the 0° and 38 J/mm^3 build condition). The LOF pores were observed in the other two build conditions as well, but to a lesser extent in terms of both size and frequency. A characteristic feature observed around most LOF pores was the presence of small grains. The 0° and 38 J/mm^3 build condition exhibited the smallest effective grain size (width of grains in the direction of tension) of the three build conditions; whereas, the 60° and 62 J/mm^3 build condition had the largest.

In addition to the grain morphology, which was elongated in the build direction, the L-

PBF IN718 microstructure contained a sub-grain structure with apparent growth directions parallel to the building direction (see arrows in Figure 3.5a) and appeared as columnar sub-grains. The sub-grain growth appears cellular in nature (Figure 3.5b) when viewed in a direction parallel to the build direction. The columnar and cellular sub-grain structure are the same structure viewed in different orientations (i.e., a cylindrical structure in three dimensions). The spacing of the sub-grain structure was measured using a method where the number of sub-grain structures was counted per 5 or 10 μm line segments. The number of sub-grains per μm was then converted to a spacing value representing the average spacing between sub-grain structures and compared among the three build conditions. The first, second, and third build conditions showed an average spacing of 0.34, 0.69, and 0.5 μm, respectively. Additionally, the BSE images clearly highlight a distinct melt-pool boundary, shown in Figure 3.5c. Growth of the sub-grains from the melt-pool boundary is well distinguished. Figure 3.6d provides a high magnification view of the sub-grain structure and reveals cells/walls of dislocations, which are decorated with secondary nano-scale precipitates. To determine the elemental composition of those precipitates, EDS line scans were performed at high magnification. Figure 3.6a shows a BSE image from which a line scan was acquired, and Figure 3.6b shows the X-ray intensity corresponding to Fe, Nb, Cr, Mo, and Ni. The secondary precipitates are enriched in Nb and Mo and depleted in Ni, Cr, and Fe. No differences in particle morphologies were observed among the three as-built conditions.

3.3.2 Tensile properties

All measured engineering stress-strain curves are shown in Figure 3.7a, b, and c for the three build conditions. The first build condition (0° and 38 J/mm^3) exhibited the lowest tensile strength and lowest elongation. This build condition had an average yield strength (YS) of 639 MPa $\pm$ 10 MPa, which is approximately 18% lower than the other build conditions. Additionally, the ultimate tensile strength (UTS) of this build condition (774 MPa $\pm$ 22 MPa) was approximately 28% lower than the other two build conditions (1081 MPa $\pm$ 23 MPa and 1070 MPa $\pm$ 34 MPa, respectively). The Young's modulus of the second and third build conditions (0° and 60° oriented parts manufactured with a laser-energy density of 62 J/mm^3) was approximately 195 GPa; whereas, the Young's modulus for the

0° and 38 J/mm^3 build condition was 150 GPa $\pm$ 22 MPa. A summary of the YS, UTS, uniform elongation (UE) and total elongation (TE) is shown in Figure 3.7d and e. The average UE (0.05 ± 0.007) and TE (0.06 ± 0.012) of the 0° and 38 J/mm^3 build orientation were approximately 77% lower than the UE (0.22 ± 0.013 and 0.21 ± 0.034) and TE (0.29 ± 0.027 and 0.28 ± 0.085) of the second and third build conditions. No significant difference was found when comparing the UTS, UE, and TE of the 0° and 62 J/mm^3 and the 60° and 62 J/mm^3 build conditions, but a significant difference in YS was measured between the two. Finally, the YS, UTS, and Young's modulus for the second and third build conditions are comparable to that of wrought IN718 (Table 3.3). The ANOVA results showed that between the first build condition (0° and 38 J/mm^3) and the second build condition (0° and 62 J/mm^3), there were statistically significant differences in YS, UTS, Young's modulus, UE, and TE (all $p < 0.001$). The ANOVA between the first build condition and third build condition (60° and 62 J/mm^3) showed similar differences observed between the first and second build conditions. Additionally, the comparison between the second and third build conditions showed only a statistically significant difference in YS ($p < 0.05$).

3.3.3 Fractography

The fracture surfaces from the 0° and 38 J/mm^3 build condition contained undulating features (Figure 3.8a) due to a high amount of porosity, which is consistent with the high amount of porosity observed in the X-ray CT measurements. Only small pores are visible on the fracture surfaces of the build conditions manufactured with a high laser-energy density (Figure 3.8b and c). The fracture surfaces of all three build conditions have regions of ductile micro-void coalescence (Figure 3.8d) and signs of brittle failure near LOF pores (Figure 3.8e). Sub-grain structures visible in BSE images of the microstructure were also observed in the fracture surfaces (Figure 3.8f).

3.4 Discussion

3.4.1 Effects of laser-energy density

In the first two build conditions, build orientation was the same (0°), but the L-PBF beam settings varied to study the effects of laser-energy density (38 J/mm^3 and 62 J/mm^3) on the three-dimensional pore structure and microstructure. One effect from using the

low laser-energy density (38 J/mm^3) in L-PBF is the formation of a large amount of LOF pores. Results from X-ray CT in Section 3.3.1 show that the specimens manufactured with the low laser-energy density (38 J/mm^3) contained the higher amount of porosity (6.91% of the analyzed volume) compared to the 62 J/mm^3 laser-energy density porosity (0.23% of the analyze volume). Using optical microscopy, Moussaoui et al. [91] showed that the porosity for L-PBF IN718 was approximately 0.8% and 0.48% for 40 J/mm^3 and 61.2 J/mm^3 laser-energy densities, respectively, indicating that for this range of laser-energy density the porosity content decreases as laser-energy density increases (once the laser-energy density is high enough to start forming keyhole pores, the porosity will begin to increase). Fairly similar amounts of porosity were observed for the current work and work from Moussaoui et al. [91] for the laser-energy density near 62 J/mm^3. However, the low laser energy density (i.e., near 38 J/mm^3) showed large differences in porosity (6.91% compared to 0.8%). Although Moussaoui et al. showed different amounts of porosity for the two laser-energy densities, they performed a two-dimensional analysis of the pore structure using optical microscopy (the current study used X-ray CT). Therefore, a direct comparison between the two-dimensional analysis by Moussaoui et al. [91] and the three-dimensional analysis in this work was difficult. It is likely that the 38 J/mm^3 laser-energy density represents a lower bound on sufficient laser-energy density in terms of proper melting parameters. In this work, most of the porosity in the low laser-energy density build condition was characterized as LOF pores, which are formed due to an insufficient melting of the powder particles [23, 106]. Small and spherical pores were also observed in all build conditions, which may originate from hollow powder particles or keyhole collapse [21]. Even though a similar distribution of spherical pore sizes was observed in all build conditions, the 0° and 38 J/mm^3 build condition contained nearly twice the amount of spherical gas pores as the other two build conditions (Table 3.2). The gas pores are typically attributed to the powder characteristics, which should remain constant throughout the different build conditions in this work. However, due to the rough classification method used (i.e., aspect ratio), some LOF pores likely were misclassified as gas pores [107], causing differences in the represented gas porosity values.

The laser-energy density also influenced many aspects of the grain and sub-grain structure. The 38 J/mm^3 laser-energy density specimen contained the smallest effective grain

sizes due to two mechanisms. First, around the LOF pores, a grain refinement was observed, which is consistent with observations by Pei et al. [108] of clustered fine-grain zones around pores. Pei et al. [108] concluded that the pores stopped the grain growth due to disrupting the temperature gradient along the build direction. Second, the melt-pool geometries visible in the microstructure (Figure 3.3) were smaller for the 38 J/mm^3 laser-energy density (compared to the 62 J/mm^3 laser-energy density). Generally, a lower laser-energy density produces less energy input, ultimately reducing the size of the melt-pool [109]. Furthermore, on the plane normal to the build direction, the scan tracks can be observed (Figure 3.3a and b). In both laser-energy densities, the width of the tracks is approximately 100 μm, which can be expected since hatch spacing for both parts was the same (100 μm). However, the scan tracks observed in the 38 J/mm^3 laser-energy density appeared to have a much more irregular pattern (Figure 3.3a) indicative of a high melt-pool instability, which shows a high fluctuation in melt-pool dynamics [110]. A strong texture was observed for both laser-energy densities, such that the majority of ⟨001⟩-oriented grains aligned with the build direction.

Sub-grain structures were observed for both the 38 J/mm^3 and 62 J/mm^3 energy densities. There was an average spacing of 0.34 μm in the 38 J/mm^3 laser-energy density specimens compared to 0.69 μm in the 62 J/mm^3 laser-energy density specimens. The sub-grain structure consists of dislocation sub-structures that form when large amounts of low-energy dislocations cluster [111] to form geometric boundaries that are necessary to accommodate plastic strain [112] exerted by the manufacturing process. Tucho et al. [113] showed that the number of the clustered dislocations is indicative of the amount of plastic deformation created by extreme thermal histories (rapid solidification) in AM processes, meaning a higher number of sub-grain structures, which correlates to a smaller sub-grain spacing, indicates a greater amount of residual stress produced during the manufacturing process. Bertoli et al. [114] showed that lower values of laser power at the same scan speeds (i.e., lower laser-energy densities) had higher cooling rates in L-PBF titanium. The low laser-energy density (38 J/mm^3) specimens in this work showed the smallest spacing, which indicates a higher number of sub-grains, likely experienced higher cooling rates and a higher amount of residual stress as compared to the 62 J/mm^3 laser-energy density specimens.

Although the sub-grain spacing was different between the two laser energy densities, the precipitates that decorated the sub-grain structures were similar in both morphology and composition. Microsegregation of Nb to sub-grain boundaries has been reported for AM IN718 [102, 115] and IN718 Plus [116]. MC type carbides are rich in Nb and Mo [117, 118] and are commonly found in Inconel alloys near irregularly shaped Laves phase particles [119, 120]. While the δ phase is also enriched in Nb and Mo, the δ phase is always characterized by a needle-like morphology [97]. Since none of the observed precipitates had a needle-like morphology (whether on sub-grain boundaries or grain boundaries), it is likely that the precipitates observed in all three as-built conditions are Laves phase mixed with MC type carbides, which was shown to be prevalent in L-PBF IN718 [113, 121, 122].

The difference in laser-energy density produced statistically significant differences in all measured tensile properties (Figure 3.7 and Table 3.3), most likely due to the large amount of LOF pores and differences in thermal history. A comparison between fracture surfaces of specimens produced with different laser-energy densities (Figure 3.8a and b) shows the vast difference in the amount of LOF that contributed to premature failure and a loss of ductility in the low laser-energy density condition. Since the cross-sectional area was measured on the outside of the specimen, the engineering stress was likely underestimated since the 6.91% (volumetric) internal porosity was not accounted for, but this volume-averaged value does not completely account for the nearly 20% difference in strength when comparing the same build orientation. It is likely that the worst case cross-sectional area of porosity (11% in a two-dimensional slice), coupled with the smaller grain size and higher sub-grain density, could account for the differences in tensile properties. However, it is not possible to decouple the effects of the porosity, grain size, and sub-grain density on the mechanical properties due to the dominating effects from the large and numerous LOF pores.

3.4.2 Effects of build orientation given the same laser-energy density

The second and third build conditions have the same laser-energy density (62 J/mm^3) and vary the build orientation: 0° and 60°, respectively. The X-ray CT results showed that the 0° build condition contained 0.23% porosity (by volume), but only 0.07% porosity (by volume) in the 60° build condition was gas porosity (Table 3.2). Although these two

build conditions were manufactured with the same laser-energy density, the laser powers and scan speeds were different (Table 3.1). The build condition at 0° orientation had a faster scan speed (1770 mm/s) than the 60° orientation (1180 mm/s). Aboulkhair et al. [123] showed that in L-PBF aluminum, faster laser scan speeds produce significantly more LOF pores for the same value of laser power. In the current work, there is an increase in laser scan speed and laser power equalling the same laser-energy density. Kamath et al. [25] showed that an increase in laser scan speed had a larger influence on the porosity than laser power because the higher laser scan speed did not provide a sufficient amount of penetrating energy into the powder-bed system to completely melt the powder. This insufficient energy penetration led to a higher amount of porosity. Therefore, the difference in LOF porosity between the two build conditions at the same laser-energy density can be attributed to the different laser scan speeds.

When comparing effective grain sizes of the second and third build conditions (0° and 60°), the third build condition had a larger effective grain size based on line-intercept measurements along the loading direction. Visualizing the gas-recoater and build-recoater planes (see Figure 3.3e and Figure 3.3f) provides insight to explain the slight differences in effective grain size with respect to the loading direction. The average grain widths, measured over a 1 mm x 1 mm area in the gas-recoater plane using a line-intercept method along the loading direction, are 9.4 μm and 13.2 μm for the 0° and 60° build orientations, respectively. Higher magnification views are shown in Figure 3.3b and Figure 3.3c. As shown in this work and previous work (e.g., [68, 94, 95, 99]), the grains in as-built AM microstructures are elongated in the build direction. The specimens built at 60° had grains slightly elongated towards the build direction, causing larger effective grains measured with respect to the loading direction. The crystallographic texture for both of these build conditions was similar, and further analysis of the Schmid factors in each build orientation (with respect to tensile direction) indicated that the averages were approximately the same, indicating that effective grain size was the main difference in microstructure. Differences of sub-grain spacing existed for the two different build orientations (0° and 60°) at the same laser-energy density (62 J/mm^3). The average sub-grain spacing was 0.69 and 0.50 μm for the 0° and 60° specimens, respectively. As previously shown [113], a smaller sub-grain spacing indicates a greater amount of residual stress induced by the

manufacturing process. Therefore, this difference in sub-grain spacing indicates that the amount of residual stress due to the manufacturing process in the 60° specimens was slightly greater than that in the 0° specimens. Deng et al. [124] attributed differences in the amount of residual stress in specimens built at the same laser-energy density to differences in the build orientation of specimens. In the current work, the 60° specimens had less overlap and remelting of previous layers due to the orientation in which they were built. There has also been evidence in the literature showing that the remelting of previous layers can lead to a reduction in accumulated strains, effectively acting as a stress relieving process [125–127]. Therefore, it can be postulated that the increased remelting of previous layers in the 0° specimens decreased the amount of residual stress (compared to the 60° specimens) and ultimately led to a larger sub-grain spacing. Additionally, the precipitates that decorate the sub-grain structures were similar in both morphology and composition for the two build orientations (0° and 60°).

The effects of build orientation on the tensile properties were less drastic than the effects from using a non-optimized laser-energy density. The ANOVA between the two build conditions produced no statistically significant difference in the UTS, UE, TE, and Young's modulus. The minor differences in porosity (attributed to the change in scan speed) did not have a statistically significant effect on the tensile properties. However, there was a statistically significant difference between the yield strengths of the two build orientations but same laser-energy density. The 60° build orientation exhibited a slightly lower yield strength than the 0° build orientation. The smaller effective grain sizes in the 0° build orientation, with respect to the loading direction, would lead to a shorter dislocation mean free path and thus a higher yield strength according to the Hall-Petch effect [128]. Additionally, the standard deviations for the tensile properties were much larger for the 60° build orientation compared to the 0° build orientation. In the 60° build orientation specimens, there was a variation in build height (i.e., specimens taken from the bottom and top grip region); whereas, the specimens from the 0° build orientation were taken from nominally the same build height. Previous research has shown that build height has an effect, albeit sometimes small, on the mechanical properties in L-PBF metals [129–132] due to variations in grain structures.

3.4.3 Relationship to previous work on high-cycle fatigue life

The previous fatigue work by the authors [10] investigated the relationships between AM build conditions, surface roughness, and high-cycle fatigue life for as-built L-PBF IN718. However, no pre-mortem investigation into the material structures was performed. To better understand the full processing-structure-property relationships for as-built L-PBF IN718, this work focused on investigating the microstructure (grain and sub-grain structures) and internal porosity. The relationships among the laser-energy density, build orientation, three-dimensional pore structure, grain structure, sub-grain structure, and quasi-static tensile properties were studied. As previously mentioned, this work used three build conditions that resulted in the extreme cases of fatigue life, while exhibiting variability in the laser-energy density and build orientation.

From the previous work [10], the differences in laser-energy density at the same build orientation showed a large difference in high-cycle fatigue life (10,755 cycles and 60,919 cycles, on average, for the 38 J/mm^3 and 62 J/mm^3 laser-energy densities, respectively, and 0° build orientation). The fatigue work showed that there was no significant difference between surface roughness values, for the aforementioned build conditions, so the difference in fatigue life was mainly attributed to internal porosity differences, which was supported by fractographic analysis of the fatigue failure surfaces. The current work quantified, comprehensively and in three dimensions, the difference in porosity and showed that the porosity had a large effect on the quasi-static tensile properties. The 38 J/mm^3 laser-energy density specimen exhibited roughly 6.91% porosity while also having the lowest quasi-static tensile properties; the findings confirm that the porosity plays a key role in the fatigue life. However, other factors were likely to have influenced the observed differences in fatigue life. Fatigue life can be sensitive to residual stresses, and the current work demonstrates that the differences in sub-grain spacing could indicate a difference in the residual stress caused by differences in the laser processing parameters (i.e., the laser-energy density). In other words, although the internal porosity dominates the observed differences in fatigue life, given the same surface roughness, the differences in residual stress likely had an influence as well. Additionally, when comparing the different build orientations (0° and 60° at 62 J/mm^3 laser-energy density), the previous work showed a significant difference in high-cycle fatigue life (60,919 cycles and 172,497 cycles, on average,

respectively). Results from the fatigue study showed that the difference in fatigue life for the aforementioned build condition was primarily driven by the differences in the surface roughness and identified no differences in porosity. However, the current work showed slight differences in porosity between the two different build orientations. The only significant difference in quasi-static tensile properties between the different build orientations, given the same laser-energy density, was the yield strength. Therefore, the differences in porosity (0.23% and 0.07%, respectively) generally did not influence the quasi-static properties but may have still had an influence on the high-cycle fatigue life since fatigue life has been shown to be sensitive to small changes in porosity, specifically in AM metals [26, 133–135]. Similarly to the observed difference in the sub-grain structure between the different laser-energy densities (but same build orientation), there was also a difference in sub-grain spacing between the two build orientations with a fixed laser-energy density. This indicates a difference in residual stresses causes a difference in the high-cycle fatigue life. The first build condition consisted of the smallest spacing of sub-grain structures resulting from the highest amount of residual stress. The first build condition also correlates with the lowest high-cycle fatigue life among the three build conditions.

3.5 Conclusions

In this study, the influence of the build orientation and laser-energy density on the three-dimensional pore structure, microstructure, and the corresponding quasi-static tensile properties was investigated for as-built L-PBF IN718. Based on the experimental results, the following conclusions are made:

1. The variation of the three-dimensional pore structure was predominantly controlled by the laser-energy density. At the low laser-energy density (38 J/mm^3), the applied energy was insufficient to fully melt the powder, which led to an increase in lack-of-fusion pores compared to the 62 J/mm^3 laser-energy density. The first build condition (0° and 38 J/mm^3) had a 93.09% relative density (6.91% porosity by total volume) compared to 99.77% for the 0° and 62 J/mm^3 build condition. The relative volumetric density for the 60° and 62 J/mm^3 build condition was 99.93%.

2. The grain structure was influenced by both the laser-energy density and the build

orientation. The effective grain size was smaller in the 38 J/mm^3 build condition compared to the 62 J/mm^3. This was due to an observed grain refinement around the lack-of-fusion pores as well as a smaller melt pool geometry. A similar texture was observed for both the 38 and 62 J/mm^3 laser-energy densities (both manufactured at a 0° build orientation). The effective grain sizes, based on a line intercept method used to measure the average grain width in the loading direction, were different between the two build orientations (manufactured with the same laser-energy density) since grains were elongated in the build direction causing a statistically significant difference in the yield strength.

3. Sub-grain structures were observed in the three build conditions that consist of dislocation sub-structures formed when large amounts of low-energy dislocations clustered to form geometric boundaries. A decrease in the spacing of these sub-grains can indicate a higher amount of residual stress caused by higher cooling rates during the manufacturing process. The first build condition (0° and 38 J/mm^3) contained the smallest sub-grain spacing (0.34 μm) and the second build condition (0° and 62 J/mm^3) contained the largest sub-grain spacing (0.69 μm). From the sub-grain spacing, the first build condition likely contains the highest amount of residual stress caused by the L-PBF process, and the second build condition contained the lowest amount.

4. The significant reduction in the yield strength and ultimate tensile strength for the 38 J/mm^3 build condition, as compared to the 62 J/mm^3 build condition, was attributed to the lack-of-fusion porosity. Although the microstructure differences have an effect on the mechanical properties, the individual effects cannot be decoupled due to the dominant influence of the porosity on the properties. The only significant difference in mechanical properties between the 0°- and 60°-oriented specimens was in the yield strength. The effective grain size in the 60° build specimens was slightly larger than in the 0° build specimens, which decreased the yield strength due to the longer mean free path for dislocation motion.

5. In all three build conditions, precipitates were observed at the end of the dislocation walls that are referred to as the sub-grain structures. These precipitates had a high

amount of Nb and Mo, which are consistent with MC type carbides and Laves phase particles. Since all three build conditions were investigated in the as-built (non-heat-treated) condition, no other phases or precipitates were observed.

6. In L-PBF Inconel, the mechanical properties are influenced by the pore structure (which includes both gas porosity and lack-of-fusion porosity), and by the microstructure (which includes the grain size and morphology, the crystallographic texture, the sub-grain structure, and the precipitates/secondary phases). However, in un-optimized laser-energy density builds, the pore structure dominates the mechanical properties. Therefore, to best optimize the mechanical properties for L-PBF IN718, it is recommended to minimize the porosity through laser-energy density control.

Table 3.1. L-PBF IN718 processing parameters for the three build conditions.

Build condition	Laser power (W)	Scan speed (mm/s)	Layer thickness (μm)	Build orientation (°)	Laser-energy density (J/mm^3)
1	168	1475	30	0	38
2	330	1770	30	0	62
3	220	1180	30	60	62

Table 3.2. Porosity values (% by volume for a given part) for each build condition showing the relative density, the gas porosity, and the lack-of-fusion porosity.

Build Condition	Build orientation (°)	Laser-energy density (J/mm^3)	Relative density (%)	Gas porosity (%)	Lack-of-fusion porosity (%)
1	0	38	93.09	0.29	6.62
2	0	62	99.77	0.11	0.12
3	60	62	99.93	0.06	0.01

Table 3.3. The average yield strength, ultimate tensile strength, Young's modulus, uniform elongation, and total elongation of all three build conditions for L-PBF IN718 (with one standard deviation). References are provided for the wrought condition.

Build condition	Build orientation °	Laser-energy density J/mm^3	Yield strength MPa	UTS MPa	Young's modulus GPa	Uniform elongation -	Total elongation -
1	0	38	639 (10)	774 (22)	151 (22)	0.05 (0.007)	0.06 (0.012)
2	0	62	798 (27)	1081 (23)	195 (17)	0.22 (0.013)	0.29 (0.027)
3	60	62	772 (15)	1070 (34)	194 (26)	0.21 (0.034)	0.28 (0.085)
n/a	Wrought		800-1100 [68, 69]	1200-1400 [52]	208 [52]	n/a	0.32 [80]

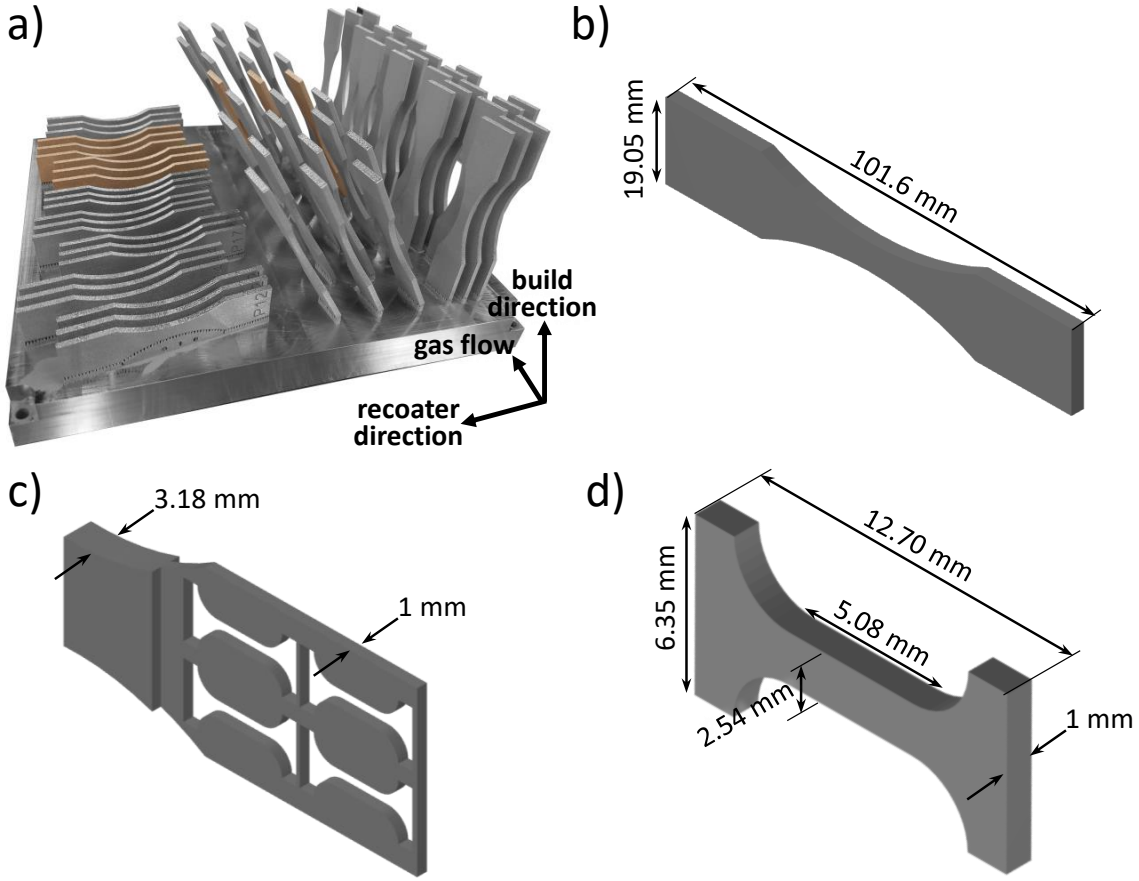

Figure 3.1. Reuse of fatigue specimens from a previous study [10] to perform detailed materials characterization and miniaturized tensile testing in the current study. a) All as-built IN718 fatigue specimens on the build plate prior to removal (from [10]); the nine specimens used in the current study are highlighted (refer to electronic version for color distinction). b) Target dimensions for the fatigue specimens in accordance with ASTM E466-15. c) The thinned grip region of the fatigue specimens, from which the tensile specimens are excised. d) The tensile specimen target dimensions.

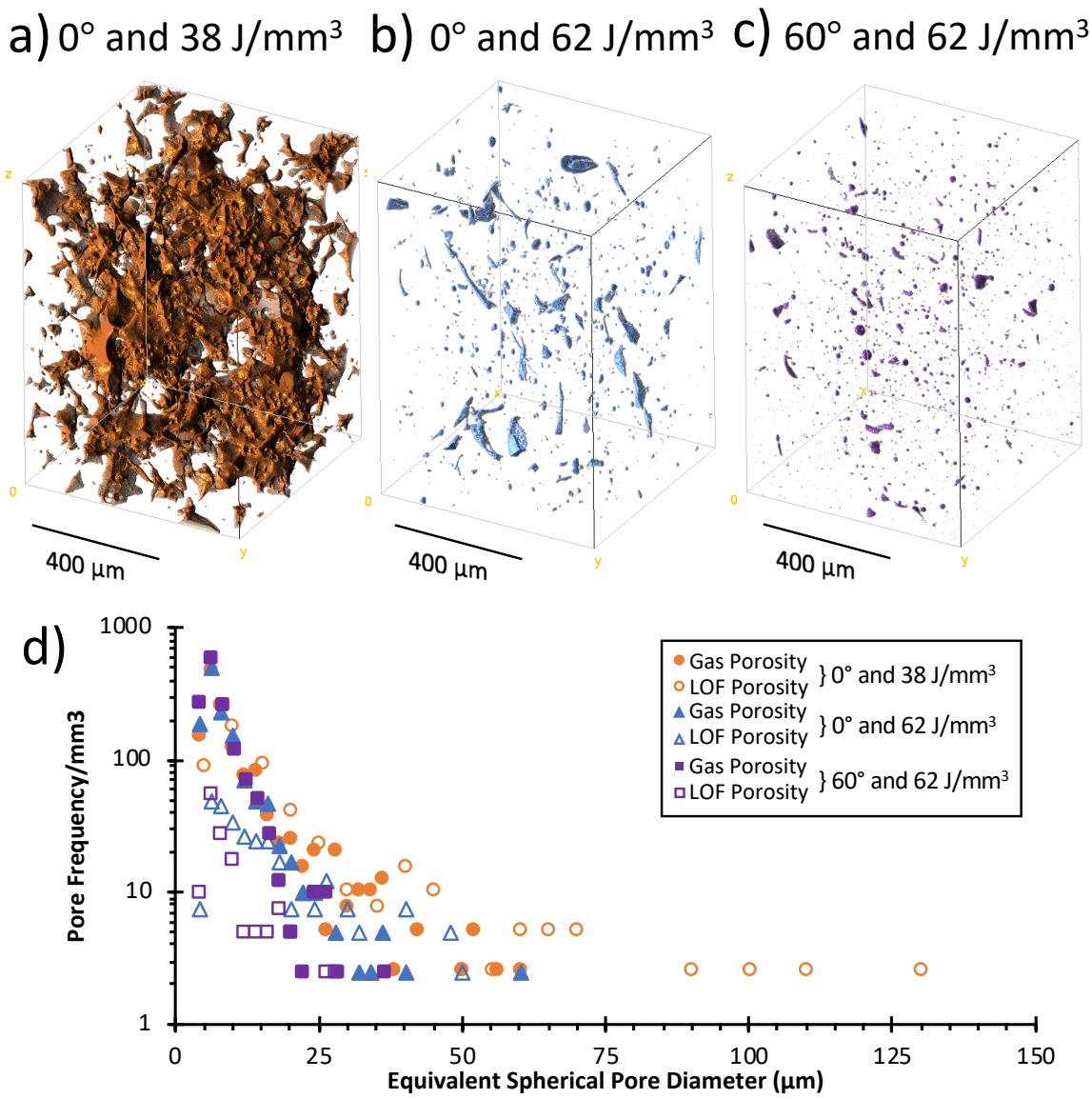

Figure 3.2. X-ray CT reconstruction of porosity (the tensile direction is vertical) for the following build conditions: a) 0° build orientation and 38 J/mm^3 laser-energy density, b) 0° build orientation and 62 J/mm^3 laser-energy density, and c) 60° build orientation and 62 J/mm^3 laser-energy density. d) Frequency of porosity by equivalent spherical pore diameter per build condition showing both gas porosity and lack-of-fusion porosity.

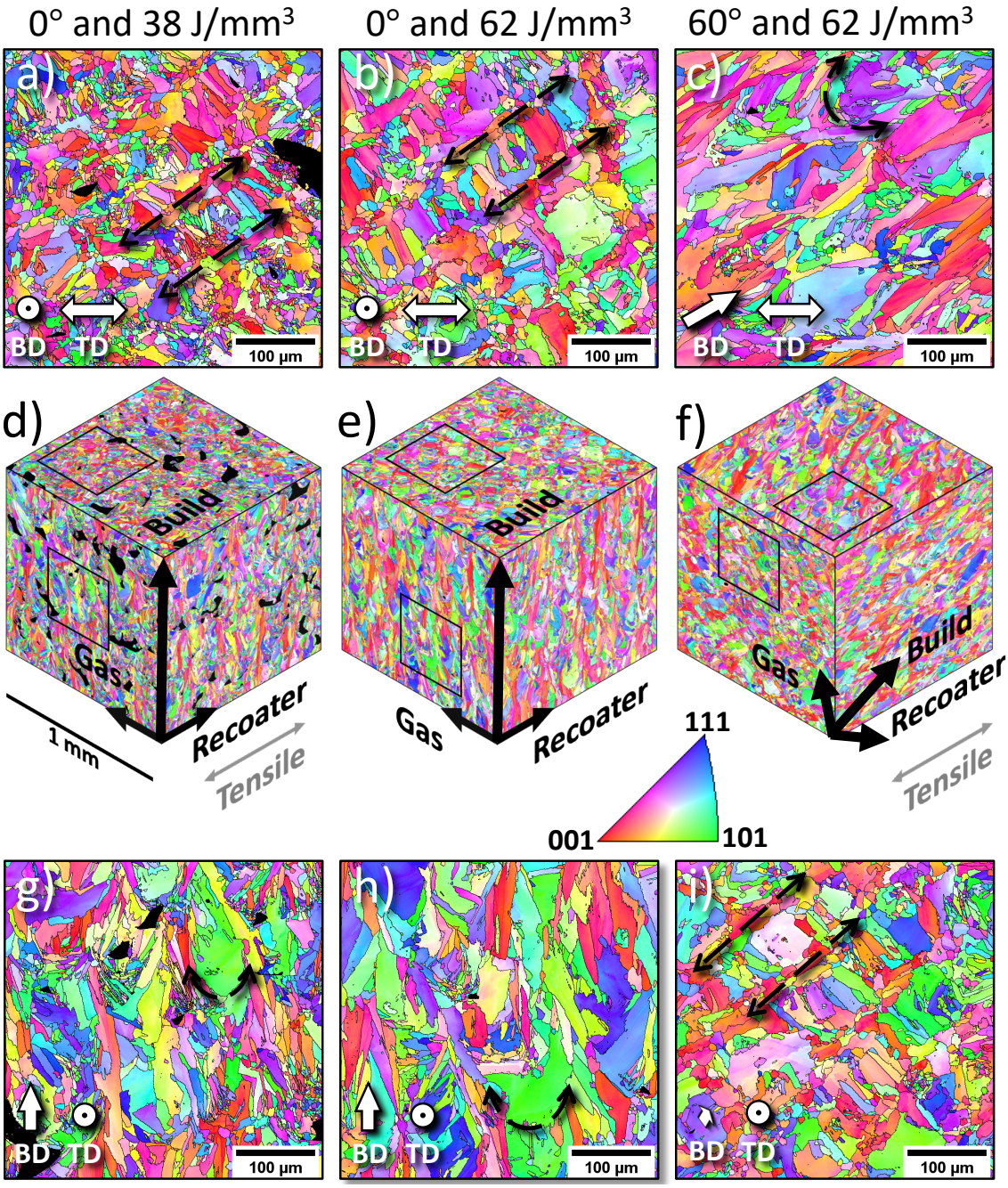

Figure 3.3. EBSD reconstruction of inverse pole figure maps for planes parallel and normal to the tensile direction (TD) for three different build conditions: a,g) 0° and 38 J/mm^3; b,h) 0° and 62 J/mm^3; and c,i) 60° and 62 J/mm^3, where BD stands for build direction. Inverse pole figure maps for all three orthogonal planes shown with respect to gas flow, recoater, build, and tensile directions: d) 0° and 38 J/mm^3, e) 0° and 62 J/mm^3, f) 60° and 62 J/mm^3. All inverse pole figure maps are plotted with respect to the BD.

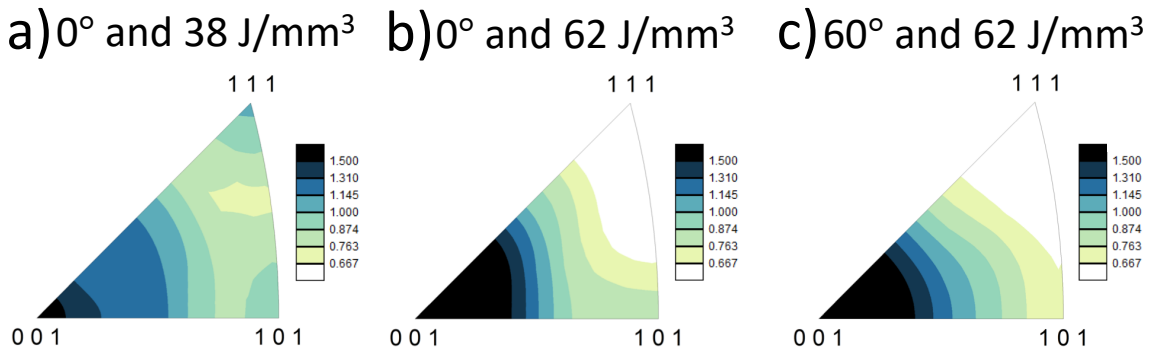

Figure 3.4. The texture heatmaps (harmonic series expansion of grain orientations) for the three different build conditions.

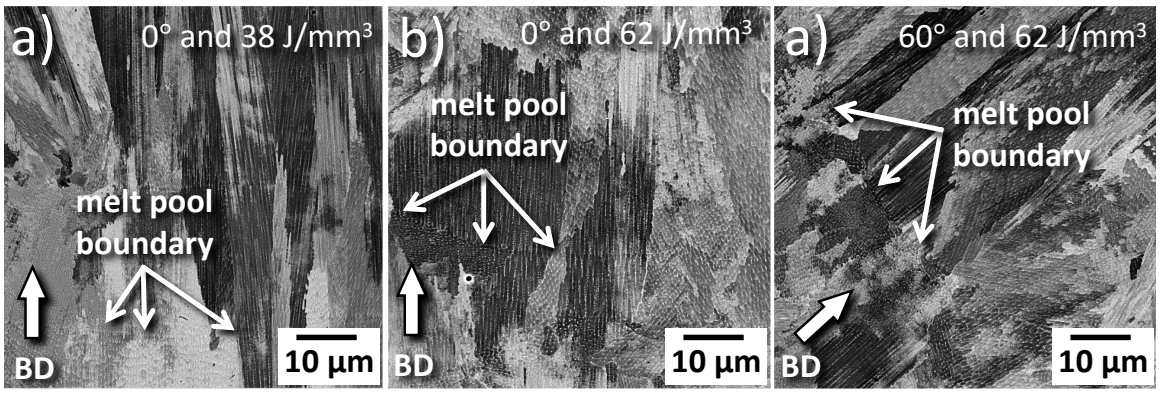

Figure 3.5. BSE images showing the sub-grain structures with apparent growth parallel to the build direction for a) the 0° and 38 J/mm^3 build condition, b) the 0° and 62 J/mm^3 build condition, and c) the 60° and 62 J/mm^3 build condition.

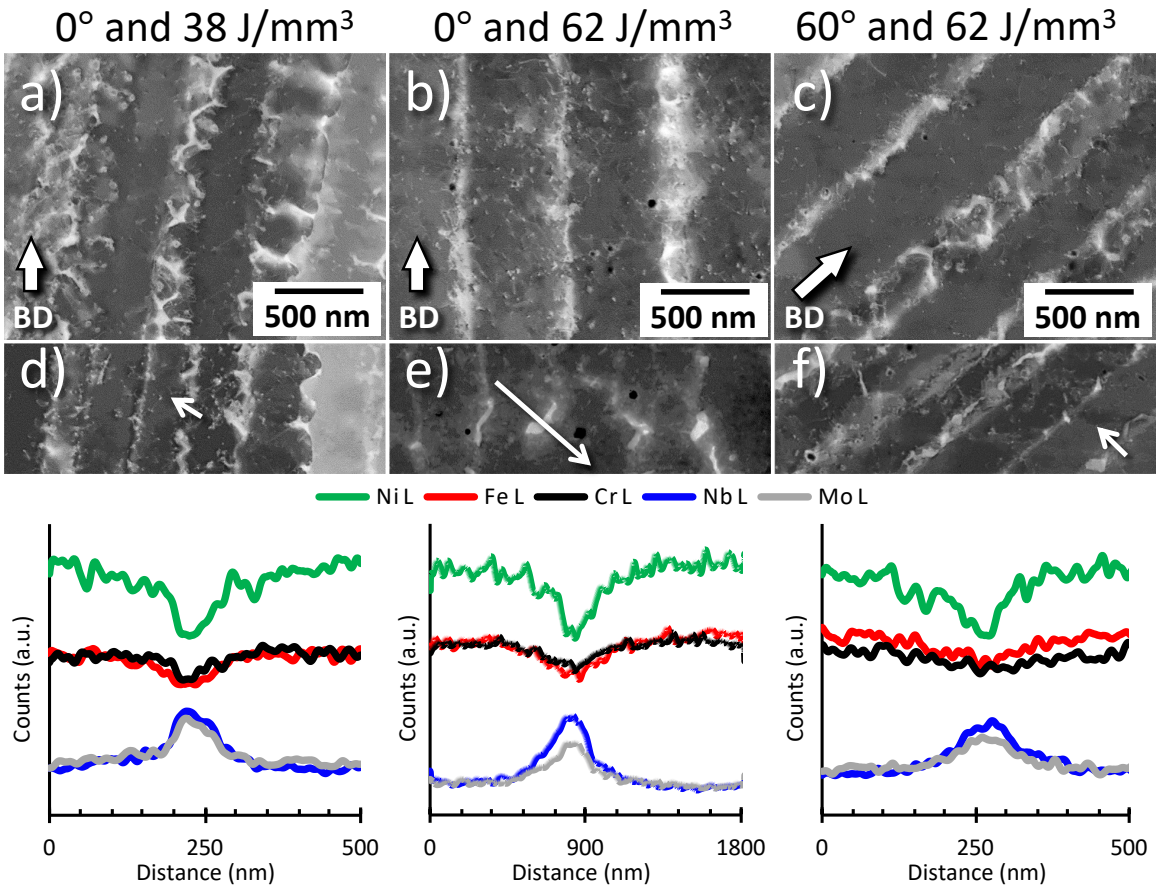

Figure 3.6. BSE images showing the precipitates located on the cellular dislocation structures: a) first build condition (0° and 38 J/mm^3), b) second build condition (0° and 62 J/mm^3), and third build condition (60° and 62 J/mm^3). EDS line scans (elemental counts from L-α lines) of Ni, Fe, Cr, Nb, and Mo, along the direction of the white arrow shown in (d), (e), and (f) for the three build conditions, respectively.

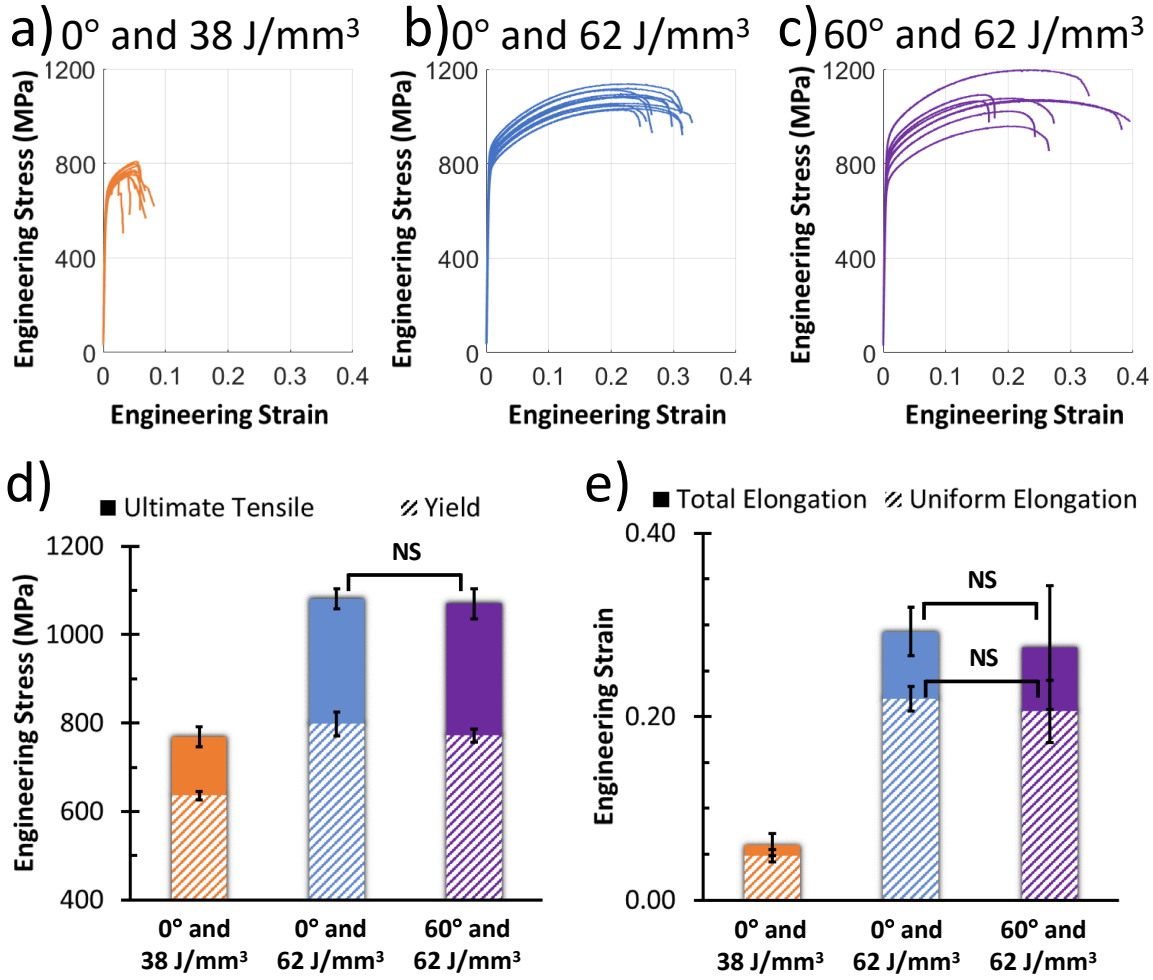

Figure 3.7. Engineering stress-strain curves for a) the first build condition (0° and 38 J/mm^3), b) the second build condition (0° and 62 J/mm^3), and c) the third build condition (60° and 62 J/mm^3). d) Summary of the average yield strength and ultimate strength for the three build conditions. e) Summary of the average uniform and total elongation for the three build conditions. Error bars indicate one standard deviation and NS stands for not significant ($p < .05$).

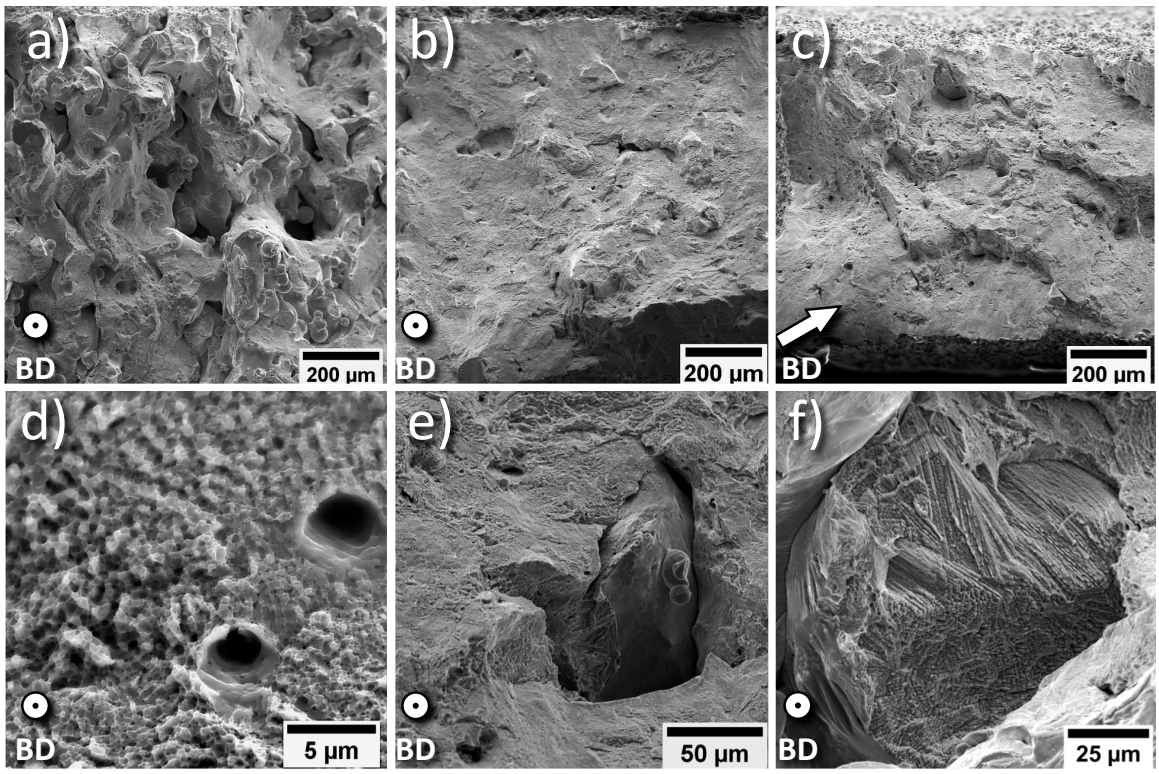

Figure 3.8. Representative SEM images of the fracture surfaces for the following build conditions: a) 0° and 38 J/mm^3, b) 0° and 62 J/mm^3, and c) 60° and 62 J/mm^3. A representative SEM image of d) micro-void coalescence and gas porosity, e) cleavage-like fracture near LOF porosity, and f) the sub-grain structure observed on the fracture surfaces in the rupture zone of the 0° and 62 J/mm^3 build condition.

CHAPTER 4

A MODIFIED VOID DESCRIPTOR FUNCTION TO UNIQUELY CHARACTERIZE THE PORE NETWORKS AND PREDICT FRACTURE LOCATION IN ADDITIVELY MANUFACTURED METALS

As shown in previous chapters, variations in the additive manufacturing (AM) processing parameters can lead to variations in porosity, making it challenging to predict pore-sensitive mechanical response in AM metals. A recently developed pore metric, the void descriptor function (VDF)—which accounts for pore locations, sizes (assuming spherical pores), and distances to the nearest free surface—was shown to improve the predictive capabilities of fracture location in ductile porous metals as compared to predictions based on cross-section area reduction and maximum pore size. This work expands upon the original VDF by incorporating terms to account for non-spherical pore shapes and pore-pore interactions. The modified VDF is then evaluated against 120 computational fracture simulations of laser powder bed fused (L-PBF) 17-4 PH stainless steel tensile specimens and six mesoscale tensile specimens machined from L-PBF IN718. For the simulations, the modified VDF accurately predicts fracture location (within $\pm$5% tolerance) for 5.5% more specimens compared to predictions based on the original VDF and 65.5% more specimens compared to predictions based on the maximum cross-sectional area reduction. In the experimental data set, the modified VDF accurately predicts the location of fracture (within $\pm$5% tolerance) in four out of six specimens compared to two out of six accurate predictions using the original VDF, maximum cross-section area reduction, or largest pore. Furthermore, the maximum VDF shows strong correlations with post-yield mechanical properties, suggesting that it could serve as a promising metric to assist with property predictions in AM metals.

4.1 Introduction

Metal additive manufacturing (AM) has become a popular and vital tool in a variety of different industries [2, 85, 86]. There are many benefits of AM techniques over traditional manufacturing including the ability to achieve high accuracy in fine details, reduced manufacturing time, geometric flexibility, and the ability to use a variety of metals and their alloys [4]. There has been a significant amount of work investigating the relationship among the microstructure and tensile properties in AM metals, which vary widely from under-performing to over-performing when mechanical properties are compared against wrought or cast metals [13, 32–36]. However, recent works have begun to acknowledge the significance that defects in general, and porosity in particular, plays in the mechanical response in AM metals [10, 12–14]. The complexity of porosity can in part be attributed to the different types of pores that exist in AM metals: gas pores, keyhole pores, and lack-of-fusion pores [15]. These different types of pores have variable mechanisms of evolution as well as variability in their respective impact on the mechanical response [20, 23–29]. For example, Hilaire et al. [30] showed that lack-of-fusion pores (irregularly shaped) created localized stress concentrations and promoted the initiation of sharp cracks more significantly than spherical (gas and keyhole) pores. Pores have also been shown to be one of the main drivers in poor fatigue performance in AM metals [10, 26]. Many of these works highlight the importance of understanding the unique evolution of porosity and its corresponding impact on fracture in AM metals.

In ductile metals specifically, one of the most important failure mechanisms is pore coalescence and growth, further highlighting the importance of porosity [11]. Many models have been developed attempting to understand the impact of pores on the mechanical response in metals [136–140]. However, most of these models make many assumptions when predicting the mechanical properties. One important assumption these models make is that pore networks are homogeneous. Since true pore networks are likely inhomogeneous, especially in AM metals, these models are unable to properly predict the mechanical response. However, with the emergence of high-resolution X-ray computed tomography (CT), the measurement of the exact size, shape, and location of individual pores have made modeling the impact of inhomogeneous pore networks on mechanical properties feasible. Recently, an advanced multiscale model method was proposed to capture the impact of

inhomogeneous distributions of pores upon fatigue and fracture behaviour [141]; while it captures pore size, shape, and location exactly using images of pores from CT, the model is computation expensive and requires a highly skilled operator to effective use. To avoid the complexity of directly modeling pores, improved pore metrics have been developed as a way of characterizing complex pore networks and using these metrics to predict the mechanical response [142]. In one example, Du Plessis et al. [143] showed that for cast Ti-6Al-4V tensile specimens, the fracture location could be predicted with high accuracy using the location of the largest measured pore. These new ways of characterizing pore networks and using them to predict the mechanical response are also being used in AM metals. Madison et al. [144] characterized AM specimens using some of these common pore metrics and attempted to correlate them to the mechanical response. They showed that common pore metrics, such as maximum reduction of cross-sectional area, total pore volume, maximum pore volume, and the number of pores, had no strong correlation with the tensile properties. This lack of correlation indicates that either other factors besides porosity play a key role in the fracture of AM metals, or that the current pore metrics inadequately characterize the pore networks at least for the purposes of predicting mechanical response.

One significant advancement to the characterization of pore networks was presented by Erickson et al. [145]. In this work, a new pore metric was derived, aptly named the void descriptor function (VDF), to uniquely characterize pore networks in metals. The VDF metric was derived to account for pore clustering (relative to a location along the gauge length), pore sizes, and pore locations relative to the nearest free surface of the specimen. Erickson et al. [145] then compared the predictive capability of the VDF to commonly used pore metrics to predict fracture location for 120 simulated fracture tests. They were able to show that the maximum value of the VDF accurately predicted fracture (within ± 5 % of the total gauge length) in 91 out of 120 (76.0 %) specimens. In comparison, they showed that the location of the maximum reduction of cross-sectional area was only able to predict the fracture location (± 5 %) in 58 of the 120 (48.0 %) specimens and the location of the largest pore was only able to predict the fracture location (± 5 %) in 59 of the 120 (49.0 %) specimens. Additionally, Erickson et al. [145] showed strong correlations between their maximum VDF value and post-yielding mechanical properties. Although

the VDF derived by Erickson et al. [145] demonstrated significant improvement compared to previous pore-related metrics, the derivation makes certain assumptions that limit the use of the VDF. For example, the VDF does not account for non-spherical pore shapes and pore-pore interactions, which have both been shown to have significant impact on fracture behavior in AM metals [30, 146].

In the presented work, there are two main objectives. The first objective is to extend the formulation of the previously proposed VDF presented by Erickson et al. [145] to include the impact of non-spherical pores and pore-pore interactions. Using the numerical data provided by Erickson et al. [145], the fracture-location prediction capability of the modified VDF is compared to those of the original VDF and common pore-related metrics. The second objective is to experimentally evaluate and assess the modified VDF on a set of IN718 mesoscale tensile specimens manufactured by laser powder bed fusion (L-PBF), thereby extending the test cases beyond the simulated data set presented by Erickson.

4.2 Modification of void descriptor function

Erickson et al. [145] derived the void descriptor function (VDF) to characterize pore networks in ductile metals and potentially serve as an indicator for fracture location and parameter to predict post-yielding mechanical properties. The original VDF derivation by Erickson et al. is inspired by a Laplace radial distribution function used in the work of von Lilienfeld et al. [147] and effectively combines fraction porosity, pore position along the axial direction (clustering), and pore distance to nearest free surface into a single metric, expressed as:

$$\mathrm{VDF}(z_{ref}, P) = \sum_{i=1}^{n} \frac{v_i e^{-\frac{S_i}{\alpha L} - \frac{|c - r_i|}{\rho c}}}{V_{gauge}}, \tag{4.1}$$

where z_{ref} is a given reference point along the axial direction of the specimen (assumed to be the z direction[1]) and P is an array of pore attributes consisting of the individual pore volume (v_i), pore diameter (D_i), and pore centroid (x_i,y_i,z_i) for all n pores in the specimen. The length of the gauge section is L, the total volume of the gauge region is V_{gauge}, and the maximum distance from the centroid of the specimen cross section to the free surface is c (depicted in Figure 4.1b). In Eqn. 4.1, S_i (depicted in Figure 4.1a) represents the distance

[1]The original formulation expresses VDF as a function of x_{ref} because of the assumed alignment of the longitudinal axis with the x direction.

from the reference position, z_{ref}, to the centroid of the i^{th} pore, measured along the axial direction:

$$S_i = \left| z_i - z_{ref} \right|, \tag{4.2}$$

and r_i is the distance from the farthest edge of the pore to the centroid of the specimen cross section, illustrated in Figure 4.1b and calculated as follows:

$$r_i = \sqrt{x_i^2 + y_i^2} + \frac{D_i}{2}. \tag{4.3}$$

In Eqn. 4.1, the term $\frac{S_i}{\alpha L}$ accounts for pore clustering along the axial direction of the gauge section, and α is a weighting parameter that controls the relative influence of a given pore based on its axial position with respect to the point of reference. The term $\frac{|c-r_i|}{\rho c}$ accounts for pore proximity to free surfaces, where ρ is a weighting parameter that controls the relative influence of a given pore based on its position relative to the free surface of the specimen. Erickson et al. [145] performed a Bayesian optimization to find the optimal fitting parameters (α and ρ) for weighing both aspects of the VDF formulation. They found the optimized values for α and ρ to be 0.220 and 0.188, respectively. The reader is referred to Ref. [145] for the complete derivation of the original VDF.

The original VDF formulation by Erickson et al. [145] was evaluated using a finite element (FE) modeling framework. Erickson et al. [145] created 120 FE models of AM 17-4 PH stainless steel uniaxial tensile specimens with statistically similar closed-pore (i.e., pores are isolated and non-overlapping) networks, assuming spherical pores. The number of pores, pore sizes, and pore locations were sampled from distributions based on experimental measurements of AM 17-4 PH stainless steel by Boyce et al. [148]. The pores were explicitly modeled, and an isotropic elastic-plastic constitutive model with von Mises plasticity and material hardening was applied. Failure was simulated using the element deletion method. Details of the pore modeling and simulations can be found in Erickson et al. [145]. Based on the computational fracture simulations, Erickson's VDF metric was shown to outperform common pore-related metrics reported in the literature in terms of its ability to predict fracture location and its correlation with post-yielding mechanical properties.

Despite the promising results from Erickson's original VDF work, there are two limitations in the original formulation that are addressed in this work: lack of pore-pore interactions and assumption of spherically shaped pores. First, although Erickson's VDF formulation does account for pore clustering relative to a given reference point (z_{ref}), it does not account for pore-pore interaction. Figure 4.1c illustrates this limitation by showing two scenarios that would result in equivalent values of VDF despite having obvious differences in the interactions between the two pores P_1 and P_2. For Erickson's VDF formulation, the two cases have the same VDF value because the distance from z_{ref} to P_2 is identical in both cases, and there is no term in Eqn. 4.1 that accounts for the distance between P_1 and P_2. Realistically, the case on the left in Figure 4.1c could be considered more critical than the one on the right due to the interacting stress fields between the two pores, which could impact the fracture behavior (example FE models shown in Appendix B). Yadollahi et al. [146] showed a higher rate of pore coalescence with specimens with closer nearest neighbor pores in AM steels. They attributed this increase in pore coalescence rates to the increased interactions of the pores' stress fields. The incorporation of the weighted nearest neighbors into the modified VDF represents this pore-pore interaction. The second limitation of the original VDF is the assumption that all pores are spherical. It is well documented that pore structures in AM metals can range from spherical to highly non-spherical, depending on the mechanism of void formation [28]. Irregularly shaped (non-spherical) pores generally have more impact on the tensile behavior than do spherical pores depending on their orientation relative to the loading direction [30]. Since Erickson's original VDF formulation assumes every pore is spherical, it does not account for the range of pore morphologies that are observed in AM metals. Thus, this work seeks to extend the VDF to address both of the aforementioned limitations.

4.2.1 Pore-pore interaction

To account for pore-pore interactions in the modified VDF formulation, a nearest-neighbor calculation is performed for each pore (as shown in Figure 4.1d), and the VDF formulation is enriched with a weighted nearest-neighbor distance term, a_i, using the same Laplacian function form that was used in the original derivation:

$$\mathrm{VDF}(z_{ref}, P) = \sum_{i=1}^{n} \frac{v_i e^{-\frac{S_i}{\alpha L} - \frac{|c-r_i|}{\rho c} - a_i}}{V_{gauge}}, \tag{4.4}$$

where

$$a_i = \frac{\sum_{j=1}^{n-1} w_j d_{i,j}}{\gamma}. \tag{4.5}$$

The term a_i accounts for the pore-pore interactions via a weighted nearest-neighbor formulation, with the weights assigned by the term w, which is an array of length $n-1$. In this work, a linear weighting[2] is used such that the array consists of evenly spaced values ranging from 1 to 0, which, for a given pore, will weight the closer pores more than pores farther away. The array of nearest-neighbor distances, d, is arranged closest to farthest and measures the distance between the centroids of the i^{th} and j^{th} pores. Similar to the scaling parameters α and ρ, γ is a scaling parameter for the exponential decay and expresses the relative influence of a given pore on the VDF value in terms of its interactions with all other pores in the specimen. The optimal value of γ was determined using a Bayesian optimization approach [149] similar to that used in Erickson et al. [145] to find the optimal values of α and ρ. The optimal value was determined to be 0.225 and is used for the remainder of this work.

4.2.2 Non-spherical pores

To account for non-spherical pores, and the stress concentrations that they induce, ellipsoids are fitted rather than spheres. Fit parameters for the ellipsoid include the major semi-axis (r_a), the minor semi-axes (r_b, r_c), and the angles θ_{xy}, ϕ_x, and ϕ_y depicted in Figure 4.2a. Because non-spherical pores have been shown to contribute to crack initiation (e.g., [150]), the term in the VDF that describes a given pore's distance to the nearest free surface is scaled by the pore's sphericity, Ψ_i [151]:

$$\Psi_i = \frac{\sqrt[3]{36\pi v_i^2}}{A_i}, \tag{4.6}$$

where A_i is the surface area of the pore. Additionally, the value of r_i from the original derivation is updated to account for non-spherical pore shapes. Referring to Figure 4.2, the updated value, r_i^*, is calculated as:

[2]Various weighting arrays were tested, and it was found that the linear weighting performed the best. More details can be found in Appendix B.

$$r_i^* = \sqrt{\left(x_i + r_a \cos(\theta_{xy}) \cos(\phi_x)\right)^2 + \left(y_i + r_a \cos(\theta_{xy}) \cos(\phi_y)\right)^2}. \tag{4.7}$$

4.2.3 New VDF formulation

The final, modified VDF formulation is given in Eqn. 4.8,

$$\mathrm{VDF}(z_{ref}, P) = \sum_{i=1}^{n} \frac{v_i e^{-\frac{S_i}{aL} - \Psi_i \frac{|c - r_i^*|}{\rho c} - a_i}}{V_{gauge}}. \tag{4.8}$$

An overview of the implementation of the VDF calculation is provided by Algorithm 1. Prior to experimental evaluation using the mesoscale tensile specimens, the modified VDF was assessed by revisiting the computational results from Erickson et al. [145].

4.3 Materials and methods

An experimental evaluation of the modified VDF formulation is carried out using mesoscale tensile specimens machined from the grip sections of AM IN718 fatigue specimens studied previously by Watring et al. [10]. The specimens were fabricated using a 3D Systems[3] ProX DMP 320 machine and IN718 powder. In the previous study [10], 25 unique build conditions were investigated in terms of their impact on total fatigue life. It was found that, of three build orientations considered, the 0° and 60° build orientations resulted in the minimum and maximum fatigue lifetimes, respectively, for a given value of laser-energy density. Furthermore, for a given build orientation, the total fatigue life versus laser-energy density exhibited a bell-shaped curve, with a maximum fatigue life corresponding to a laser-energy density of approximately $62\,\mathrm{J/mm^3}$. Of the 25 build conditions considered previously, the two build conditions representing the best fatigue performance for the 0° and 60° build orientations are selected for the current study. Table 4.1 shows the L-PBF parameters used to fabricate the specimens for the two build conditions. The reader is referred to previous work by Watring et al. [1, 10] for more details about the material.

As illustrated in Figure 4.3, grip regions from the previously investigated fatigue specimens [10] were thinned to approximately 400 µm using wire electrical discharge machining (wire-EDM). From the wafers, mesoscale tensile specimens based on previous work from

[3]Certain commercial software, equipment, instruments or materials are identified in this paper to adequately specify the experimental procedure. Such identification is not intended to imply recommendation or endorsement by the National Institute of Standards and Technology, nor is it intended to imply that the equipment or materials identified are necessarily the best available for the purpose.

Liew et al. [152] and Benzing et al. [153] were excised (dimensions are depicted in Figure 4.3d). Three specimens for each build condition were excised for a total of six specimens. The mesoscale tensile specimens were loaded to failure in uniaxial tension at a strain rate of $1 \times 10^{-3}\,\mathrm{s}^{-1}$, and digital image correlation via an optical microscope was used to measure strain. Guidance from ASTM E3076-18 [103] was used to calculate Young's modulus. Additionally, yield strength, ultimate tensile strength, uniform elongation, and total elongation were calculated according to practices recommended in ASTM E8-16a [104].

Prior to tensile testing, the entire gauge region of each mesoscale specimen was imaged using X-ray CT to enable 3D reconstruction and quantification of the pore structure for each specimen. A Zeiss Xradia Versa 500 X-ray CT machine (operated at 130 kV to 160 kV, 10 W, and approximately 2 µm voxel edge length) was used for the X-ray CT measurements. In the CT, 1601 projection images were collected while rotating the specimen through 360°. Each projection was 1000 pixels × 1000 pixels. Tomographic projections were reconstructed into 3D volume, and then exported as tiff image stacks using the proprietary algorithm provided in the Xradia software provided with the X-ray CT machine. Image processing, segmentation, and format conversion was conducted in a combination of custom Python scripts and FIJI [154]. DREAM.3D [155] was used to quantify the dimensions, orientation, and location of each pore (assuming a best-fit ellipsoid), which were then used to define the pore parameters in the VDF described in section 4.2. Specifically, for each pore, the centroid, volume, surface area, major semi-axis, and orientation of the major semi-axis were recorded. Subsequently, the fraction porosity was measured using the total volume of the pores and the total volume of the specimen observed in the CT data. The sphericity was calculated by Eqn. 4.6. Visual reconstructions of the porosity distribution for each specimen were performed using ParaView [156]. Following tensile testing to failure, the gauge region for each specimen was characterized again using X-ray CT. The post-fracture CT data provides a visual reconstruction of the fractured surfaces and allows for a measurement of the fracture location. Post-failure X-ray CT was conducted at a higher resolution, with voxel edge length of about 1 µm. This was achieved by using "vertical stitching" (a custom mode in the Xradia control software) to extend the vertical dimension as necessary to image the entirety of each half of the fracture gauge section. Images were then down sampled to match the resolution of the initial scans.

4.4 Results

4.4.1 X-Ray CT and porosity values

The X-ray CT measurements were used to quantify the pore structures among the mesoscale specimens. The image stack from each of the CT measurements for each specimen was converted to a VTK file and visualized using Paraview [156]. The CT reconstruction is visualized in Figure 4.4, which shows both the internal porosity and the surface topography of each specimen. Although Figures 4.4a, 4.4b, and 4.4c show three different specimens from the same build condition (P1: 220 W, 1180 mm/s, 60° orientation), there is a slight difference in fraction porosity: 0.04 %, 0.05 %, and 0.01 %, respectively. This also holds true for the second build condition (P2: 330 W, 1770 mm/s, 0° orientation), where the first specimen ($P2_1$) has a fraction porosity of 0.08 % compared to 0.01 % and 0.02 % for the second and third specimens ($P2_2$ and $P2_3$), respectively. The distribution of porosity To determine if the distribution of porosity between specimens are significantly different, a t-test assuming unequal variances was performed between each of the specimens [157], where the t-test . The results from the t-test analysis show that for the first build condition, the mean pore sizes for the three specimens were not significantly different (p values of 0.39, 0.09, and 0.11). For the second build condition, the mean pore sizes are also not significantly different when taking a $p < 0.05$ to be significant (p values of 0.06, 0.34, and 0.05). However, even though the mean pore sizes are not significantly different, the fraction porosity values show that there is a higher amount of porosity in the first specimen for the second build condition.

4.4.2 Stress-strain curves and tensile properties

The measured stress-strain curves for the specimens are shown in Figure 4.5. The nominal cross-sectional area was measured by using a bounding box measurement from the CT image stack. This measurement is comparable to a caliper measurement, which was avoided due to the delicate nature of the specimens. This nominal area was used to calculate the nominal engineering stress. The first specimen from the second build condition ($P2_1$) shows much higher tensile properties compared to the rest of the specimens (Table 4.2). However, the tensile properties are significantly lower for all six specimens compared to the bulk properties obtained using sub-sized tensile specimens in work pre-

viously performed by the authors for the same build condition [1].

4.4.3 Modified VDF results

Prior to the experimental evaluation performed using the mesoscale tensile specimens, a numerical evaluation of the modified VDF formulation was performed using Erickson's data [145]. As reported by Erickson et al. [145], the original VDF formulation was able to accurately predict (within a 5 % tolerance) the fracture location for 91 out of 120 simulated tensile tests using the FE framework. For the same tolerance, the modified VDF formulation presented herein is able to predict fracture location in 96 out of 120 simulated tensile tests, representing a 5.5 % increase in the number of accurately predicted fracture locations compared to the original VDF formulation. By comparing each sample within the population, it is observed that there are six FE simulations for which the modified VDF accurately predicts the fracture location while the original VDF does not (shown in Figure 4.6), and one simulation for which the original VDF accurately predicts the fracture location and the modified VDF does not. This observation is discussed in the following section.

The modified VDF formulation was then experimentally evaluated by predicting fracture location in the six L-PBF IN718 mesoscale tensile specimens. For comparison, the original VDF formulation by Erickson was calculated along with the cross-section area reduction due to porosity along the entire gauge length for each of the six specimens. The plots in Figure 4.7 show the original and modified VDFs and the cross-section area reduction as a percentage. Below each plot are the CT reconstructions of the corresponding specimen in both the undeformed and fractured states, with the pores highlighted in red. For reference, the largest pore by volume in the undeformed state is circled for each specimen. Based on Erickson's original VDF, the location of global maximum coincides with the fracture location in two out of six specimens ($P1_3$ and $P2_1$). Similarly, the location of the maximum cross-section area reduction as well as that of the largest pore coincide with the fracture location in the same two specimens. On the other hand, for the modified VDF presented in this work, the location of global maximum coincides with the fracture location in four out of the six specimens. These results are discussed further in the next section.

4.5 Discussion

4.5.1 Application of the modified VDF to computational fracture simulations: Impact of pore-pore interactions

The performance of the modified VDF is first discussed in the context of the numerical data set investigated by Erickson et al. [145]. Recall that the numerical data set was generated based on pore distributions from experimental-characterization data, which resulted in statistically represented pore distributions. However, the synthetic pore networks were based on the assumption of spherical pores. Since the numerical data set contains pore networks with only spherical pores, any improvement in the modified VDF on the numerical data set is due to the pore-pore interaction (modeled by the weighted nearest neighbor in the modified VDF formulation). As previously discussed, the modified VDF predicts the fracture location correctly in 96 out of 120 simulated tensile tests, whereas the Erickson VDF accurately predicted the fracture location in 91 out of 120 simulated tensile tests. This is approximately 5.5 % more specimens accurately predicted due solely to the pore-pore interaction modification on the VDF. Figure 4.8a shows one of the six simulations for which the modified VDF accurately predicts the fracture location when the Erickson VDF does not. The Erickson VDF predicts that fracture will occur at the large pore at the beginning of the gauge length (shown in the first region in Figure 4.8a). The pore located at the second point in Figure 4.8a is actually slightly larger with an equivalent spherical diameter (ESD) of 99.75 µm compared to an ESD of 96.59 µm for the first pore. However, Erickson's VDF predicts fracture will occur at the first pore due to its relative location to the free surface. Although the Erickson VDF does account for clustering of the pores with relation to a reference point along the gauge length, it does not account for the possible pore-pore interaction. As previously discussed, Yadollahi et al. [146] showed a higher rate of pore coalescence with specimens with closer nearest neighbor pores in AM steels. They attributed this increase in pore coalescence rates to the increased interactions of the pores' stress fields. The incorporation of the weighted nearest neighbors into the modified VDF represents this pore-pore interaction. Specifically, in Figure 4.8a, the location at which the modified VDF predicts fracture to occur consists of the large pore closely surrounded by a large number of smaller pores. This indicates that for this simulation the pore-pore interaction was correctly weighed relative to the size

and the location of the pore to the surface. This holds true for the five other simulations (Figure 4.6) where the weighted nearest neighbor addition to the modified VDF enables the accurate prediction of the fracture location through representation of the pore-pore interaction. However, one example of when the modified VDF incorrectly predicts the fracture location is shown in Figure 4.8b. In this example, the Erickson VDF correctly predicts fracture occurs at the second point, where there are two large pores (ESDs of 79.36 µm and 90.57 µm) that are both located relatively close to the surface. The modified VDF predicts that fracture will occur in this simulation at the first point in Figure 4.8b, where there is one large pore (81.49 µm) surrounded by multiple smaller pores. In this instance, the modified VDF weighs the pore-pore interaction too heavily compared to the size and the location of the pores to the surface. However, six simulations where the modified outperforms the Erickson VDF and only one where it does not is a significant improvement due to the incorporation of the pore-pore interactions.

Similar to the work presented in Erickson et al. [145], a correlation study was performed between the pore metrics and the mechanical properties. To compare how well the modified VDF does against other pore metrics, a Pearson correlation analysis was performed on the numerical data set. Figure 4.9a shows the correlation values between the mechanical properties of the simulated tensile tests and the pore metrics including the modified VDF. The V_{frac} represents the fraction porosity, the N_{tot} is the number of pores, CSA_{ave} is the average cross-sectional area reduction, CSA_{max} is the maximum cross-sectional area reduction, NND_{ave} is the average nearest neighbor distance, ESD_{ave} is the average equivalent spherical diameter, ESD_{max} is the maximum equivalent spherical diameter, and VDF_{max} is the maximum value of the modified VDF. The mechanical properties consist of the elastic modulus (E), the yield strength (σ_Y), the ultimate tensile strength (σ_U), the percent elongation (e_f), and the toughness modulus (U_f). The common pore metrics (i.e., fraction porosity, the number of pores, and cross-sectional area reductions) have the highest correlation to both the elastic modulus and the yield strength. However, the maximum value of the modified VDF has the highest correlation coefficients with the post-yielding mechanical properties (i.e., σ_U, e_f, U_f). This indicates that the modified VDF does a better job at predicting fracture-related properties than other pore metrics. This is evident in the correlation analysis between the actual fracture location and the predicted

fracture location (Figure 4.9b), where the correlation between the predicted fracture location using the maximum VDF location is higher compared to the location of the maximum cross-sectional area reduction and the location of the largest pore. This is consistent with the results of the correlation analysis performed by Erickson et al. [145]. Erickson et al. [145] also determined an ambiguity score to quantify the difference of the global and local VDF maximum values. The higher ambiguity scores indicated the local maximums are similar to the value of the global maximum, which would translate to an ambiguous fracture location. They showed that when removing simulations that had an ambiguity score of more than 0.7, the VDF was able to predict the fracture location more accurately (38 out of 39 specimens). Applying the same ambiguity calculations and threshold to the modified VDF formulation, a total of 40 specimens would have a less than 0.7 ambiguity score. Similar to the Erickson et al. [145] work, the fracture location prediction became slightly more accurate with predicting the fracture in 35 out of the 40 specimens (87.5 %). The correlation between the predicted location and the actual fracture location also increases (Figure 4.9b). A clear visualization of this improvement can be seen in Figure 4.9c, where the actual versus the predicted fracture location for the maximum cross sectional area reduction, location of the maximum pore size, the location of the maximum VDF value, and the location of the maximum VDF value for specimens with less than 0.7 ambiguity score are plotted. It is clear that removing the more ambiguous specimens, some of the outliers (in Figure 4.9c) are removed. Comparing the modified VDF to the Erickson VDF, approximately the same number of specimens fall within the ambiguity score threshold (40 and 39, respectively). The modified VDF, however, predicted fewer specimens when removing specimens with an ambiguity score higher than 0.7 despite predicting more prior to the ambiguity score thresholding. Some specimens that were accurately predicted with the modified VDF were removed during this thresholding. This would indicate that although the modified VDF generally performs better than the Erickson VDF, the ambiguity is increased from adding the pore-pore interaction. Figure 4.6e shows a clear example of how this takes place. When the pore-pore interaction is included in the VDF formulation, the VDF value for the area (around 0.4 mm) with a high number of pores increases. The modified VDF accurately predicts the fracture to occur at this location when the Erickson VDF does not, but also increases the ambiguity of this prediction resulting

in this being one of the specimens that would be removed when applying an ambiguity score threshold. The modified VDF shows a slight predictive improvement compared to the Erickson VDF. However, when comparing to the current pore metrics used to predict fracture location, the modified VDF performs exceptionally well. Recall the location of the maximum cross-sectional area reduction and the location of the largest pore accurately predicted 58 out of the 120 specimens (48 %) and 59 out of the 120 specimens (49 %), respectively. The modified VDF accurately predicted 65.5 % more specimens than the location of the maximum cross-sectional area reduction and 62.7 % more specimens than the location of the largest pore. This shows significant improvement over the commonly used pore metrics to predict fracture location and demonstrates the VDF is a promising metric to predict failure properties in AM metals.

4.5.2 Application of the modified VDF to experimental data: Impact of pore-pore interactions and pore ellipticity

As mentioned above, the modified VDF was evaluated using the six mesoscale tensile specimens. The pore structure for the mesoscale tensile specimens differ from the simulated tensile specimens in the work from Erickson et al. [145]. The porosity shown in each of the specimens in Figure 4.4 has irregular shaped pores. The modified VDF incorporates both the pore-pore interaction and the pore ellipticity into the formulation. As previously discussed, the numerical data set from Erickson et al. [145] consisted of only spherical pores making it impossible to determine the impact of fitting ellipsoids to the pores. However, there is literature showing that the shape of pores impacts the tensile properties and fracture locations. Hilaire et al. [30] showed that lack-of-fusion pores (irregularly shaped) created localized stress concentrations and promoted the initiation of sharp cracks, whereas the more spherical (gas pores) did not initiate fracture under tensile loading. The work from Hilaire et al. [30] would indicate that under tensile loading, irregular shaped pores contribute to fracture more than spherical pores. Therefore, it is important to determine the impact of the ellipsoid fitting in the VDF formulation. In the mesoscale tensile specimens, both pore-pore interactions and the ellipsoid fitting will impact the prediction of the fracture location. The modified VDF is able to accurately predict fracture location for four out of six specimens (66.6 %) compared to two out of six specimens (33.3 %) for the Erickson VDF (shown in Figure 4.7).

To decouple the impact of the pore-pore interactions and the ellipsoid fitting for the mesoscale specimens, the modified VDF was split into a VDF containing only the pore-pore interaction and the ellipsoid fitting and re-evaluated on the six mesoscale specimens. The VDF including just the pore-pore interaction term predicts the fracture location two out of the six specimens (33.3 %). The pore-pore interaction changes the predicted fracture location in two of the specimens compared to the Erickson VDF. When looking at the maximum VDF with just the ellipsoid fitting term, the predicted fracture location changes in two of the six specimens compared to the Erickson VDF, which are different specimens than those predicted for the pore-pore impact. However, the maximum VDF including just the ellipsoid fitting coincides with fracture location in three of the six specimens (50.0 %). Depending on the specimen, the pores will have different impacts on the modified VDF. A clear example of this is in the first mesoscale specimen for build condition P1. The VDF formulation is decomposed to demonstrate the relative impact from the pore-pore interaction and the ellipsoid fitting (shown in Figure 4.10). Figure 4.10a shows the Erickson VDF plotted against the partially modified VDF containing the pore-pore interaction term. There is a clear indication at the first highlighted location that this clustering of pores increases the VDF value due to the pore-pore interaction. Although including the pore-pore interaction increases the VDF value at the fracture location, the global maximum would still predict fracture to occur at the same location as that predicted by the Erickson VDF. Figure 4.10b shows the impact of the ellipsoid fitting (sans pore-pore interaction). In the first highlighted section of Figure 4.10b, there is an irregularly shaped pore that is relatively small in size. In the Erickson VDF, this pore does not increase the VDF value due to its small size. However, in the partially modified VDF that includes the ellipsoid fitting term, a small local maximum appears at this pore's location. This shows that the modified VDF value increases at pore locations that are more irregular in shape, which reflects research showing that such irregular pores increase localized stress concentrations and hence influence fracture behavior. The next highlighted section in Figure 4.10b shows the region discussed in Figure 4.10a. This clustering of pores has one pore that is large and irregularly shaped. The irregular shape of this pore increases the VDF value at its corresponding location. However, the predicted fracture location (i.e., location of global maximum) remains the same. The highlighted section in Figure 4.10c shows the combined

effect of the pore-pore interaction and the ellipticity terms. In this highlighted section, the non-spherical pore shape together with pore-pore interaction drive the VDF value to exhibit a global maximum, which correctly predicts the fracture location. This example shows the breakdown of how each additional parameter in the modified VDF influences the VDF values.

Similar to the computational work, the modified VDF was compared to the location of the maximum reduction in cross-sectional area and the location of the largest pore for the experimental data set. The location of the maximum pore size and the location of the maximum cross-sectional area reduction accurately predicted fracture location in two out of the six specimens (which were the same as those accurately predicted by the Erickson VDF), as compared to the four fracture locations accurately predicted by the modified VDF. Additionally, there are no cases for which any of the other metrics correctly predict fracture location and the modified VDF does not.

There are two specimens for which none of the metrics considered (including the modified VDF) accurately predicts the fracture location: $P1_2$ and $P2_3$. Examining closely the CT data for $P1_2$ (Figures 4.7b and 4.4b), there are no obvious features in the region where fracture occurred that would indicate that fracture was driven by porosity or surface roughness. Thus, it is postulated that fracture could have been driven by features in the grain or sub-grain structures. However, further investigation is required to confirm this. Examining the VDF plot for specimen $P2_3$ (Figure4.7f), it is noted that there is a near-plateau region of high VDF values within which fracture occurred. Thus, although fracture did not occur precisely at the point of the VDF global maximum, it did occur within the elevated plateau region. This example demonstrates the potential ambiguity in selecting a single point of fracture and shows that, in some cases, it might be appropriate to use the VDF function to evaluate potential regions, rather than points, of failure. In summary, although the original Erickson VDF does not outperform the common pore metrics for predicting fracture in the experimental tensile specimens, the predictive capability of the VDF is improved significantly once the pore-pore interaction and the pore ellipticity are included.

4.5.3 Limitations and future work

Although this work shows significant improvement to the predictive capabilities of the VDF, there are still limitations to the work that should be addressed. This work focused on improving the predictive capabilities of the VDF to account for pore shape, specifically ellipticity, and pore-pore interaction. Similar to the limitations addressed in Erickson et al. [145], this work neglects the effects of surface roughness. However, surface roughness is known to play a critical role in the mechanical response of AM metals, especially fatigue life [10, 81–83, 158]. The mesoscale specimens presented in this work were excised via wire-EDM, which was assumed to remove any significant surface roughness imparted by the L-PBF process. However, there could still be local surface roughness features that may have affected the tensile properties. For applications in which the as-built surface remains intact, the surface roughness would depend on geometry, processing parameters, and build orientation, which could have a significant impact on the mechanical behavior. Thus, future work should incorporate effects of surface roughness into the VDF formulation. Another current limitation of the modified VDF formulation is that both the Erickson VDF and the modified VDF presented in this work assume a one-dimensional problem using uniaxial tensile testing (i.e., VDF is expressed as a function of position along the loading axis). Additionally, AM metals have been shown to exhibit anisotropic mechanical behavior with respect to build orientation [159]. In the future, the VDF formulation could be extended to account for multi-axial loading, anisotropic behavior, and failure predictions for more complex, three-dimensional geometries.

Although there are still limitations to the general application of the VDF to complex AM parts, the modified VDF shows significant improvement over common pore metrics in predicting the fracture location and correlating with the mechanical properties. Significant improvement is made upon the current pore metrics by including the pore-pore interaction, pore size, pore shape, pore clustering, and the location of pores relative to the free surface of the specimen.

4.6 Conclusion

In this study, the void descriptor function (VDF) developed by Erickson et al. [145] was modified and improved via incorporation of pore-pore interactions and pore shapes

(as measured by ellipticity). The numerical data set from the work by Erickson et al. [145] that simulated the uniaxial tensile testing of porous AM metals was first used to compare the modified VDF to Erickson's original VDF and other common pore metrics. After analyzing the modified VDF using this numerical data set, six mesoscale IN718 specimens manufactured by laser powder bed fusion were used to experimentally evaluate the modified VDF. Based on the results from the application of the modified VDF on both the numerical data set and the mesoscale specimens, the following conclusions are made:

1. The incorporation of the pore-pore interaction (using weighted nearest neighbors) accurately predicted the fracture location ($\pm 5\,\%$) for approximately 5.5 % more specimens than the Erickson VDF. The modified VDF accurately predicted 96 out of 120 specimens, whereas the Erickson VDF predicted 91 out of 120 specimens. Although the modified VDF showed only a slight improvement compared to the Erickson VDF, the VDF in general shows significant improvement over common pore metrics. The modified VDF accurately predicted fracture in 65.5 % more specimens than the maximum cross section reduction and 62.7 % more specimens than the maximum pore size.

2. The improvement of the modified VDF due to the ellipsoid fitting is more complex to quantify. However, the modified VDF, combining both the pore-pore interaction and the pore ellipticity, accurately predicted fracture location in four out of six specimens in the experimental evaluation compared to two out of six for the original VDF, the maximum reduction in cross-sectional area, and the location of the largest pore by volume. This is the first time the VDF has been experimentally evaluated, and it shows improved predictive capability for fracture locations in the experimental dataset relative to previously reported pore metrics.

3. The maximum value of the modified VDF exhibits a strong correlation with post-yield mechanical properties compared to the correlation between mechanical properties and commonly reported pore metrics, including fraction porosity, the number of pores, maximum pore size, average pore size, and maximum cross-sectional area reduction for the numerical data set. This result suggests that the VDF could be a

promising metric to assist with characterizing pore networks and predicting ductile-metal failure properties, including for AM metals.

4. The promising results from the assessment of the modified VDF against both the numerical data set and the experimental, mesoscale specimens shows that pore-pore interaction and pore shape play a vital roles in the fracture behavior in porous AM metals. The development of metrics that account for interactions between different mechanisms driving failure in AM metals is vital for the incorporation of AM metals into critical applications.

Algorithm 1: Modified VDF formulation

For each z_{ref} in L
  For pore i from 1 to n, where n is the total number of pores
    Step 1: Calculate effect of pore-pore interactions, a_i
      For j=1 to n-1
        Generate linearly spaced weight vector w_j from 1 to 0
        Generate nearest-neighbor distance vector $d_{i,j}$
      Calculate $a_i = \frac{\sum_{j=1}^{n-1} w_j d_{i,j}}{\gamma}$
    Step 2: Calculate effect of pore clustering along gauge length, S_i
      Calculate $S_i = \left| z_i - z_{ref} \right|$
    Step 3: Calculate effect of pore distance to free surface, $|c - r_i^*|$
      Calculate fitted ellipsoid parameters
        Major semi-axis of the ellipsoid: r_a
        Ellipsoid angles from major semi-axis: θ_{xy}, ϕ_x, and ϕ_y
      Calculate distance from centroid to edge of pore, r_i^*
      Calculate $|c - r_i^*|$
    Step 4: Calculate VDF contribution for pore i
  Sum VDF values for all pores according to Eqn. 4.4

Table 4.1. L-PBF IN718 processing parameters for the two build conditions.

Build condition	**Laser power (W)**	**Scan speed (mm/s)**	**Layer thickness (μm)**	**Build orientation (°)**	**Laser-energy density (J/mm^3)**
P1	220	1180	30	60	62
P2	330	1770	30	0	62

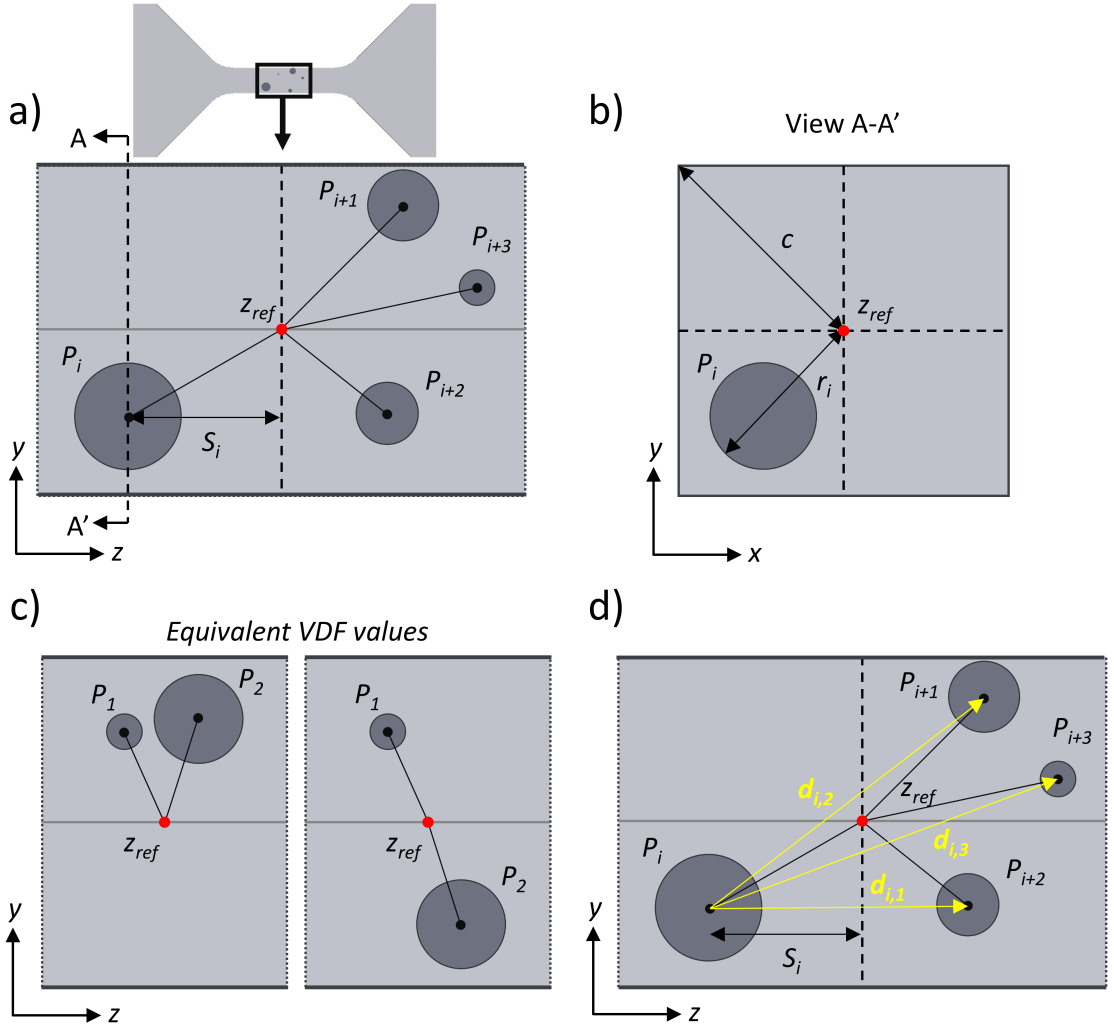

Figure 4.1. Magnified view of specimen gauge section illustrating parameters used in the original and modified VDF formulations, where the z axis is aligned with the longitudinal axis of the tensile specimen. a) Magnified view along the gauge length, adapted from Ref. [145]. b) View of the gauge cross section, adapted from Ref. [145]. c) Limitation of the original VDF, where two instances have the same VDF value despite having different interactions between P_1 and P_2. d) Proposed improvement to original VDF by incorporating pore-pore interactions using the parameter $d_{i,j}$.

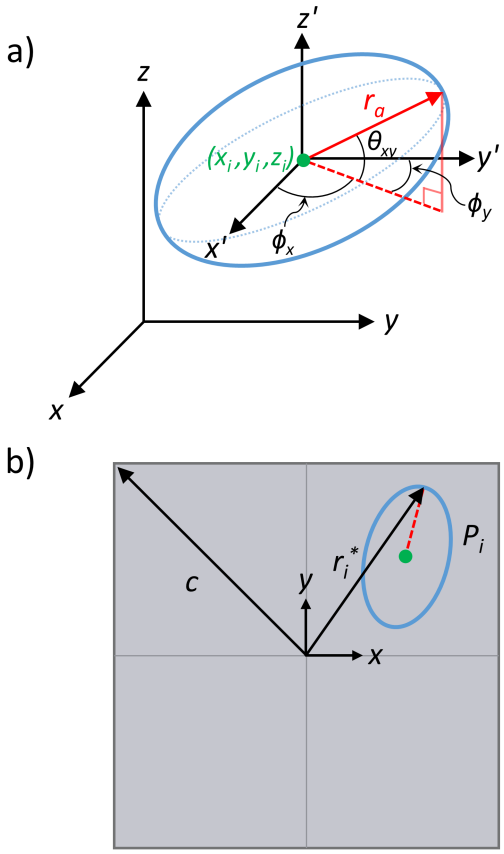

Figure 4.2. Ellipsoidal representation of pore P_i. a) Best-fit ellipsoid showing the major semi-axis (r_a), the angle between vector $\vec{r}_a$ and the projection of $\vec{r}_a$ in the xy plane (θ_{xy}), the angles between the projection of $\vec{r}_a$ and the x axis (ϕ_x) and the projection of $\vec{r}_a$ and the y axis (ϕ_y), and the centroid of the ellipsoid (x_i, y_i, z_i). b) The projected ellipsoid in the xy plane and the definition of r_i^* and c used in the VDF formulation.

Table 4.2. Mechanical properties for six L-PBF IN718 mesoscale specimens and bulk properties from previous work [1]. Build condition P1: 220 W, 1180 mm/s, 60° orientation orientation. Build condition P2: 330 W, 1770 mm/s, 0° orientation.

Specimen	Yield strength (MPa)	Ultimate tensile strength (MPa)	Uniform elongation -	Total elongation -
$P1_1$	290	416	0.0573	0.0758
$P1_2$	552	668	0.0784	0.0957
$P1_3$	326	503	0.1070	0.1497
$P1_{bulk}$ [1]	772	1070	0.2100	0.2800
$P2_1$	555	768	0.1175	0.1343
$P2_2$	541	759	0.1664	0.1868
$P2_3$	372	598	0.1847	0.2001
$P2_{bulk}$ [1]	798	1081	0.2200	0.2900

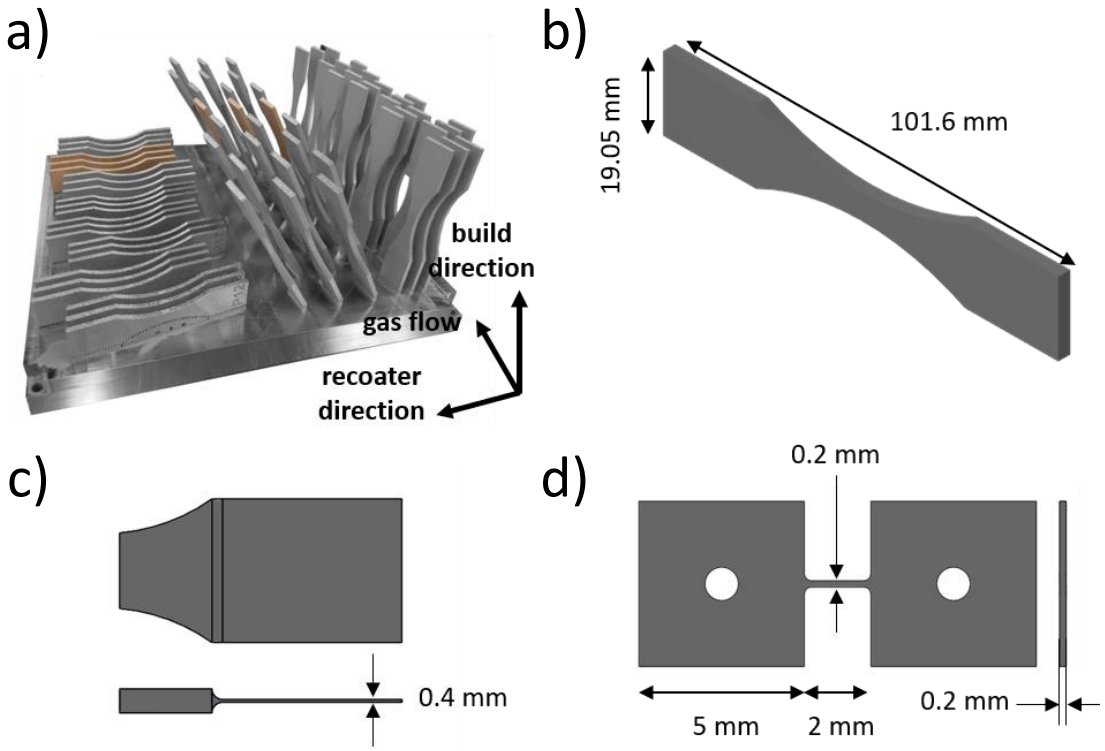

Figure 4.3. Reuse of fatigue specimens from a previous study [10]. a) All as-built IN718 fatigue specimens on the build plate prior to removal; the six specimens used in the current study are highlighted (refer to electronic version for color distinction). b) Target dimensions for the fatigue specimens in accordance with ASTM E466-15. c) Thinned grip region of the fatigue specimens, from which the mesoscale specimens are excised. d) Nominal dimensions of mesoscale tensile specimens.

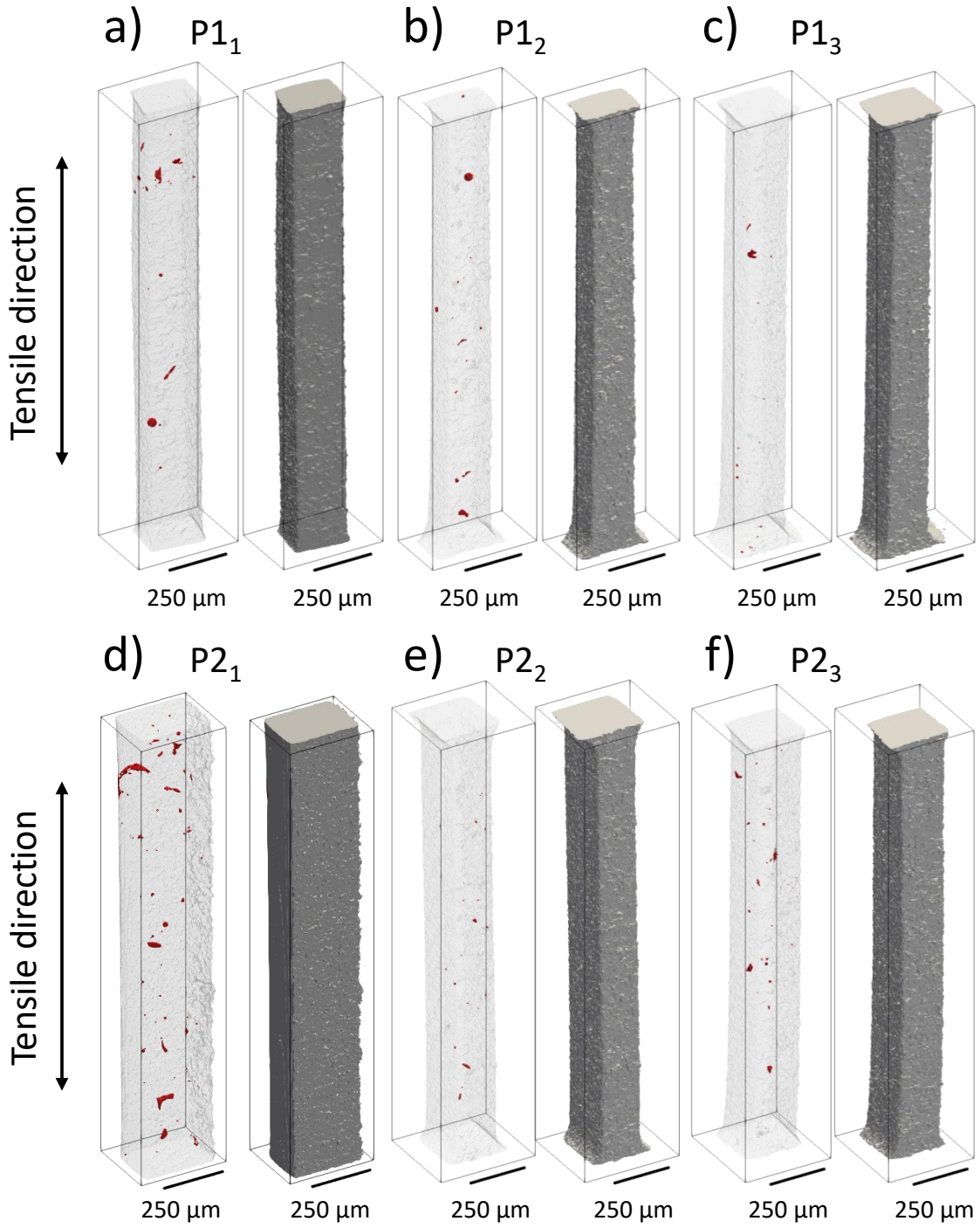

Figure 4.4. X-ray CT reconstructions of L-PBF IN718 mesoscale specimens showing internal pore structures highlighted in red. a-c) Three specimens manufactured using build condition P1 (220 W, 1180 mm/s, 60° orientation). d-f) Three specimens manufactured using build condition P2 (330 W, 1770 mm/s, 0° orientation). Specimens were excised from larger samples using precision wire-EDM on all surfaces.

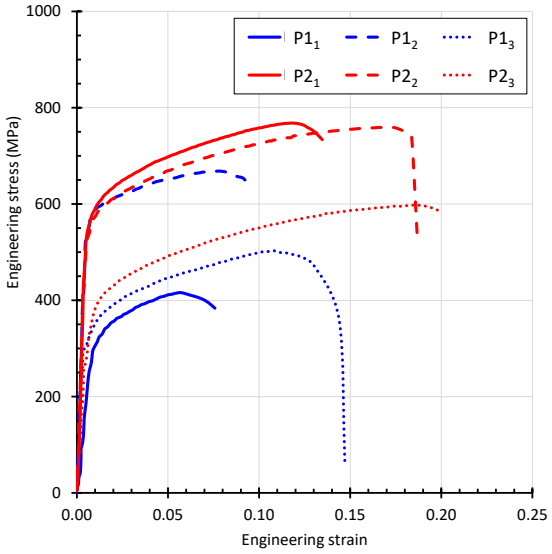

Figure 4.5. Engineering stress-strain curves for six L-PBF IN718 mesoscale specimens (three repeats for two different build conditions).

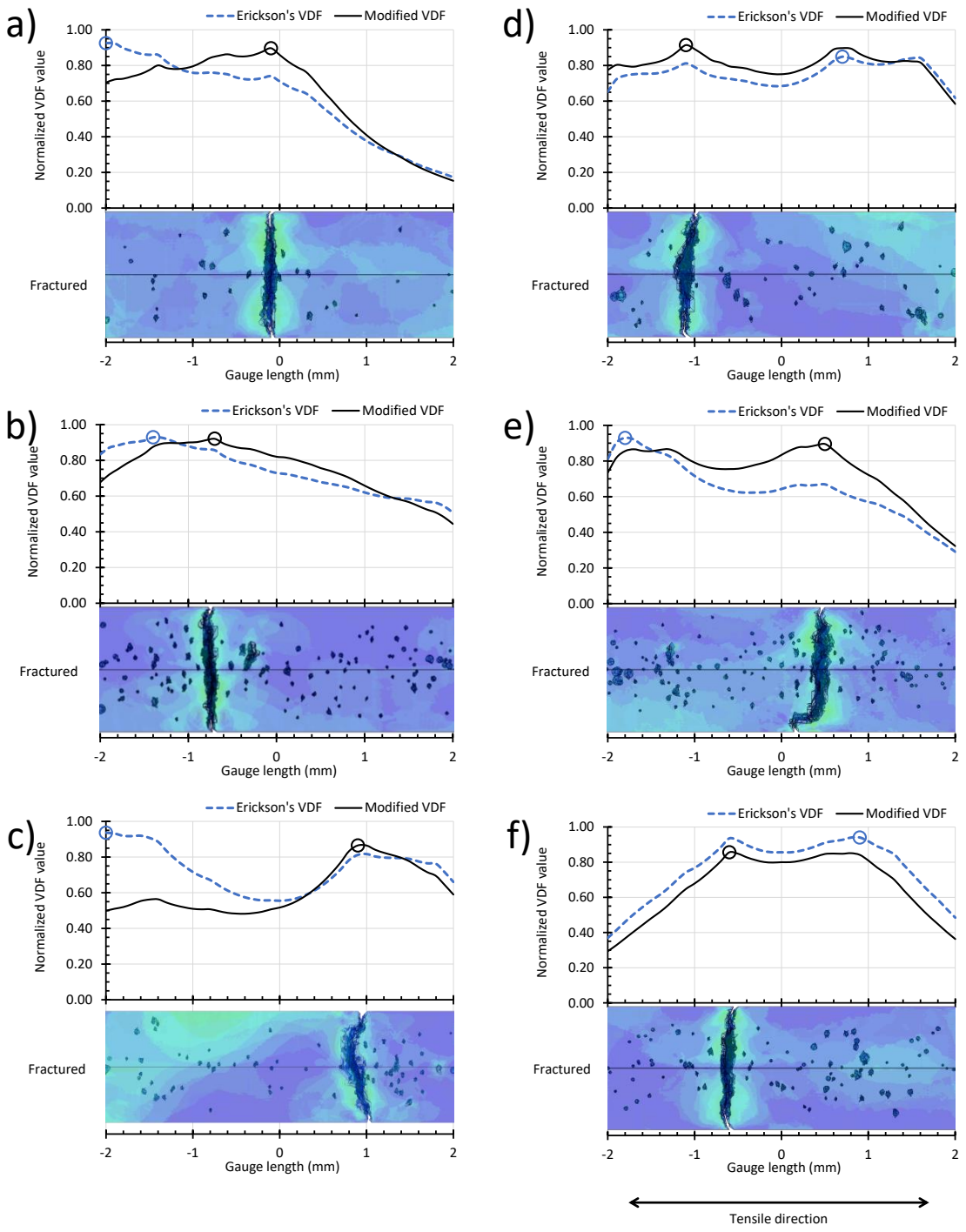

Figure 4.6. The six simulations (a - f) for which the modified VDF formulation correctly predicts the fracture location and the Erickson VDF formulation does not. The predicted fracture location for both the Erickson VDF and the modified VDF are circled.

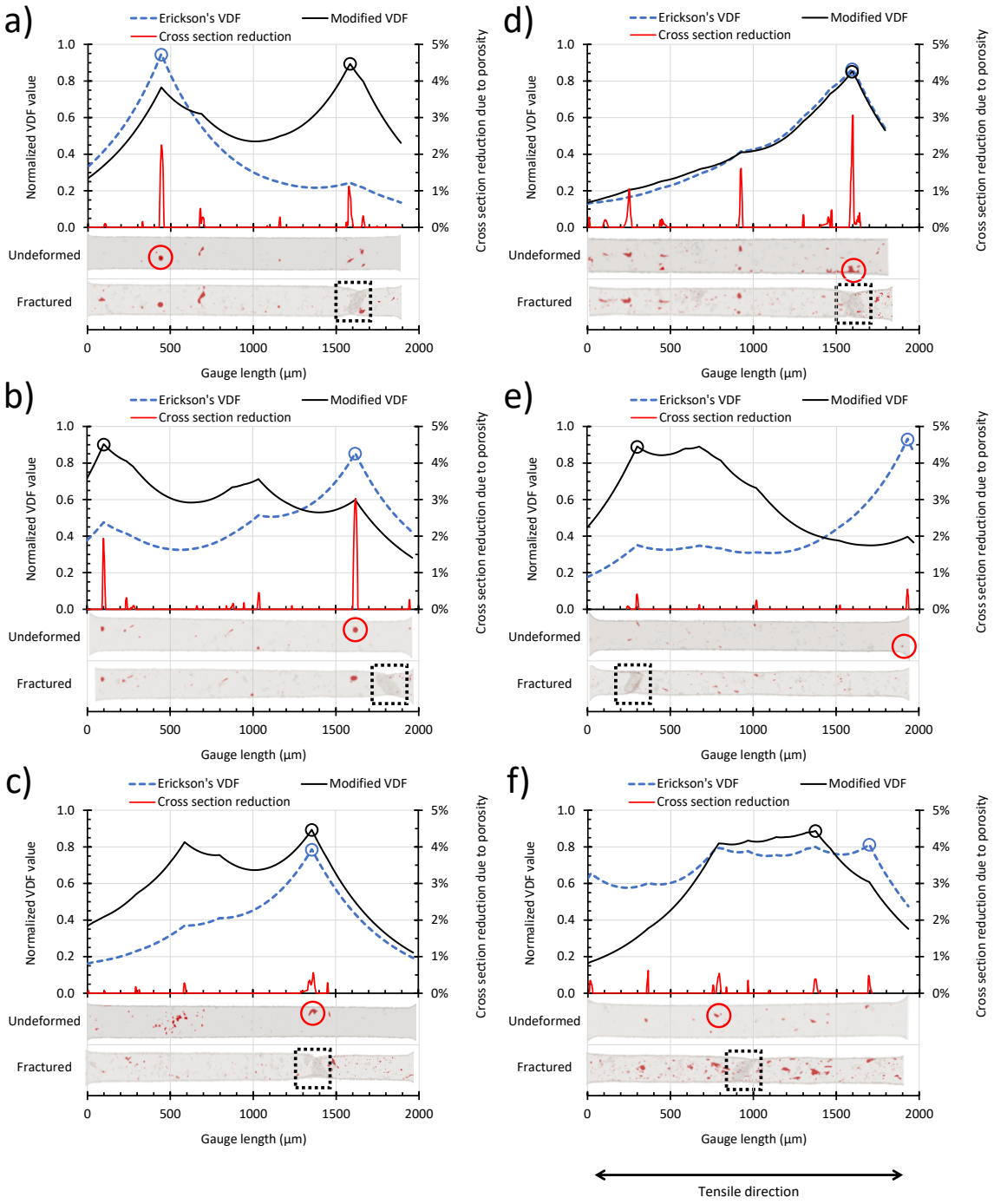

Figure 4.7. Erickson's VDF and modified VDF predictions of fracture locations, where the maximum value for each VDF is circled, for build condition P1 (220 W, 1180 mm/s, 60° orientation) specimens a) $P1_1$, b) $P1_2$, and c) $P1_3$, and for build condition P2 (330 W, 1770 mm/s, 0° orientation) specimens d) $P2_1$, e) $P2_2$, and f) $P2_3$. For each specimen, the cross-section reduction due to porosity is plotted in red and the location of the largest pore by volume is circled in red.

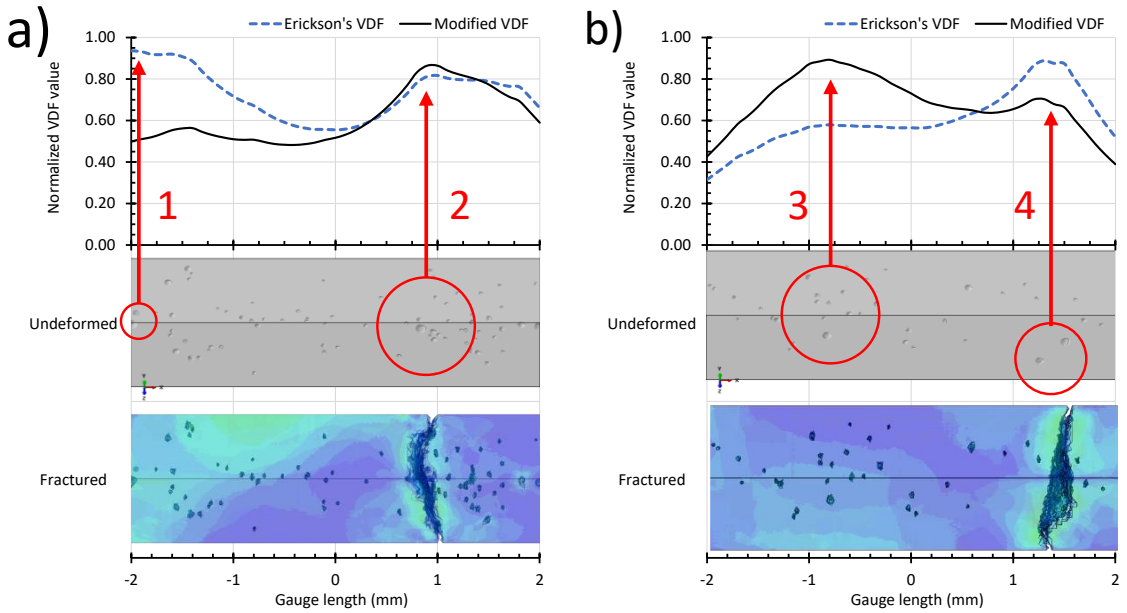

Figure 4.8. Important features in the computational fracture simulations for a) a simulation for which the modified VDF accurately predicted the fracture location and the Erickson VDF did not, and b) a simulation for which the Erickson VDF accurately predicted fracture location and the modified VDF did not.

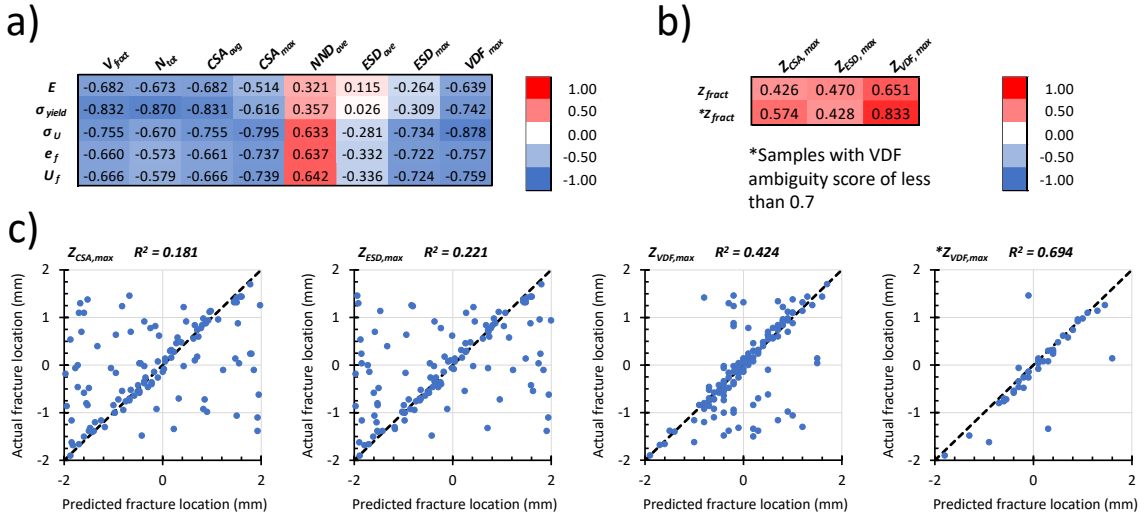

Figure 4.9. Correlation studies showing a) Pearson correlation coefficients between pore metrics and mechanical properties including the modified VDF. b) The Pearson correlation coefficients between the actual fracture location and the predicted fracture locations for the maximum cross-sectional area reduction, the maximum equivalent spherical diameter, the Erickson VDF, and the modified VDF. c) Scatter plots showing the Pearson correlation between the actual fracture locations and the predicted fracture locations.

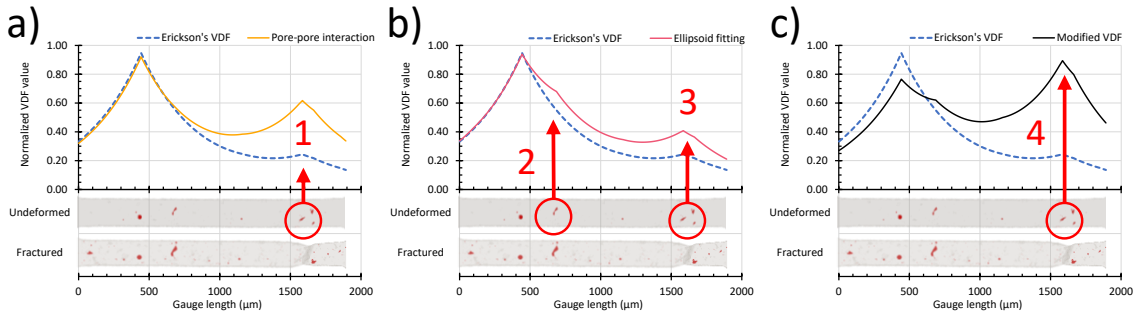

Figure 4.10. Important features in one mesoscale specimen that influence the VDF formulation for a) the pore-pore interaction, b) the ellipsoid fitting, and c) the final, modified VDF formulation.

CHAPTER 5

SUMMARY, CONCLUSIONS, AND FUTURE RECOMMENDATIONS

This dissertation provides an investigation into the processing-structure-property relationships for laser powder bed fused Inconel 718 using materials characterization and mechanical testing across multiple length scales. Within the dissertation, three main topics were investigated. The objective of the first study was to examine the relationships among the AM process parameters, surface roughness parameters, and the high-cycle fatigue life for as-built laser powder bed fused Inconel 718. The objective of the second study was to relate the pore structure, microstructure, and quasi-static tensile properties to various processing conditions for laser powder bed fused Inconel 718. The last study sought to improve upon a void descriptor function to characterize pore structures in additively manufactured metals and to use mesoscale tensile specimens to experimentally validate the modified function.

The work presented in the first study was one of the first works to investigate the as-built condition of L-PBF Inconel 718 for a large number of parameter sets in the context of fatigue. The findings showed that there are two competing mechanisms controlling the fatigue life in as-built L-PBF Inconel 718: surface roughness and porosity. Furthermore, the results showed that both the surface roughness and porosity can be controlled by the processing parameters, and non-optimal build parameters caused a significant increase in surface and sub-surface crack initiation sites leading to a reduction in fatigue life. It was found that surface roughness is mainly associated with the build orientation and porosity is mainly associated with laser-energy density.

Although the first study concluded that the porosity was crucial in governing the fatigue life in as-built AM Inconel 718, there was no quantification of the influence of the processing parameters on the variability of the three-dimensional pore structure and

microstructure and their corresponding impact on tensile properties. Therefore, the second study focused on quantifying the three-dimensional pore structure, microstructure, and quasi-static tensile properties. This work confirmed that the variation of the pore structure was predominantly controlled by the laser-energy density and found that for L-PBF Inconel 718, there exists a range of laser-energy density for which the relative density is optimized. Additionally, one of the salient findings from this work was that unique sub-grain structures and intragranular misorientations develop during the AM process. This was one of the first publications to report on these sub-grain features in L-PBF Inconel, as many of these sub-grain structures are completely erased during post processing.

Finally, the last study presented work on deriving a modified void descriptor function and experimentally validating its predictive capability for fracture location using mesoscale L-PBF Inconel 718 specimens. This work improved on a previously derived void descriptor function to include pore-pore interaction and pore ellipticity in addition to pore size, pore clustering, and location of pores relative to the free surface, all expressed in a single metric. The modified VDF shows significant improvement over common pore metrics in predictive capabilities, which indicates that it is a promising metric to assist with characterizing pore networks and predicting ductile-metal failure properties. The development of metrics that account for interactions between different mechanisms driving failure in AM metals is vital for the incorporation of AM metals into critical applications.

In terms of future work, it is recommended to further investigate and model the evolution of the observed sub-grain structures and intragranular misorientations and their respective impact on mechanical behavior. Such work on sub-grain structures would benefit research in Ni-based, Fe-based, and high entropy alloys, which are alloys in which sub-grain structures have been observed. Specifically, the evolution of the sub-grain structures and intragranular misorientations as a function of the AM processing parameters and their effects on the mechanical properties should be quantified, which will expand the use of as-built AM components in critical applications. Another suggestions for future work is to expand the void descriptor function. As discussed in Chapter 4, the void descriptor function shows significant improvements over common pore metrics for predicting fracture location and fracture-related mechanical properties. Although this is a significant improvement, the void descriptor function still has a few limitations. Surface roughness is

known to play a critical role in the mechanical response of AM metals, especially in fatigue life. In the current state, the void descriptor function assumes the surface roughness does not impact fracture. Therefore, the author recommends future work expanding the scope of the void descriptor function to incorporate the impact of surface roughness on fracture. Additionally, the void descriptor function currently assumes a one-dimensional problem using uniaxial tensile testing. Expanding the void descriptor function to use a more generalized stress state will allow for the void descriptor function to be used to predict fracture in more complex loading scenarios and more complex geometries.

APPENDIX A

SURFACE ROUGHNESS PARAMETERS AND CORRELATION COEFFICIENTS

Topography parameters considered in this work include the asperity-peak density (η), the asperity-peak radius (ρ), and the standard deviation of asperity-peak heights (σ_s). The spectral moment approach, developed by McCool et al. [160], was used to calculate the surface topography parameters. In this method, the topography parameters are calculated from the spectral moments m_0, m_2, and m_4. However, this method accounts for a single, arbitrary cross section of the surface and can lead to significant variation of the calculated parameters depending on the cross section taken. A better approach to calculating the topography parameters, suggested by Pawar et al. [161], is to average the spectral moments from all cross sections and then calculate the topography parameters from the averaged spectral moments. Additionally, the spectral moments can be affected by the finite difference discretization technique used. To be consistent with literature [162], the central finite difference discretization was used. The equations for calculating all of the surface roughness and topography parameters are presented below.

Surface roughness parameters:

$$R_a = \frac{1}{nm} \sum_{i=1}^{n} \sum_{j=1}^{m} Z_{ij} \tag{A.1}$$

$$R_{ms}(R_q) = \sqrt{\frac{1}{n} \frac{1}{m} \sum_{i=1}^{n} \sum_{j=1}^{m} Z_{ij}^2} \tag{A.2}$$

$$R_t = \max_{ij} Z_{ij} - \min_{ij} Z_{ij} \tag{A.3}$$

$$R_{sk} = \frac{1}{mnR_q^3} \sum_{i=1}^{n} \sum_{j=1}^{m} Z_{ij}^3 \tag{A.4}$$

$$R_{ku} = \frac{1}{mnR_q^4} \sum_{i=1}^{n} \sum_{j=1}^{m} Z_{ij}^4 \tag{A.5}$$

Table A.1. Complete list of roughness and topography parameters investigated.

Description	Parameter
Roughness Average	Ra
Root Mean Squared	Rms (Rq)
Max Height of Profile	Rt
Skewness	Rsk
Kurtosis	Rku
Average Distance - Peak to Valley	RzDIN
Average Distance - Peak to Valley (Japanese Standard)	RzJIS
Asperity-Peak Density	η
Asperity-Peak Radius	ρ
Standard Deviation of Asperity-Peak Heights	σ_s

$$R_{zDIN} = \frac{1}{s}\sum_{i=1}^{s} R_{t_i} \tag{A.6}$$

$$R_{zJIS} = \frac{1}{5}\sum_{i=1}^{5} R_{t_i} \tag{A.7}$$

$$\eta = \frac{\frac{m_4}{m_2}}{6\pi\sqrt{3}} \tag{A.8}$$

$$\rho = 0.375\sqrt{\frac{\pi}{m_4}} \tag{A.9}$$

$$\sigma_s = \sqrt{1 - \frac{0.8968}{\alpha}}\sqrt{m_0} \tag{A.10}$$

$$m_0 = AVG(Z^2) \tag{A.11}$$

$$m_2 = AVG((\frac{dZ}{dx})^2) \tag{A.12}$$

$$m_4 = AVG((\frac{d^2Z}{dx^2})^2) \tag{A.13}$$

$$\alpha = \frac{m_0 m_4}{m_2^2} \tag{A.14}$$

Once all of the surface roughness and topography parameters were calculated, a correlation study was performed to determine the roughness parameters exhibiting the highest correlation to the high-cycle fatigue life. Three different correlation coefficients were investigated: the Pearson correlation, the distance correlation, and the Spearman correlation. The Pearson correlation coefficient measures the linear correlation between two

variables (Figure A.1) [163]. The Spearman correlation measures the monotonic relationship between two variables, which can be linear or nonlinear (Figure A.2) [164]. Finally, the distance correlation measures both the linear and nonlinear relationship between two variables with one coefficient (Figure A.3) [165]. The surface roughness was averaged for all of the scans for each of the sides. The four parameters that were selected according to the correlation study were the roughness average (Ra), the max height of profile (Rt), the average distance peak to valley (RzDIN), and the standard deviation of asperity-peak heights (σ_s).

Pearson correlation coefficients:

$$r_{xy} = \frac{\sum_{i=1}^{n}(x_i - \overline{x})((y_i - \overline{y})}{\sqrt{\sum_{i=1}^{n}(x_i - \overline{x})^2}\sqrt{\sum_{i=1}^{n}(y_i - \overline{y})^2}} \tag{A.15}$$

Spearman correlation coefficients:

$$r_s = 1 - \frac{6\sum d_i^2}{n(n^2 - 1)} \tag{A.16}$$

$d_i = rg(X_i) - rg(Y_i)$, is the difference between ranks

Distance correlation coefficients:

$$dCor(X, Y) = \frac{dCov(X, Y)}{\sqrt{dVar(X)dVar(Y)}} \tag{A.17}$$

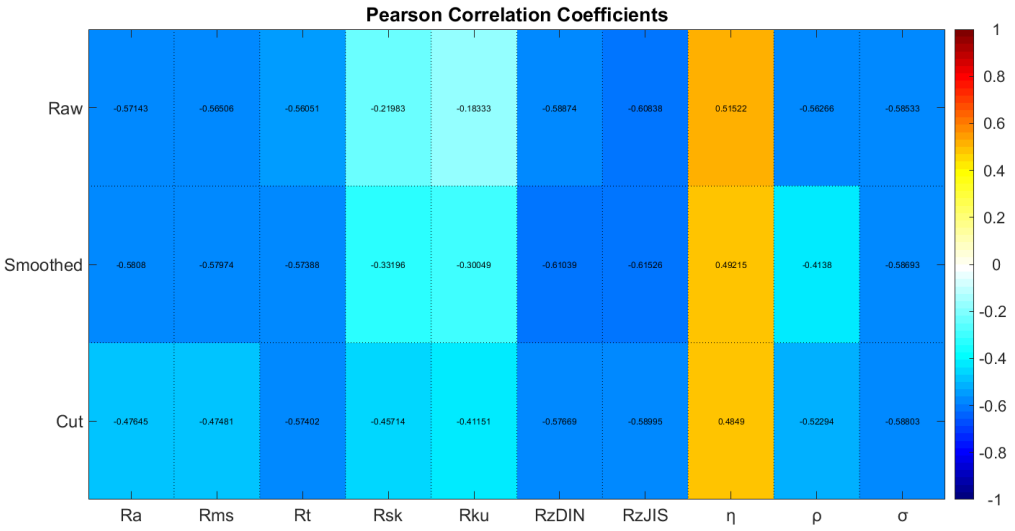

Figure A.1. Pearson correlation coefficient among surface roughness values and high-cycle fatigue life.

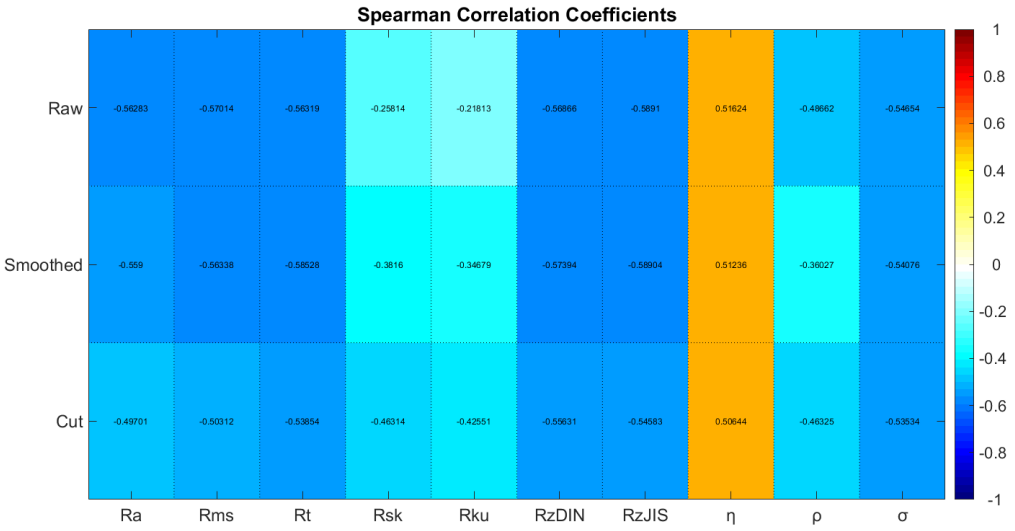

Figure A.2. Spearman correlation coefficient among surface roughness values and high–cycle fatigue life.

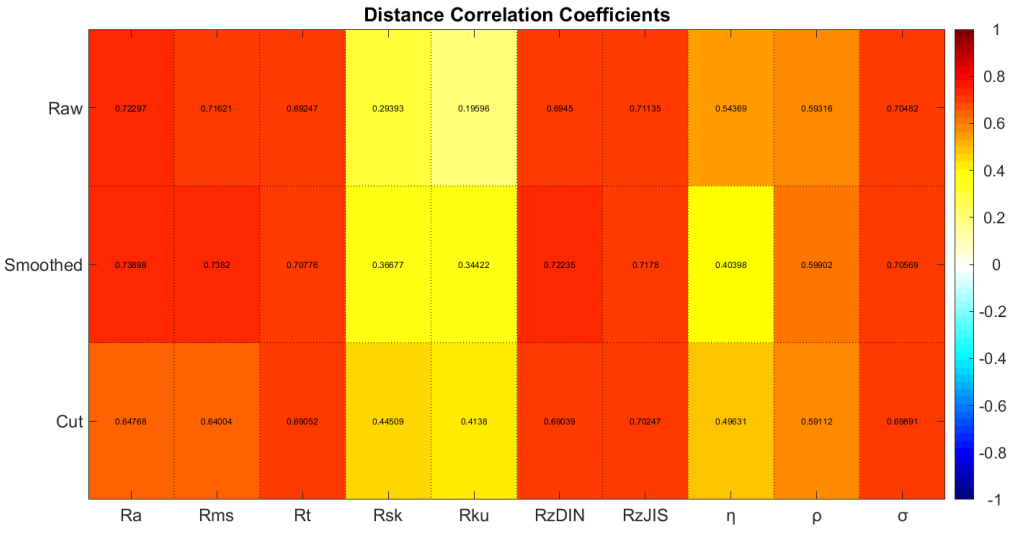

Figure A.3. Distance correlation coefficient among surface roughness values and high-cycle fatigue life.

APPENDIX B

DIFFERENT WEIGHTING ARRAYS FOR NEAREST NEIGHBOR FORMULATION

As discussed in Chapter 4, a_i accounts for the pore-pore interactions via a weighted nearest-neighbor formulation, with the weights assigned by the term w, which is an array of length $n-1$. In this work, a linear weighting is used such that the array consists of evenly spaced values ranging from 1 to 0, which, for a given pore, will weight the closer pores more than pores farther away. The array of nearest-neighbor distances, d, is arranged closest to farthest and measures the distance between the centroids of the i^{th} and j^{th} pores. Similar to the scaling parameters α and ρ, γ is a scaling parameter for the exponential decay and expresses the relative influence of a given pore on the VDF value in terms of its interactions with all other pores in the specimen. The optimal value of γ was determined using a Bayesian optimization approach [149] similar to that used in Erickson et al. [145] to find the optimal values of α and ρ. The optimal value for γ was determined to be 0.225 and is used for the remainder of this work. Intuitively, an exponential or logarithmic weighting of the nearest-neighbor distances may be more appropriate. However, it is noted that the weighted nearest-neighbor term is nested within an exponential term in Eqn. 4.8. Thus, although the nearest-neighbor distances are linearly weighted in a_i, its effect on the VDF value is nonlinear. Additionally, different arrays were tested and compared with the linearly weighted arrays (w). For example, a logarithmic decaying array was incorporated and analyzed using the Erickson computational data set. The logarithmic decay array accurately predicted fracture location in 81 out of 120 simulated tensile specimens; whereas, the linearly weighted array accurately predicted 96 out of 120. It was concluded that the linearly weighted nearest neighbor distances ultimately performed the best.

APPENDIX C

PORE ARRANGEMENT TEST CASE

Although Erickson's VDF formulation does account for pore clustering relative to a given reference point (z_{ref}), it does not account for pore-pore interaction. Figure 4.1c illustrates this limitation by showing two scenarios that would result in equivalent values of VDF despite having obvious differences in the interactions between the two pores P_1 and P_2. For Erickson's VDF formulation, the two cases have the same VDF value because the distance from z_{ref} to P_2 is identical in both cases, and there is no term in Eqn. 4.1 that accounts for the distance between P_1 and P_2. Realistically, the case on the left in Figure 4.1c could be considered more critical than the one on the right due to the interacting stress fields between the two pores, which could impact the fracture behavior. This can best be shown using a simple FE model to show the cases with pores clustered closer together will have a higher stress concentration. It is possible that the pore-pore interaction could also create a stress shielding effect leading to an overall reduction in stress concentrations. Figure C.1a and b show two cases where the interactions of the stress fields of these pores cause an increase in stress concentration.

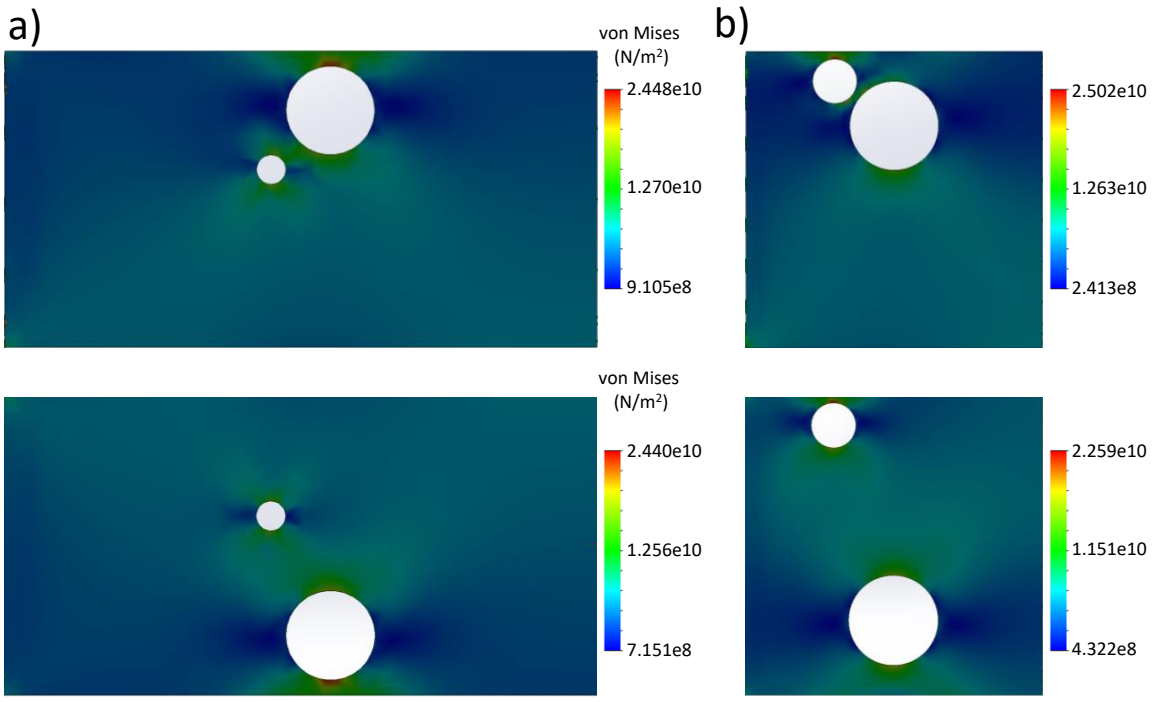

Figure C.1. FE models showing pore-pore interactions effects on stress concentrations for a) the first test case and b) the second test case.

REFERENCES

[1] D. S. Watring, J. T. Benzing, N. Hrabe, and A. D. Spear, "Effects of laser-energy density and build orientation on the structure–property relationships in as-built inconel 718 manufactured by laser powder bed fusion," *Additive manufacturing*, vol. 36, p. 101425, 2020.

[2] Y. Huang, M. C. Leu, J. Mazumder, and A. Donmez, "Additive manufacturing: current state, future potential, gaps and needs, and recommendations," *Journal of Manufacturing Science and Engineering*, vol. 137, no. 1, 2015.

[3] T. Wohlers, "Wohlers report," *Wohlers Associates Inc*, 2018.

[4] M. Baumers, "Economic aspects of additive manufacturing: benefits, costs and energy consumption," Ph.D. dissertation, © Martin Baumers, 2012.

[5] N. Shamsaei, A. Yadollahi, L. Bian, and S. M. Thompson, "An overview of direct laser deposition for additive manufacturing; part ii: Mechanical behavior, process parameter optimization and control," *Additive Manufacturing*, vol. 8, pp. 12–35, 2015.

[6] T. M. Mower and M. J. Long, "Mechanical behavior of additive manufactured, powder-bed laser-fused materials," *Materials Science and Engineering: A*, vol. 651, pp. 198–213, 2016.

[7] T. DebRoy, H. Wei, J. Zuback, T. Mukherjee, J. Elmer, J. Milewski, A. M. Beese, A. d. Wilson-Heid, A. De, and W. Zhang, "Additive manufacturing of metallic components–process, structure and properties," *Progress in Materials Science*, vol. 92, pp. 112–224, 2018.

[8] J. P. Oliveira, A. LaLonde, and J. Ma, "Processing parameters in laser powder bed fusion metal additive manufacturing," *Materials & Design*, vol. 193, p. 108762, 2020.

[9] J. Gockel, L. Sheridan, B. Koerper, and B. Whip, "The influence of additive manufacturing processing parameters on surface roughness and fatigue life," *International Journal of Fatigue*, vol. 124, pp. 380–388, 2019.

[10] D. S. Watring, K. C. Carter, D. Crouse, B. Raeymaekers, and A. D. Spear, "Mechanisms driving high-cycle fatigue life of as-built inconel 718 processed by laser powder bed fusion," *Materials Science and Engineering: A*, vol. 761, p. 137993, 2019.

[11] V. Tvergaard, "Material failure by void growth to coalescence," *Advances in applied Mechanics*, vol. 27, pp. 83–151, 1989.

[12] W. E. Frazier, "Metal additive manufacturing: a review," *Journal of Materials Engineering and Performance*, vol. 23, no. 6, pp. 1917–1928, 2014.

[13] J. J. Lewandowski and M. Seifi, "Metal additive manufacturing: a review of mechanical properties," *Annual review of materials research*, vol. 46, pp. 151–186, 2016.

[14] M. Salarian, H. Asgari, and M. Vlasea, "Pore space characteristics and corresponding effect on tensile properties of inconel 625 fabricated via laser powder bed fusion," *Materials Science and Engineering: A*, vol. 769, p. 138525, 2020.

[15] R. Snell, S. Tammas-Williams, L. Chechik, A. Lyle, E. Hernández-Nava, C. Boig, G. Panoutsos, and I. Todd, "Methods for rapid pore classification in metal additive manufacturing," *JOM*, pp. 1–9, 2019.

[16] M. Svensson, U. Ackelid, and A. Ab, "Titanium alloys manufactured with electron beam melting mechanical and chemical properties," in *Proceedings of the materials and processes for medical devices conference*. ASM International, 2010, pp. 189–194.

[17] J. Elmer, J. Vaja, H. Carlton, and R. Pong, "The effect of ar and n2 shielding gas on laser weld porosity in steel, stainless steels, and nickel," *Weld J*, vol. 94, no. 10, pp. 313s–325s, 2015.

[18] W. E. King, H. D. Barth, V. M. Castillo, G. F. Gallegos, J. W. Gibbs, D. E. Hahn, C. Kamath, and A. M. Rubenchik, "Observation of keyhole-mode laser melting in laser powder-bed fusion additive manufacturing," *Journal of Materials Processing Technology*, vol. 214, no. 12, pp. 2915–2925, 2014.

[19] V.-P. Matilainen, H. Piili, A. Salminen, and O. Nyrhilä, "Preliminary investigation of keyhole phenomena during single layer fabrication in laser additive manufacturing of stainless steel," *Physics Procedia*, vol. 78, pp. 377–387, 2015.

[20] N. Kouraytem, X. Li, R. Cunningham, C. Zhao, N. Parab, T. Sun, A. D. Rollett, A. D. Spear, and W. Tan, "Effect of laser-matter interaction on molten pool flow and keyhole dynamics," *Physical Review Applied*, vol. 11, no. 6, p. 064054, 2019.

[21] R. Cunningham, S. P. Narra, C. Montgomery, J. Beuth, and A. Rollett, "Synchrotron-based x-ray microtomography characterization of the effect of processing variables on porosity formation in laser power-bed additive manufacturing of ti-6al-4v," *Jom*, vol. 69, no. 3, pp. 479–484, 2017.

[22] A. du Plessis, I. Yadroitsava, and I. Yadroitsev, "Effects of defects on mechanical properties in metal additive manufacturing: A review focusing on x-ray tomography insights," *Materials & Design*, vol. 187, p. 108385, 2020.

[23] M. Tang, P. C. Pistorius, and J. L. Beuth, "Prediction of lack-of-fusion porosity for powder bed fusion," *Additive Manufacturing*, vol. 14, pp. 39–48, 2017.

[24] G. Vastola, Q. Pei, and Y.-W. Zhang, "Predictive model for porosity in powder-bed fusion additive manufacturing at high beam energy regime," *Additive Manufacturing*, vol. 22, pp. 817–822, 2018.

[25] C. Kamath, B. El-dasher, G. F. Gallegos, W. E. King, and A. Sisto, "Density of additively-manufactured, 316l ss parts using laser powder-bed fusion at powers up to 400 w," *The International Journal of Advanced Manufacturing Technology*, vol. 74, no. 1-4, pp. 65–78, 2014.

[26] L. Sheridan, O. E. Scott-Emuakpor, T. George, and J. E. Gockel, "Relating porosity to fatigue failure in additively manufactured alloy 718," *Materials Science and Engineering: A*, vol. 727, pp. 170–176, 2018.

[27] E. Lucon, J. Benzing, and N. Hrabe, "Effect of precrack configuration and lack-of-fusion on the elastic-plastic fracture toughness of additively manufactured ti-6al-4v parts," *Materials Performance and Characterization*, vol. 9, no. 5, 2020.

[28] A. Sola and A. Nouri, "Microstructural porosity in additive manufacturing: The formation and detection of pores in metal parts fabricated by powder bed fusion," *Journal of Advanced Manufacturing and Processing*, vol. 1, no. 3, p. e10021, 2019.

[29] D. Dai, D. Gu, H. Zhang, J. Xiong, C. Ma, C. Hong, and R. Poprawe, "Influence of scan strategy and molten pool configuration on microstructures and tensile properties of selective laser melting additive manufactured aluminum based parts," *Optics & Laser Technology*, vol. 99, pp. 91–100, 2018.

[30] A. Hilaire, E. Andrieu, and X. Wu, "High-temperature mechanical properties of alloy 718 produced by laser powder bed fusion with different processing parameters," *Additive Manufacturing*, vol. 26, pp. 147–160, 2019.

[31] S. Gribbin, J. Bicknell, L. Jorgensen, I. Tsukrov, and M. Knezevic, "Low cycle fatigue behavior of direct metal laser sintered inconel alloy 718," *International Journal of Fatigue*, vol. 93, pp. 156–167, 2016.

[32] P. Wang, M. L. S. Nai, X. Tan, W. J. Sin, S. B. Tor, and J. Wei, "Anisotropic mechanical properties in a big-sized ti-6al-4v plate fabricated by electron beam melting," in *TMS 2016 145th Annual Meeting & Exhibition*. Springer, 2016, pp. 5–12.

[33] P. Wang, X. Tan, M. L. S. Nai, S. B. Tor, and J. Wei, "Spatial and geometrical-based characterization of microstructure and microhardness for an electron beam melted ti–6al–4v component," *Materials & Design*, vol. 95, pp. 287–295, 2016.

[34] X. Tan, P. Wang, Y. Kok, W. Toh, Z. Sun, S. Nai, M. Descoins, D. Mangelinck, E. Liu, and S. Tor, "Carbide precipitation characteristics in additive manufacturing of co-cr-mo alloy via selective electron beam melting," *Scripta Materialia*, vol. 143, pp. 117–121, 2018.

[35] S. Al-Bermani, M. Blackmore, W. Zhang, and I. Todd, "The origin of microstructural diversity, texture, and mechanical properties in electron beam melted ti-6al-4v," *Metallurgical and materials transactions a*, vol. 41, no. 13, pp. 3422–3434, 2010.

[36] B. Song, X. Zhao, S. Li, C. Han, Q. Wei, S. Wen, J. Liu, and Y. Shi, "Differences in microstructure and properties between selective laser melting and traditional manufacturing for fabrication of metal parts: A review," *Frontiers of Mechanical Engineering*, vol. 10, no. 2, pp. 111–125, 2015.

[37] M. Simonelli, Y. Y. Tse, and C. Tuck, "On the texture formation of selective laser melted ti-6al-4v," *Metallurgical and Materials Transactions A*, vol. 45, no. 6, pp. 2863–2872, 2014.

[38] A. A. Antonysamy, J. Meyer, and P. Prangnell, "Effect of build geometry on the β-grain structure and texture in additive manufacture of ti6al4v by selective electron beam melting," *Materials characterization*, vol. 84, pp. 153–168, 2013.

[39] L. Bian, S. M. Thompson, and N. Shamsaei, "Mechanical properties and microstructural features of direct laser-deposited ti-6al-4v," *Jom*, vol. 67, no. 3, pp. 629–638, 2015.

[40] L. Thijs, M. L. M. Sistiaga, R. Wauthle, Q. Xie, J.-P. Kruth, and J. Van Humbeeck, "Strong morphological and crystallographic texture and resulting yield strength anisotropy in selective laser melted tantalum," *Acta Materialia*, vol. 61, no. 12, pp. 4657–4668, 2013.

[41] L. González-Fernández, L. Del Campo, R. Pérez-Sáez, and M. Tello, "Normal spectral emittance of inconel 718 aeronautical alloy coated with yttria stabilized zirconia films," *Journal of Alloys and Compounds*, vol. 513, pp. 101–106, 2012.

[42] J. Lambarri, J. Leunda, V. G. Navas, C. Soriano, and C. Sanz, "Microstructural and tensile characterization of inconel 718 laser coatings for aeronautic components," *Optics and Lasers in Engineering*, vol. 51, no. 7, pp. 813–821, 2013.

[43] E. Ezugwu, Z. Wang, and A. Machado, "The machinability of nickel-based alloys: a review," *Journal of Materials Processing Technology*, vol. 86, no. 1-3, pp. 1–16, 1999.

[44] E. Akca and A. Gürsel, "A review on superalloys and in718 nickel-based inconel superalloy," *Periodicals of Engineering and Natural Sciences (PEN)*, vol. 3, no. 1, 2015.

[45] R. Molins, G. Hochstetter, J. Chassaigne, and E. Andrieu, "Oxidation effects on the fatigue crack growth behaviour of alloy 718 at high temperature," *Acta Materialia*, vol. 45, no. 2, pp. 663–674, 1997.

[46] X. Wang, X. Gong, and K. Chou, "Review on powder-bed laser additive manufacturing of inconel 718 parts," *Proceedings of the Institution of Mechanical Engineers, Part B: Journal of Engineering Manufacture*, vol. 231, no. 11, pp. 1890–1903, 2017.

[47] C. Radhakrishna, K. P. Rao, and S. Srinivas, "Laves phase in superalloy 718 weld metals," *Journal of materials science letters*, vol. 14, no. 24, pp. 1810–1812, 1995.

[48] J.-P. Costes, Y. Guillet, G. Poulachon, and M. Dessoly, "Tool-life and wear mechanisms of cbn tools in machining of inconel 718," *International Journal of Machine Tools and Manufacture*, vol. 47, no. 7-8, pp. 1081–1087, 2007.

[49] T. Sugihara and T. Enomoto, "High speed machining of inconel 718 focusing on tool surface topography of cbn tool," *Procedia Manufacturing*, vol. 1, pp. 675–682, 2015.

[50] A. K. Parida and K. Maity, "Comparison the machinability of inconel 718, inconel 625 and monel 400 in hot turning operation," *Engineering Science and Technology, an International Journal*, vol. 21, no. 3, pp. 364–370, 2018.

[51] B. Izquierdo, S. Plaza, J. Sánchez, I. Pombo, and N. Ortega, "Numerical prediction of heat affected layer in the edm of aeronautical alloys," *Applied Surface Science*, vol. 259, pp. 780–790, 2012.

[52] Z. Wang, K. Guan, M. Gao, X. Li, X. Chen, and X. Zeng, "The microstructure and mechanical properties of deposited-in718 by selective laser melting," *Journal of Alloys and Compounds*, vol. 513, pp. 518–523, 2012.

[53] A. Hilaire, E. Andrieu, and X. Wu, "High-temperature mechanical properties of alloy 718 produced by laser powder bed fusion with different processing parameters," *Additive Manufacturing*, vol. 26, pp. 147–160, 2019.

[54] K. Morgan, "Additive manufacturing overview: Propulsion applications, design for and lessons learned," 2017.

[55] L. E. Criales, Y. M. Arısoy, B. Lane, S. Moylan, A. Donmez, and T. Özel, "Laser powder bed fusion of nickel alloy 625: experimental investigations of effects of process parameters on melt pool size and shape with spatter analysis," *International Journal of Machine Tools and Manufacture*, vol. 121, pp. 22–36, 2017.

[56] B. Mueller, "Additive manufacturing technologies–rapid prototyping to direct digital manufacturing," *Assembly Automation*, vol. 32, no. 2, 2012.

[57] M. Schmidt, M. Merklein, D. Bourell, D. Dimitrov, T. Hausotte, K. Wegener, L. Overmeyer, F. Vollertsen, and G. N. Levy, "Laser based additive manufacturing in industry and academia," *CIRP Annals*, vol. 66, no. 2, pp. 561–583, 2017.

[58] L. E. Murr, S. M. Gaytan, D. A. Ramirez, E. Martinez, J. Hernandez, K. N. Amato, P. W. Shindo, F. R. Medina, and R. B. Wicker, "Metal fabrication by additive manufacturing using laser and electron beam melting technologies," *Journal of Materials Science & Technology*, vol. 28, no. 1, pp. 1–14, 2012.

[59] J. Warren and D. Wei, "The cyclic fatigue behavior of direct age 718 at 149, 315, 454 and 538 c," *Materials Science and Engineering: A*, vol. 428, no. 1-2, pp. 106–115, 2006.

[60] A. Thomas, M. El-Wahabi, J. Cabrera, and J. Prado, "High temperature deformation of inconel 718," *Journal of materials processing technology*, vol. 177, no. 1-3, pp. 469–472, 2006.

[61] K. Prasad, R. Sarkar, P. Ghosal, V. Kumar, and M. Sundararaman, "High temperature low cycle fatigue deformation behaviour of forged in 718 superalloy turbine disc," *Materials Science and Engineering: A*, vol. 568, pp. 239–245, 2013.

[62] D.-H. Jeong, M.-J. Choi, M. Goto, H.-C. Lee, and S. Kim, "Effect of service exposure on fatigue crack propagation of inconel 718 turbine disc material at elevated temperatures," *Materials Characterization*, vol. 95, pp. 232–244, 2014.

[63] H. Zhang, S. Zhang, M. Cheng, and Z. Li, "Deformation characteristics of δ phase in the delta-processed inconel 718 alloy," *Materials characterization*, vol. 61, no. 1, pp. 49–53, 2010.

[64] K. Rana, S. Rinaldi, S. Imbrogno, G. Rotella, D. Umbrello, R. M. Saoubi, and S. Ayvar-Soberanis, "2d fe prediction of surface alteration of inconel 718 under machining condition," *Procedia CIRP*, vol. 45, pp. 227–230, 2016.

[65] F1877, "Standard practice for characterization of particles," *ASTM International*, 2016.

[66] E466, "Standard practice for conducting force controlled constant amplitude axial fatigue tests of metallic materials," *ASTM International*, 2015.

[67] J. Ciurana, L. Hernandez, and J. Delgado, "Energy density analysis on single tracks formed by selective laser melting with cocrmo powder material," *The International Journal of Advanced Manufacturing Technology*, vol. 68, no. 5-8, pp. 1103–1110, 2013.

[68] K. Amato, S. Gaytan, L. Murr, E. Martinez, P. Shindo, J. Hernandez, S. Collins, and F. Medina, "Microstructures and mechanical behavior of inconel 718 fabricated by selective laser melting," *Acta Materialia*, vol. 60, no. 5, pp. 2229–2239, 2012.

[69] T. Trosch, J. Strößner, R. Völkl, and U. Glatzel, "Microstructure and mechanical properties of selective laser melted inconel 718 compared to forging and casting," *Materials letters*, vol. 164, pp. 428–431, 2016.

[70] K. Sadananda, , and A. Vasudevan, "Short crack growth and internal stresses," *International Journal of Fatigue*, vol. 19, no. 93, pp. 99–108, 1997.

[71] K. Sadananda and A. Vasudevan, "Crack tip driving forces and crack growth representation under fatigue," *International Journal of Fatigue*, vol. 26, no. 1, pp. 39–47, 2004.

[72] A. Mkaddem and M. El Mansori, "On fatigue crack growth mechanisms of mmc: Reflection on analysis of 'multi surface initiations'," *Materials & Design*, vol. 30, no. 9, pp. 3518–3524, 2009.

[73] H. J. Jin and S. J. Wu, "A new driving force parameter for fatigue growth of multiple cracks," *International Journal of Fatigue*, vol. 96, pp. 10–16, 2017.

[74] A. D. Spear and A. R. Ingraffea, "Effect of chemical milling on low-cycle fatigue behavior of an al–mg–si alloy," *Corrosion Science*, vol. 68, pp. 144–153, 2013.

[75] E. Olakanmi, R. Cochrane, and K. Dalgarno, "Densification mechanism and microstructural evolution in selective laser sintering of al–12si powders," *Journal of Materials Processing Technology*, vol. 211, no. 1, pp. 113–121, 2011.

[76] T. Kimura and T. Nakamoto, "Microstructures and mechanical properties of a356 (alsi7mg0. 3) aluminum alloy fabricated by selective laser melting," *Materials & Design*, vol. 89, pp. 1294–1301, 2016.

[77] C. Kantzos, J. Pauza, R. Cunningham, S. P. Narra, J. Beuth, and A. Rollett, "An investigation of process parameter modifications on additively manufactured inconel 718 parts," *Journal of Materials Engineering and Performance*, vol. 28, no. 2, pp. 620–626, 2019.

[78] Y. Chen, F. Lu, K. Zhang, P. Nie, S. R. E. Hosseini, K. Feng, and Z. Li, "Dendritic microstructure and hot cracking of laser additive manufactured inconel 718 under improved base cooling," *Journal of Alloys and Compounds*, vol. 670, pp. 312–321, 2016.

[79] C. E. Roberts, D. Bourell, T. Watt, and J. Cohen, "A novel processing approach for additive manufacturing of commercial aluminum alloys," *Physics Procedia*, vol. 83, pp. 909–917, 2016.

[80] Y. Chen, K. Zhang, J. Huang, S. R. E. Hosseini, and Z. Li, "Characterization of heat affected zone liquation cracking in laser additive manufacturing of inconel 718," *Materials & Design*, vol. 90, pp. 586–594, 2016.

[81] K. Shiozawa, Y. Morii, S. Nishino, and L. Lu, "Subsurface crack initiation and propagation mechanism in high-strength steel in a very high cycle fatigue regime," *International Journal of Fatigue*, vol. 28, no. 11, pp. 1521–1532, 2006.

[82] G. Chai, "The formation of subsurface non-defect fatigue crack origins," *International Journal of Fatigue*, vol. 28, no. 11, pp. 1533–1539, 2006.

[83] J. Hyzak and I. Bernstein, "The effect of defects on the fatigue crack initiation process in two p/m superalloys: Part ii. surface-subsurface transition," *Metallurgical transactions A*, vol. 13, no. 1, pp. 45–52, 1982.

[84] A. D. Spear, S. F. Li, J. F. Lind, R. M. Suter, and A. R. Ingraffea, "Three-dimensional characterization of microstructurally small fatigue-crack evolution using quantitative fractography combined with post-mortem x-ray tomography and high-energy x-ray diffraction microscopy," *Acta Materialia*, vol. 76, pp. 413–424, 2014.

[85] J.-P. Kruth, L. Froyen, J. Van Vaerenbergh, P. Mercelis, M. Rombouts, and B. Lauwers, "Selective laser melting of iron-based powder," *Journal of materials processing technology*, vol. 149, no. 1-3, pp. 616–622, 2004.

[86] M. Rehnberg and S. Ponte, "3d printing and global value chains: How a new technology may restructure global production," *Global Production Networks Centre: Singapore, Copenhagen Business School, (2016)*, 2016.

[87] W. E. King, A. T. Anderson, R. Ferencz, N. Hodge, C. Kamath, S. A. Khairallah, and A. M. Rubenchik, "Laser powder bed fusion additive manufacturing of metals; physics, computational, and materials challenges," *Applied Physics Reviews*, vol. 2, no. 4, p. 041304, 2015.

[88] S. A. Khairallah, A. T. Anderson, A. Rubenchik, and W. E. King, "Laser powder-bed fusion additive manufacturing: Physics of complex melt flow and formation mechanisms of pores, spatter, and denudation zones," *Acta Materialia*, vol. 108, pp. 36–45, 2016.

[89] P. Karimi, E. Sadeghi, D. Deng, H. Gruber, J. Andersson, and P. Nylén, "Influence of build layout and orientation on microstructural characteristics of electron beam melted alloy 718," *The International Journal of Advanced Manufacturing Technology*, vol. 99, pp. 2903–2913, 2018.

[90] F. Imani, A. Gaikwad, M. Montazeri, P. Rao, H. Yang, and E. Reutzel, "Process mapping and in-process monitoring of porosity in laser powder bed fusion using layerwise optical imaging," *Journal of Manufacturing Science and Engineering*, vol. 140, no. 10, 2018.

[91] K. Moussaoui, W. Rubio, M. Mousseigne, T. Sultan, and F. Rezai, "Effects of selective laser melting additive manufacturing parameters of inconel 718 on porosity, microstructure and mechanical properties," *Materials Science and Engineering: A*, vol. 735, pp. 182–190, 2018.

[92] J. Benzing, N. Hrabe, T. Quinn, R. White, R. Rentz, and M. Ahlfors, "Hot isostatic pressing (hip) to achieve isotropic microstructure and retain as-built strength in an additive manufacturing titanium alloy (ti-6al-4v)," *Materials Letters*, vol. 257, p. 126690, 2019.

[93] Q. Jia and D. Gu, "Selective laser melting additive manufacturing of inconel 718 superalloy parts: Densification, microstructure and properties," *Journal of Alloys and Compounds*, vol. 585, pp. 713–721, 2014.

[94] L. L. Parimi, G. Ravi, D. Clark, and M. M. Attallah, "Microstructural and texture development in direct laser fabricated in718," *Materials Characterization*, vol. 89, pp. 102–111, 2014.

[95] X. Wang, J. A. Muñiz-Lerma, O. Sánchez-Mata, M. A. Shandiz, and M. Brochu, "Microstructure and mechanical properties of stainless steel 316l vertical struts manufactured by laser powder bed fusion process," *Materials Science and Engineering: A*, vol. 736, pp. 27–40, 2018.

[96] Y. Zhong, "Sub-grain structure in additive manufactured stainless steel 316l," Ph.D. dissertation, Department of Materials and Environmental Chemistry, Stockholm University, 2017.

[97] T. G. Gallmeyer, S. Moorthy, B. B. Kappes, M. J. Mills, B. Amin-Ahmadi, and A. P. Stebner, "Knowledge of process-structure-property relationships to engineer better heat treatments for laser powder bed fusion additive manufactured inconel 718," *Additive Manufacturing*, vol. 31, p. 100977, 2020.

[98] Y. Mu, C. Wang, W. Zhou, and L. Zhou, "Effect of nb on δ phase precipitation and the tensile properties in cast alloy in625," *Metals*, vol. 8, no. 2, p. 86, 2018.

[99] A. Mostafa, I. Picazo Rubio, V. Brailovski, M. Jahazi, and M. Medraj, "Structure, texture and phases in 3d printed in718 alloy subjected to homogenization and hip treatments," *Metals*, vol. 7, no. 6, p. 196, 2017.

[100] G. M. Reddy, C. S. Murthy, K. S. Rao, and K. P. Rao, "Improvement of mechanical properties of inconel 718 electron beam welds—influence of welding techniques and postweld heat treatment," *The International Journal of Advanced Manufacturing Technology*, vol. 43, no. 7-8, pp. 671–680, 2009.

[101] J. J. Schirra, R. H. Caless, and R. W. Hatala, "The effect of laves phase on the mechanical properties of wrought and cast + hip inconel 718," *The Minerals, Metals & Materials Society*, pp. 375–388, 2015.

[102] M.Pröbstle, S. Neumeier, J.Hopfenmüller, L.P.Freund, T.Niendorf, D.Schwarze, and M.Gökena, "Superior creep strength of a nickel-based superalloy produced by selective laser melting," *Materials Science and Engineering A*, vol. 674, pp. 299–3078, Sep 2016.

[103] "E3076-18, standard practice for determination of the slope in the linear region of a test," ASTM International, Standard, 2018.

[104] "E8-16a, standard test methods for tension testing of metallic materials," ASTM International, Standard, 2016.

[105] J. Schindelin, I. Arganda-Carreras, E. Frise, V. Kaynig, M. Longair, T. Pietzsch, S. Preibisch, C. Rueden, S. Saalfeld, B. Schmid *et al.*, "Fiji: an open-source platform for biological-image analysis," *Nature methods*, vol. 9, no. 7, p. 676, 2012.

[106] H. Gong, K. Rafi, H. Gu, T. Starr, and B. Stucker, "Analysis of defect generation in ti–6al–4v parts made using powder bed fusion additive manufacturing processes," *Additive Manufacturing*, vol. 1, pp. 87–98, 2014.

[107] A. Matsunawa, J.-D. Kim, N. Seto, M. Mizutani, and S. Katayama, "Dynamics of keyhole and molten pool in laser welding," *Journal of Laser Applications*, vol. 10, no. 6, pp. 247–254, 1998.

[108] C. Pei, D. Shi, H. Yuan, and H. Li, "Assessment of mechanical properties and fatigue performance of a selective laser melted nickel-base superalloy inconel 718," *Materials Science and Engineering A*, vol. 759, pp. 278–287, June 2019.

[109] H. Gong, H. Gu, K. Zeng, J. Dilip, D. Pal, B. Stucker, D. Christiansen, J. Beuth, and J. J. Lewandowski, "Melt pool characterization for selective laser melting of ti-6al-4v pre-alloyed powder," in *Solid freeform fabrication symposium*, 2014, pp. 256–267.

[110] L. Thijs, F. Verhaeghe, T. Craeghs, J. Van Humbeeck, and J.-P. Kruth, "A study of the microstructural evolution during selective laser melting of ti–6al–4v," *Acta materialia*, vol. 58, no. 9, pp. 3303–3312, 2010.

[111] W. M. Tucho and V. Hansen, "Characterization of slm-fabricated inconel 718 after solid solution and precipitation hardening heat treatments," *Journal of materials science*, vol. 54, no. 1, pp. 823–839, 2019.

[112] P. Littlewood, T. Britton, and A. Wilkinson, "Geometrically necessary dislocation density distributions in ti–6al–4v deformed in tension," *Acta Materialia*, vol. 59, no. 16, pp. 6489–6500, 2011.

[113] W. M. Tucho, P. Cuvillier, A. Sjolyst-Kverneland, and V. Hansen, "Microstructure and hardness studies of inconel 718 manufactured by selective laser melting before and after solution heat treatment," *Materials Science and Engineering: A*, vol. 689, pp. 220–232, 2017.

[114] U. S. Bertoli, G. Guss, S. Wu, M. J. Matthews, and J. M. Schoenung, "In-situ characterization of laser-powder interaction and cooling rates through high-speed imaging of powder bed fusion additive manufacturing," *Materials & Design*, vol. 135, pp. 385–396, 2017.

[115] H. Qi, M. Azer, and A. Ritter, "Studies of standard heat treatment effects on microstructure and mechanical properties of laser net shape manufactured inconel 718," *Metallurgical and Materials Transactions A*, vol. 40, pp. 2410–2422, Oct 2009.

[116] Y. Idell, L. E. Levine, A. J. Allen, F. Zhang, C. E. Campbell, G. B. Olson, J. Gong, D. R. Snyder, and H. Z. Deutchman, "Unexpected δ-phase formation in additive-manufactured ni-based superalloy," *JOM*, vol. 68, no. 3, pp. 950–959, Mar 2016.

[117] F. Zupanič, T. Bončina, A. Križman, and F. Tichelaar, "Structure of continuously cast ni-based superalloy inconel 713c," *Journal of Alloys and Compounds*, vol. 329, no. 1-2, pp. 290–297, 2001.

[118] A. Bhambri, T. Kattamis, and J. Morral, "Cast microstructure of inconel 713c and its dependence on solidification variables," *Metallurgical Transactions B*, vol. 6, no. 4, pp. 523–537, 1975.

[119] S. Manikandan, D. Sivakumar, K. P. Rao, and M. Kamaraj, "Laves phase in alloy 718 fusion zone—microscopic and calorimetric studies," *Materials Characterization*, vol. 100, pp. 192–206, 2015.

[120] H.Y.Wan, Z.J.Zhou, C.P.Li, G.F.Chen, and G.P.Zhang, "Effect of scanning strategy on mechanical properties of selective laser melted inconel 718," *Materials Science and Engineering A*, vol. 753, pp. 42–48, Apr 2019.

[121] S. Sui, J. Chen, E. Fan, H. Yang, X. Lin, and W. Huang, "The influence of laves phases on the high-cycle fatigue behavior of laser additive manufactured inconel 718," *Materials Science and Engineering: A*, vol. 695, pp. 6–13, 2017.

[122] H. Xiao, S. Li, X. Han, J. Mazumder, and L. Song, "Laves phase control of inconel 718 alloy using quasi-continuous-wave laser additive manufacturing," *Materials & Design*, vol. 122, pp. 330–339, 2017.

[123] N. T. Aboulkhair, N. M. Everitt, I. Ashcroft, and C. Tuck, "Reducing porosity in alsi10mg parts processed by selective laser melting," *Additive Manufacturing*, vol. 1, pp. 77–86, 2014.

[124] D. Deng, R. L. Peng, H. Brodin, and J. Moverare, "Microstructure and mechanical properties of inconel 718 produced by selective laser melting: Sample orientation dependence and effects of post heat treatments," *Materials Science and Engineering: A*, vol. 713, pp. 294–306, 2018.

[125] L. Parry, I. Ashcroft, and R. D. Wildman, "Understanding the effect of laser scan strategy on residual stress in selective laser melting through thermo-mechanical simulation," *Additive Manufacturing*, vol. 12, pp. 1–15, 2016.

[126] J. Grum and R. Šturm, "A new experimental technique for measuring strain and residual stresses during a laser remelting process," *Journal of Materials Processing Technology*, vol. 147, no. 3, pp. 351–358, 2004.

[127] K. Wei, M. Lv, X. Zeng, Z. Xiao, G. Huang, M. Liu, and J. Deng, "Effect of laser remelting on deposition quality, residual stress, microstructure, and mechanical property of selective laser melting processed ti-5al-2.5 sn alloy," *Materials Characterization*, vol. 150, pp. 67–77, 2019.

[128] W. Callister and D. G. Rethwisch, *Fundamentals of Materials Science and Engineering*. Wiley London, UK:, 2000.

[129] X. Wang and K. Chou, "Electron backscatter diffraction analysis of inconel 718 parts fabricated by selective laser melting additive manufacturing," *Jom*, vol. 69, no. 2, pp. 402–408, 2017.

[130] M. Kirka, K. Unocic, N. Raghavan, F. Medina, R. Dehoff, and S. Babu, "Microstructure development in electron beam-melted inconel 718 and associated tensile properties," *Jom*, vol. 68, no. 3, pp. 1012–1020, 2016.

[131] Y. Tian, D. McAllister, H. Colijn, M. Mills, D. Farson, M. Nordin, and S. Babu, "Rationalization of microstructure heterogeneity in inconel 718 builds made by the direct laser additive manufacturing process," *Metallurgical and Materials Transactions A*, vol. 45, no. 10, pp. 4470–4483, 2014.

[132] N. Kouraytem, R. A. Chanut, D. S. Watring, T. Loveless, J. Varga, A. D. Spear, and O. T. Kingstedt, "Dynamic-loading behavior and anisotropic deformation of pre-and post-heat-treated in718 fabricated by selective laser melting," *Additive Manufacturing*, p. 101083, 2020.

[133] S. Beretta and S. Romano, "A comparison of fatigue strength sensitivity to defects for materials manufactured by am or traditional processes," *International Journal of Fatigue*, vol. 94, pp. 178–191, 2017.

[134] B. Torries, A. Imandoust, S. Beretta, S. Shao, and N. Shamsaei, "Overview on microstructure-and defect-sensitive fatigue modeling of additively manufactured materials," *Jom*, vol. 70, no. 9, pp. 1853–1862, 2018.

[135] J. Zhao, M. Easton, M. Qian, M. Leary, and M. Brandt, "Effect of building direction on porosity and fatigue life of selective laser melted alsi12mg alloy," *Materials Science and Engineering: A*, vol. 729, pp. 76–85, 2018.

[136] A. L. Gurson, "Continuum theory of ductile rupture by void nucleation and growth: Part i—yield criteria and flow rules for porous ductile media," 1977.

[137] T.-S. Cao, M. Mazière, K. Danas, and J. Besson, "A model for ductile damage prediction at low stress triaxialities incorporating void shape change and void rotation," *International Journal of Solids and Structures*, vol. 63, pp. 240–263, 2015.

[138] F. Fritzen, S. Forest, T. Böhlke, D. Kondo, and T. Kanit, "Computational homogenization of elasto-plastic porous metals," *International journal of plasticity*, vol. 29, pp. 102–119, 2012.

[139] Y.-K. Khdir, T. Kanit, F. Zaïri, and M. Naït-Abdelaziz, "A computational homogenization of random porous media: Effect of void shape and void content on the overall yield surface," *European Journal of Mechanics-A/Solids*, vol. 49, pp. 137–145, 2015.

[140] V. Tvergaard, "Influence of voids on shear band instabilities under plane strain conditions," *International Journal of fracture*, vol. 17, no. 4, pp. 389–407, 1981.

[141] O. L. Kafka, K. K. Jones, C. Yu, P. Cheng, and W. K. Liu, "Image-based multiscale modeling with spatially varying microstructures from experiments: Demonstration with additively manufactured metal in fatigue and fracture," *Journal of the Mechanics and Physics of Solids*, p. 104350, 2021.

[142] G. Antou, G. Montavon, F. Hlawka, A. Cornet, and C. Coddet, "Characterizations of the pore-crack network architecture of thermal-sprayed coatings," *Materials Characterization*, vol. 53, no. 5, pp. 361–372, 2004.

[143] A. Du Plessis, I. Yadroitsava, S. G. Le Roux, I. Yadroitsev, J. Fieres, C. Reinhart, and P. Rossouw, "Prediction of mechanical performance of ti6al4v cast alloy based on microct-based load simulation," *Journal of Alloys and Compounds*, vol. 724, pp. 267–274, 2017.

[144] J. D. Madison, O. D. Underwood, L. P. Swiler, B. L. Boyce, B. H. Jared, J. M. Rodelas, and B. C. Salzbrenner, "Corroborating tomographic defect metrics with mechanical

response in an additively manufactured precipitation-hardened stainless steel," in *AIP conference proceedings*, vol. 1949, no. 1. AIP Publishing LLC, 2018, p. 020009.

[145] J. M. Erickson, A. Rahman, and A. D. Spear, "A void descriptor function to uniquely characterize pore networks and predict ductile-metal failure properties," *International Journal of Fracture*, vol. 225, no. 1, pp. 47–67, 2020.

[146] A. Yadollahi, N. Shamsaei, Y. Hammi, and M. F. Horstemeyer, "Quantification of tensile damage evolution in additive manufactured austenitic stainless steels," *Materials Science and Engineering: A*, vol. 657, pp. 399–405, 2016.

[147] O. A. Von Lilienfeld, R. Ramakrishnan, M. Rupp, and A. Knoll, "Fourier series of atomic radial distribution functions: A molecular fingerprint for machine learning models of quantum chemical properties," *International Journal of Quantum Chemistry*, vol. 115, no. 16, pp. 1084–1093, 2015.

[148] B. L. Boyce, B. C. Salzbrenner, J. M. Rodelas, L. P. Swiler, J. D. Madison, B. H. Jared, and Y.-L. Shen, "Extreme-value statistics reveal rare failure-critical defects in additive manufacturing," *Advanced Engineering Materials*, vol. 19, no. 8, p. 1700102, 2017.

[149] B. Shahriari, K. Swersky, Z. Wang, R. P. Adams, and N. De Freitas, "Taking the human out of the loop: A review of bayesian optimization," *Proceedings of the IEEE*, vol. 104, no. 1, pp. 148–175, 2015.

[150] Z. Li, Y. Jing, H. Guo, X. Sun, K. Yu, A. Yu, X. Jiang, and X. Yang, "Study of 3d pores and its relationship with crack initiation factors of aluminum alloy die castings," *Metallurgical and Materials Transactions B*, vol. 50, no. 3, pp. 1204–1212, 2019.

[151] H. Wadell, "Volume, shape, and roundness of quartz particles," *The Journal of Geology*, vol. 43, no. 3, pp. 250–280, 1935.

[152] L.-A. Liew, L.-A. Liew, D. T. Read, R. White, and N. Barbosa III, *US Army ARDEC Joint Fuze Technology Program (JFTP) Task 2 report: quasi-static tensile tests of microfabricated electrodeposited (LIGA) Ni alloys*. US Department of Commerce, National Institute of Standards and Technology, 2018.

[153] J. T. Benzing, L.-A. Liew, N. Hrabe, and F. W. DelRio, "Tracking defects and microstructural heterogeneities in meso-scale tensile specimens excised from additively manufactured parts," *Experimental Mechanics*, vol. 60, no. 2, pp. 165–170, 2020.

[154] "ij-plugins/ijp-toolkit," https://github.com/ij-plugins/ijp-toolkit/wiki/3D-IO, accessed: 2021-03-23.

[155] M. A. Groeber and M. A. Jackson, "DREAM.3D: A Digital Representation Environment for the Analysis of Microstructure in 3D," *Integrating Materials and Manufacturing Innovation*, vol. 3, no. 1, p. 5, 2014.

[156] U. Ayachit, *The paraview guide: a parallel visualization application*. Kitware, Inc., 2015.

[157] B. L. Welch, "The generalization ofstudent's' problem when several different population variances are involved," *Biometrika*, vol. 34, no. 1/2, pp. 28–35, 1947.

[158] B. C. Salzbrenner, J. M. Rodelas, J. D. Madison, B. H. Jared, L. P. Swiler, Y.-L. Shen, and B. L. Boyce, "High-throughput stochastic tensile performance of additively manufactured stainless steel," *Journal of Materials Processing Technology*, vol. 241, pp. 1–12, 2017.

[159] Y. Kok, X. P. Tan, P. Wang, M. Nai, N. H. Loh, E. Liu, and S. B. Tor, "Anisotropy and heterogeneity of microstructure and mechanical properties in metal additive manufacturing: A critical review," *Materials & Design*, vol. 139, pp. 565–586, 2018.

[160] J. I. McCool, "Relating profile instrument measurements to the functional performance of rough surfaces," *Journal of Tribology*, vol. 109, no. 2, pp. 264–270, 1987.

[161] G. Pawar, P. Pawlus, I. Etsion, and B. Raeymaekers, "The effect of determining topography parameters on analyzing elastic contact between isotropic rough surfaces," *Journal of Tribology*, vol. 135, no. 1, p. 011401, 2013.

[162] M. Kalin, A. Pogačnik, I. Etsion, and B. Raeymaekers, "Comparing surface topography parameters of rough surfaces obtained with spectral moments and deterministic methods," *Tribology International*, vol. 93, pp. 137–141, 2016.

[163] K. Pearson, "Determination of the coefficient of correlation," *Science*, vol. 30, no. 757, pp. 23–25, 1909.

[164] J. H. Zar, "Significance testing of the spearman rank correlation coefficient," *Journal of the American Statistical Association*, vol. 67, no. 339, pp. 578–580, 1972.

[165] G. J. Székely, M. L. Rizzo, N. K. Bakirov *et al.*, "Measuring and testing dependence by correlation of distances," *The annals of statistics*, vol. 35, no. 6, pp. 2769–2794, 2007.